LBNL-56751

Femtosecond Nonlinear Spectroscopy at Surfaces: Second-Harmonic Probing of Hole Burning at the Si(111)7×7 Surface and Fourier-Transform Sum-Frequency Vibrational Spectroscopy

John Andrew McGuire
Ph.D. Thesis

Department of Physics
University of California, Berkeley

and

Materials Sciences Division
Ernest Orlando Lawrence Berkeley National Laboratory
University of California
Berkeley CA 94720

December 2004

This work was supported by the Director, Office of Science, Office of Basic Energy Sciences, Materials Sciences Division, of the U.S. Department of Energy under Contract No. DE-AC03-76SF00098.

Femtosecond Nonlinear Spectroscopy at Surfaces:
Second-Harmonic Probing of Hole Burning at the Si(111)7×7 Surface
and Fourier-Transform Sum-Frequency Vibrational Spectroscopy

by

John Andrew McGuire

B.S. (Stanford University) 1992
M.A. (University of California, Berkeley) 2000

A dissertation submitted in partial satisfaction
of the requirements for the degree of

Doctor of Philosophy

in

Physics

in the

GRADUATE DIVISION

of the

UNIVERSITY OF CALIFORNIA, BERKELEY

Committee in charge:

Professor Yuen-Ron Shen, Chair
Professor Peter Y. Yu
Professor Roya Maboudian

Fall 2004

Femtosecond Nonlinear Spectroscopy at Surfaces:
Second-Harmonic Probing of Hole Burning at the Si(111)7×7 Surface
and Fourier-Transform Sum-Frequency Vibrational Spectroscopy

by

John Andrew McGuire

Abstract

Femtosecond Nonlinear Spectroscopy at Surfaces:
Second-Harmonic Probing of Hole Burning at the Si(111)7×7 Surface
and Fourier-Transform Sum-Frequency Vibrational Spectroscopy
by
John Andrew McGuire
Doctor of Philosophy in Physics
University of California, Berkeley
Professor Yuen-Ron Shen, Chair

The high temporal resolution and broad bandwidth of a femtosecond laser system are exploited in a pair of nonlinear optical studies of surfaces.

The dephasing dynamics of resonances associated with the adatom dangling bonds of the Si(111)7×7 surface are explored by transient second-harmonic hole burning, a process that can be described as a fourth-order nonlinear optical process. Spectral holes produced by a 100 fs pump pulse at about 800 nm are probed by the second harmonic signal of a 100 fs pulse tunable around 800 nm. The measured spectral holes yield homogeneous dephasing times of a few tens of femtoseconds. Fits with a Lorentzian spectral hole centered at zero probe detuning show a linear dependence of the hole width on pump fluence, which suggests that charge carrier-carrier scattering dominates the dephasing dynamics at the measured excitation densities. Extrapolation of the deduced homogeneous dephasing times to zero excitation density yields an intrinsic dephasing time of ~ 70 fs. The presence of a secondary spectral hole indicates that scattering of the surface electrons with surface optical phonons at 570 cm^{-1} occurs within the first 200 fs after excitation.

The broad bandwidth of femtosecond IR pulses is used to perform IR-visible sum-frequency vibrational spectroscopy. By implementing a Fourier-transform technique, we demonstrate the ability to obtain sub-laser-bandwidth spectral resolution. FT-SFG yields a greater signal when implemented with a stretched visible pulse than with a femtosecond

visible pulse. However, when compared with multichannel spectroscopy using a femtosecond IR pulse but a narrowband visible pulse, Fourier-transform SFG is found to have an inferior signal-to-noise ratio. A mathematical analysis of the signal-to-noise ratio illustrates the constraints on the Fourier-transform approach.

Professor Yuen-Ron Shen

Dissertation Committee Chair

人非生而知之者，孰能無惑？惑而不從師，其爲惑也，終不解矣。

韓愈『師說』

Contents

List of Figures

List of Tables

Acknowledgements

To the trained eye, this dissertation may appear to be the work of a solitary researcher. Indeed, the shortcomings of this work can be attributed to one, but the successes represent a collective effort both in the laboratory and in my development as a physicist.

Great credit goes to my advisor, Professor Yuen-Ron Shen. His generosity with his time for students and colleagues was matched only by the lucidity of his thought and expression. Professor Shen's insistence on clear physical pictures could always be relied upon to lead to productive experiments, and my failures in research could usually be traced to neglect of his advice. Professor Shen was also generous almost to a fault in funding my investigations and allowing me great latitude despite undoubted misgivings about the directions that I often chose. Were I to insist that I needed just one more length of rope with which to fashion my noose, it is doubtful that he would refuse to provide the necessary funds.

My work was aided immensely by the Alexander von Humboldt Foundation, a reverse Marshall Plan for American science. The post-doctoral fellowships provided by the foundation brought us Dr. Wolfgang Beck, the hit-and-run physicist, and Dr. Markus Raschke. Wolfgang was as congenial a mentor in the laboratory as a young experimentalist could wish for. To Markus I owe my knowledge of ultra-high vacuum techniques and silicon surfaces that allowed us to carry out the spectral hole-burning experiments on the Si(111)7×7 surface. It was Markus' encouragement and expertise that often enabled us to push forward on our "epsilon-squared" experiment and his predilection for wide-ranging debate that frequently provided us the perfect pretext for avoiding that same experiment.

It has been a pleasure to interact with the other members of the Shen Group, all of whom contributed to a culturally rich environment and whatever moments of joy I may have experienced in the lab. My fellow students included Seok-Cheol Hong, guardian of hidden treasures; Thai Truong, the sunniest of basement-dwellers; Mikhail Belkin, aka the devil's advocate, whose every experiment seemingly turned to success; Na Ji, an interesting conversationalist and a model of clear analysis; Luning Zhang, who is to the fairer Chinese students what a flame is to moths; and Weitao Liu, a veritable machine in the lab, even if that occasionally be a mechanical bull in a china shop. Notable among our post-docs and

visitors were Professor Kok Wai Cheah, Groucho Marx's lost Chinese son; Professor I-Chia Chen, who could always be relied upon for a grim assessment of the life of an academic scientist; Dr. Kalle-Heinz Ernst, ever gregarious and a fountain of knowledge of ultra-high vacuum techniques; Dr. Song-Hee Han; Dr. Francois Lagugne; Dr. Masahito Oh-e; and Dr. Victor Ostroverkhov, as humane a physicist as one will find. Special recognition goes to Xing Wei, whose unassuming manner belied the intuition and technical skills of an outstanding physicist, and Professor Lei Xu of Fudan University, with whom I enjoyed many discussions during our attempts to measure photon echoes from the water surface...If only we had succeeded!

Others whose influence I gladly acknowledge include members of the group of Professor Raymond Chiao. With an enthusiasm for physics that is almost juvenile, Professor Chiao is a model of inquisitiveness. Morgan Mitchell and Jack Boyce still impress me as the best experimentalists with whom I have interacted, and it is among my greatest regrets from graduate school that I did not work more closely with them.

I am most indebted to the many people outside the lab who helped me to go, if not as far as I had hoped, farther than I otherwise would have gone. I could not possibly name all of those to whom thanks are due, but a few must be mentioned. To Yu Ouyang I owe my appreciation of classical Chinese, one of my rare pleasures during my most trying period of research. Huang Xiaosheng, with whom I shared so many first-year experiences and a circuitous path to our final year, was regarded by many as the Chinese brother I never had. Neil Switz was among the few with whom I could discuss life both inside and outside the lab in equal depth. I thank the members of Brigid Collective for creating such a civilized home and Luat Vuong for years of patience when I condemned myself to excessive time in a dark basement lab. Although generally a hinderance, Chubs the Cat continually reminded me of the insignificance of research relative to feline needs. To Alexandra and Monica, I owe thanks for having taken on the filial responsibilities that I often neglected. Finally, I cannot give sufficient thanks to my parents, Helena Gutiérrez de Nickerson and John J. McGuire, for having always encouraged me to follow whatever path I chose, even when that path would lead me to the other side of the country or even the other side of the globe.

Chapter 1

Introduction

Surfaces and interfaces play a central role in the physical and life sciences and technology. As the dimensions of a system shrink, the properties of its surfaces become increasingly important and can eventually determine many of the bulk properties. This can be seen clearly in such systems as quantum dots, in which the surface directly influences the bulk properties as the size of the dot decreases [1, 2]. In other systems, it is the surface properties that are of greatest importance. For example, in chemical systems, catalysis frequently occurs at surfaces (e.g., oxidation of CO by platinum) [3]. In living systems, the properties of interfaces in the form of membranes are fundamental.

The variety of problems in surface science barely exceeds the variety of techniques by which they are studied. Some of the most common techniques involve the scattering of charged particles, notably the scattering of electrons in LEED, RHEELS, and Auger spectroscopy. Other massive particles, such as He atoms, are also used to study surface structures. Optical approaches include reflectivity measurements. Techniques combining both photons and massive particles include photoemission spectroscopy and its inverse. The preceding techniques usually probe regions large on the atomic scale, either because they are fundamentally reciprocal-space measurements or because of focusing limitations. In recent years the local probes scanning tunnelling microscopy and atomic force microscopy (AFM) have become ubiquitous. However, with the exception of purely optical techniques and AFM, all of these approaches share a severe limitation: they require the surface under

study to be located in an ultrahigh vacuum ($\leq 10^{-8}$ mbar). Although AFM does not face such a limitation, AFM does not provide spectroscopic information, i.e., it does not provide information about the energy levels or density of states of a system, nor does it provide direct information about dynamics on the fastest timescales.

Optical techniques can probe surfaces in almost any environment. That advantage exists because of the relatively weak interaction of photons with matter, which is also the reason for one of the main disadvantages of applying many optical techniques to surfaces; the weak interaction of photons with matter means that photons travel far without scattering and interact largely with the bulk in a material system. Consequently, application of most optical techniques to surfaces requires one to be able to discriminate against a large bulk signal and generally implies ambiguity about the source (surface or bulk) of the detected signal. However, this difficulty can often be surmounted by means of even-order nonlinear optical techniques.

In this dissertation we report nonlinear optical investigations of surfaces using femtosecond lasers. Femtosecond pulses of coherent radiation can probe the dynamics of surfaces on timescales shorter than the period of vibrational resonances and approaching the fundamental timescales of electronic processes. Despite the broad bandwidth of such sources, we can also perform more familiar second-order frequency-resolved measurements of surface vibrational spectra by adopting Fourier transform techniques. We begin, in Section 1.1, with a brief discussion of surface nonlinear optics. After explaining the limitations on the information that can be obtained by second- versus fourth-order optical process, in Section 1.2 we present a cursory discussion of electron dynamics at surfaces. The laser system and electronics common to both sets of work in this dissertation are presented in Section 1.3. We conclude with a brief outline of the body of the dissertation.

1.1 A Brief Review of Surface Nonlinear Optics

Under excitation by a strong electric field, the polarization of a medium displays deviations from a linear response to the field. These deviations are the basis of nonlinear optics. As the basic theory of nonlinear optics has been studied extensively [4, 5], we shall merely

discuss it in general terms. Strong electric fields give rise to nonlinear source terms (charge and current densities) in the Maxwell equations. These terms generally include both local and nonlocal terms and can be described by a generalized polarization. For electric fields that are not too strong, the generalized polarization of the medium can be expanded in a power series in the total electric field:

$$\vec{P}(\omega) = \sum_{n=1}^{\infty} \vec{P}^{(n)}(\omega), \tag{1.1}$$

where

$$\begin{aligned} \vec{P}^{(n)}(\vec{k},\omega) &= \boldsymbol{\chi}^{(n)}(\vec{k} = \vec{k}_n + \vec{k}_{n-1} + \cdots + \vec{k}_1; \omega = \omega_n + \omega_{n-1} + \cdots + \omega_1)\vec{E}(\vec{k}_n, \omega_n) \\ &\quad \times \vec{E}(\vec{k}_{n-1}, \omega_{n-1}) \cdots \vec{E}(\vec{k}_1, \omega_1), \end{aligned} \tag{1.2}$$

and $\boldsymbol{\chi}^{(n)}(\vec{k} = \vec{k}_n + \vec{k}_{n-1} + \cdots + \vec{k}_1; \omega = \omega_n + \omega_{n-1} + \cdots + \omega_1)$ is the n^{th}-order susceptibility. Alternatively, by a similar power-series expansion in the time domain,

$$\begin{aligned} \vec{P}^{(n)}(\vec{r},t) &= \int_0^{\infty} d\tau_n \int_0^{\infty} d\tau_{n-1} \cdots \int_0^{\infty} d\tau_1 \int d\vec{r}_n \int d\vec{r}_{n-1} \cdots \int d\vec{r}_1 \boldsymbol{R}^{(n)}(\vec{r}, \vec{r}_n, \vec{r}_{n-1}, \ldots, \vec{r}_1; \\ &\quad t, \tau_n, \tau_{n-1}, \ldots, \tau_1)\vec{E}(\vec{r}_n, \tau_n)\vec{E}(\vec{r}_{n-1}, \tau_{n-1}) \cdots \vec{E}(\vec{r}_1, \tau_1), \end{aligned} \tag{1.3}$$

where $\boldsymbol{R}^{(n)}(\vec{r}, \vec{r}_n, \vec{r}_{n-1}, \ldots, \vec{r}_1; t, \tau_n, \tau_{n-1}, \ldots, \tau_1)$ is the n^{th}-order response function. In the dipole approximation, the response is completely local ($\vec{r}_m = \vec{r}$ for all m). In a quantum mechanical approach, the nonlinear susceptibilities or, equivalently, the nonlinear response functions can be calculated in terms of a perturbation expansion of the density matrix.

For our purposes in this dissertation, there are three particularly important features of the nonlinear response functions or susceptibilities. The first important feature concerns their basic symmetry properties. In particular, all response functions and susceptibilities of even order are exactly zero in the dipole approximation for systems that are centrosymmetric. For such systems, the inversion symmetry breaking that necessarily exists at an interface makes even-order nonlinear optical techniques (e.g., second-harmonic generation and sum-frequency generation) surface-specific for centrosymmetric systems in which the dipole approximation holds [6, 7]. The second important feature relates to information about the timescales of the dynamics of a system. In the limit in which the perturbations

of a system by a bath can be divided into processes on very fast timescales and static timescales, the broadening of spectral features is described respectively in terms of homogeneous and inhomogeneous broadening. The two contributions to the broadening cannot be separated by linear spectroscopy; one must go to at least third-order processes (e.g., photon echo and hole burning) to separate the homogeneous from the inhomogeneous contribution to a line's width. The final feature of primary concern to us is obvious from the forms of Equations (1.2) and (1.3): in general, the information (about resonances or the temporal evolution of the system) of an n^{th}-order response function exceeds that of lower-order response functions. From the first and last points, we see that to obtain as much dynamic or spectral information about a surface as one would obtain by nonlinear optical measurements of an equivalent bulk system, one must generally go to higher-order processes at the surface than one would use in the bulk. For example, whereas infrared absorption spectroscopy (a linear technique) yields the vibrational spectrum of a system, sum-frequency generation (SFG, a second-order technique) yields a surface-specific vibrational spectrum.

The first measurements of surface-specific second harmonic generation (SHG) in the group of Y.R. Shen ushered in a new era in surface science [8]. Since then, SHG and SFG have been applied to the study of a multitude of interfaces and problems including studies of liquid-liquid and liquid-solid interfaces [9], the surface melting of ice [10], chemical reactions at surfaces [11], and surface diffusion of molecules [12].

Despite the power of second-order nonlinear optical techniques, there are significant constraints on the information that can be obtained by such techniques. As indicated above, from the perspective of measurements of the coherent dynamics of a system, second-order techniques are largely equivalent to linear measurements insofar as they cannot separate homogeneous and inhomogeneous broadening. To isolate the homogeneous contribution to the broadening of a surface spectral line one must generally use a process of at least fourth order. Guyot-Sionnest measured the homogeneous broadening of the vibrational stretching mode of the monohydride Si-H bond of a hydrogen-terminated Si(111)1×1 surface by such a photon-echo technique [13]. However, in most cases fourth- and higher-order processes are expected to be feeble, and beyond Guyot-Sionnest's photon-echo measurements, there have

been only a handful of studies of surfaces using fourth-order nonlinear optical processes [14, 15, 16, 17].

In general, the weakness of nonlinear optical signals from surfaces (due to the relatively small number of particles probed) places an even greater premium on high intensities than is the case for nonlinear optical signals from many bulk systems. The need for high intensities is one factor leading to the use of pulsed lasers in surface nonlinear optics. However, even with pulses as short as tens of picoseconds, one is often limited in the intensity that can be applied to a sample by sample heating, which can modify the spectral response or damage a sample. This problem suggests moving to the femtosecond regime, where a given peak intensity can be obtained using less energy per unit area. With pulses shorter than the timescales for thermalization of a sample, damage due to absorption of transiently populated excited states also may be reduced. However, increasing the peak intensity by using shorter pulses does not necessarily result in larger signals.

Given a set of laser pulses characterized by a certain energy, U_i, and spot size, A, the scaling of various nonlinear optical signal strengths with pulse length, τ, can readily be determined. In particular, suppose we have a one-photon resonance characterized by a resonance frequency ω_{ba}, a dipole transition matrix element μ_{ba}, a homogeneous linewidth T_2 and an inhomogeneous Gaussian distribution of frequencies characterized by a linewidth $1/T_2^*$ FWHM such that the total linewidth is $1/T_2'$. We suppose that we have a coherent pulse of radiation of frequency $\omega_1 = \omega_{ba}$ and another coherent pulse of radiation of frequency ω_2 such that ω_2 and $\omega_{SF} = \omega_2 + \omega_1$ are far from any one-photon resonances in the system. This is the case that most commonly holds for IR-visible vibrationally resonant SFG. The coherent excitation of a two-level system by a short ($\tau < T_2$) pulse of resonant radiation can be characterized by the tipping angle on the Bloch sphere: $\theta_i = \frac{\mu_{ba}}{\hbar} \int dt\, \mathcal{E}_i(t) \ll \pi$, where $\mathcal{E}_i(t)$ is the electric field envelope. Based on the mixing of a second field with the resulting polarization at ω_{ba}, for pulses shorter than the inverse linewidth and such that $\theta \ll \pi$, the SFG signal scales as $S_{SF} \propto \frac{U_1 U_2 \tau}{A}$. Alternatively, for pulses longer than the inverse linewidth, the SFG signal scales as $S_{SF} \propto \frac{U_1 U_2 T_2'^2}{A\tau}$. In the case of a surface photon-echo measurement in which a pair of pulses (α and β) at frequency ω_1 produce a rephasing

(echo) of the polarization at ω_{ba} (This requires using pulse lengths $\tau < T_2$), for tipping angles $\theta_i = \frac{\mu_{ba}}{\hbar} \int dt\, \mathcal{E}_i(t) \ll \pi$, where $\mathcal{E}_i(t)$ is the electric field envelope, the signal strength scales as $S_{echo} \propto U_{1,a} U_{1,b}^2 U_2 \tau^2 \min(\tau, T_2^*)/A^3$ [13, 18]. In the photon echo measurements of Guyot-Sionnest, the homogeneous and inhomogeneous vibrational dephasing times were both found to be nearly 100 ps, making picosecond pulses much more suitable for their study than femtosecond pulses [13]. In general, for frequency-domain studies of vibrational spectra at surfaces, the optimal pulse length is often of the order of 1 ps. However, for electronic transitions in condensed media, dephasing times are typically much shorter than 1 ps, and measuring electronic dynamics generally requires femtosecond pulses.

1.2 Electron Dynamics at Surfaces

Measurements of electron dynamics yield important information on the timescales for both elastic and inelastic scattering. On a fundamental level, electron dynamics are related to such physical phenomena as charge and heat transport. Electron dynamics are intimately connected to charge screening [19, 20, 21] and can also play important roles in phase transitions [22]. From a technological perspective, electron dynamics are central to device performance.

The role of electron dynamics at interfaces is as important as their role in the bulk. Besides relating to the transport of charge across interfaces [23], electron dynamics at interfaces play an increasingly prominent role in the bulk behavior of a system as the system size decreases to a scale comparable to the electronic mean free path. Electron dynamics also play an important role in photochemistry at surfaces [24, 25, 26, 27]. Although in the preceding examples it is often the incoherent electron dynamics that are most significant, coherent dynamics are also manifested in various surface phenomena. For example, coherent transfer of electronic excitations between a Cu(111) substrate and adsorbed Cs atoms has been observed [28]. More generally, measurements of coherent dynamics provide insight on the nature of the fastest timescale perturbations of a system.

The rapid (subpicosecond) timescales typical of coherent electron dynamics make techniques employing femtosecond lasers well suited to their study. Two-photon photoemis-

sion with femtosecond lasers has been used to study the dephasing of image-potential states [29, 30, 31]. Interferometric two-photon photoemission with 10 fs pulses has been employed to study dynamic dephasing at Cu surfaces [28, 32]. Compared to all-optical techniques, two-photon photoemission has the advantage of being able to provide a complete characterization of the photoemitted electrons in terms of both energy and momentum. However, photoemission is generally restricted to conductors and semiconductors under low excitation densities and ultrahigh vacuum conditions.

Even-order nonlinear optical techniques are applicable to any interface accessible to optical radiation. Particularly in cases in which surface states are only slightly dispersive or localized, nonlinear optical techniques are well suited to studying ultrafast dynamic dephasing. To date, only one publication has described an attempt at nonlinear optical measurement of dynamic electronic dephasing at a surface [15]. The short timescales of electronic dephasing present a great difficulty in measurements of surface photon echoes. This is easily seen in the simplest model for photon echoes: an inhomogeneously broadened Lorentzian oscillator. For such a model, the photon echo signal decays exponentially with respect to the delay τ_1 between the first (exciting) and second (rephasing) pulses with a time constant of $T_2/4$. For dephasing times of the order of 20 fs, one must use pulses of length < 5 fs to be able to resolve the rapid decay of the photon echo. Such pulses are at the very limits of what has been generated in the optical region [33, 34, 35, 36]. For such rapid processes, 100 fs pulses are almost continuous wave. Herein, we use an alternative approach based on transient spectral hole burning to measure the dynamic electronic dephasing at the Si(111)7×7 surface.

1.3 Experimental Setup

The workhorse for the experiments presented in this dissertation is a femtosecond Ti:sapphire laser system operating at repetition rates of 1 kHz. The demand for such lasers has grown dramatically over the last decade. Although these lasers have bandwidths exceeding the typical widths of features in vibrational nonlinear spectroscopy, these systems offer many attractive features compared to typical Nd:YAG-based systems producing pulses of 10's of

picoseconds. In particular, commercial Ti:sapphire systems are now completely solid state, which contributes to their extremely high stability ($< 1\%$ rms shot-to-shot fluctuations) over hours of operation. Moreover, by a variety of techniques that allow for sub-laser-linewidth resolution, such lasers allow one to perform both ultrafast time-resolved spectroscopy and frequency-resolved spectroscopy with the same spectral resolution as obtained with picosecond lasers [37, 38]. As discussed in Section 1.1, on a per-pulse basis a picosecond laser may provide higher signal levels in many nonlinear optical measurements. However, typical Nd:YAG-based systems operate at repetition rates of the order of 10 Hz with pulse energies of the order of several 10's of mJ, which results in limits on the peak intensities that may be applied to a sample due to sample heating and damage constraints. Furthermore, the estimates of Section 1.1 were based on the lasers being tuned to resonance. In typical nonlinear vibrational spectroscopic measurements, one obtains spectra over hundreds of cm^{-1} with resonant features occupying only part of that range. Therefore, the difference in time required to obtain, for example, a vibrationally resonant SFG spectrum with a femtosecond laser system versus the time required with an equivalent picosecond laser system is not as great as suggested by the estimates at the end of Section 1.1.

Generation of energetic pulses begins with a Ti:sapphire oscillator [39, 40] (Kapteyn-Murnane Laboratories, L.L.C. Model TS Ti:sapphire laser kit) pumped by 4.0 W of 532 nm radiation from a diode-pumped, continuous-wave, intracavity-doubled Nd:YVO_4 laser (Spectra Physics Millennia V). Dispersion by the Ti:sapphire crystal in the oscillator is compensated by a pair of Brewster-angle prisms. Kerr lensing in the crystal results in self-mode-locking, which is favored over cw operation when the laser cavity length is adjusted such that the resonator is unstable when operated cw but is stable when producing short pulses (due to the extra wavefront curvature produced by self-focusing) [40, 41]. The mode-locked output is an 80 MHz train of $\sim$7 nJ pulses with a spectrum centered at a wavelength of 800 nm with a bandwidth of about 35 nm FWHM. In fact, the bandwidth can be increased to $\sim$70 nm FWHM. Operation at 35 nm is a compromise between stable mode-locking, which is aided by shorter pulses, and producing high spectral intensity within the bandwidth of the amplifier.

Output pulses from the oscillator are amplified to the ∼1 mJ level by a chirped pulse amplifier (Positive Light Spitfire). The seed pulses from the oscillator are stretched to several 100 ps by chirping the pulses by diffracting them four times off a grating, between which diffraction steps the beam propagates a distance of ∼1 m. This permits amplification of the pulses to the ∼1 mJ level without giving rise to the large intensities that would damage the crystal were the unchirped seed pulses to be directly amplified. The stretched seed is sent to the regenerative amplifier cavity, where a Ti:sapphire crystal is pumped by 10 W of 527 nm radiation from an arc-lamp-pumped, intra-cavity-frequency-doubled, Q-switched Nd:YLF laser (Positive Light Merlin). One Pockel's cell makes the cavity high-Q for the seed pulses. After the seed has been amplified to the point of saturation, a second Pockel's cell is fired to dump the pulse. A signal from a fast photodiode detecting a higher-order diffracted beam from the stretcher grating allows for synchronization of the switching of the two Pockel's cells so that only about 1 in 82,000 seed pulses is amplified through more than one round trip in the regenerative cavity. The 1 kHz output from the regenerative cavity goes to a compressor inverse to the stretcher. The path length of the compressor is adjusted for the optimal compensation of the chirp imposed by the stretcher and regenerative amplifier cavity to produce pulses that are 100 fs FWHM. The pulse energy stability is $< 1\%$ peak-to-peak and $< 0.5\%$ rms.

Despite the stability of the output energy of the amplifier, fluctuations in SHG from the 800 nm fundamental can exceed 20% peak-to-peak. These fluctuations are presumed to be due to pulse-length fluctuations. Pulse-length fluctuations can arise due to unequal fluctuations in the optical path length, and hence the accumulated phase, of different frequencies within the $\sim$150 cm^{-1} bandwidth of the pulses arising from variations in the index of refraction of the air along the different paths travelled by different frequencies within the pulse stretcher and compressor. Assuming that the spatial profile of the pulse does not fluctuate, the fluctuations in the SHG give a direct measure of the fluctuations in the pulse length. Such pulse-length fluctuations can produce dramatic fluctuations in nonlinear signals and the output of an optical parametric amplifier (OPA) pumped by the amplifier output. The average OPA output energy can also exhibit drift of $\pm 10\%$ over timescales from

seconds to minutes on account of such fluctuations. These fluctuations can be minimized by inserting construction paper baffles in the regenerative amplifier box to reduce air flow and by moving the high voltage power supply for the Pockel's cells (a mild heat source for convective airflows) outside the amplifier box. These measures reduced the fluctuations in the SHG from the 800 nm fundamental to below 6% peak-to-peak and below 5% rms.

Most of the output of the amplifier is usually used to pump an OPA. The design on which we eventually settled is based on a design by R.A. Kaindl and P. Hamm and their collaborators [42, 43]. The design, shown in Figure 1.1, is simple with only two passes through a single β-BaB_2O_4 (BBO) crystal (4 mm long, cut for Type-II phase matching: $\theta = 26^\circ$, $\phi = 30^\circ$). Continuum generation from focusing $\sim$2 μJ of 800 nm radiation into a c-cut sapphire crystal (1 mm long) provides the seed for the signal in the first pass. Only $\sim$25 μJ of 800 nm light is focused just after the BBO crystal as a pump. In the second pass, the signal (separated from the idler and first-pass pump by a dichroic mirror) is reflected slightly out of the plane normal to the axis of rotation of the BBO crystal (to allow the amplified radiation to be picked off without disturbing the seed input path) and amplified by a fresh pump of $\sim$600 μJ that was aligned along the same out-of-plane path as the retroreflected product of the first pass. The pump in the second pass is about three times as energetic as that used by Kaindl and Hamm, and their design is not truly scalable since the need to maintain a single-filament white-light continuum limits the amount of energy in the seed. Despite initial concerns about scalability, we do not find any significant degradation of performance when we scale our OPA to three times their pump energies. The largest conversion efficiency obtained in the second pass reached 38%. At conversion efficiencies exceeding about 30%, we observe rms shot-to-shot fluctuations of 2-3% and drift in the average output of $< 1\%$ over timescales of minutes. However, the pump levels needed to obtain such high conversion efficiency eventually damage the dichroic mirrors nearest the crystal. To reduce the likelihood of damage to the dichroic mirrors, the second pass pump is telescoped less tightly resulting in a conversion efficiency of about 25% in the second pass with fluctuations within a factor of two of those cited for the highest conversion efficiencies. In any photon counting experiments, the shot-to-shot fluctuations in photon counts due to

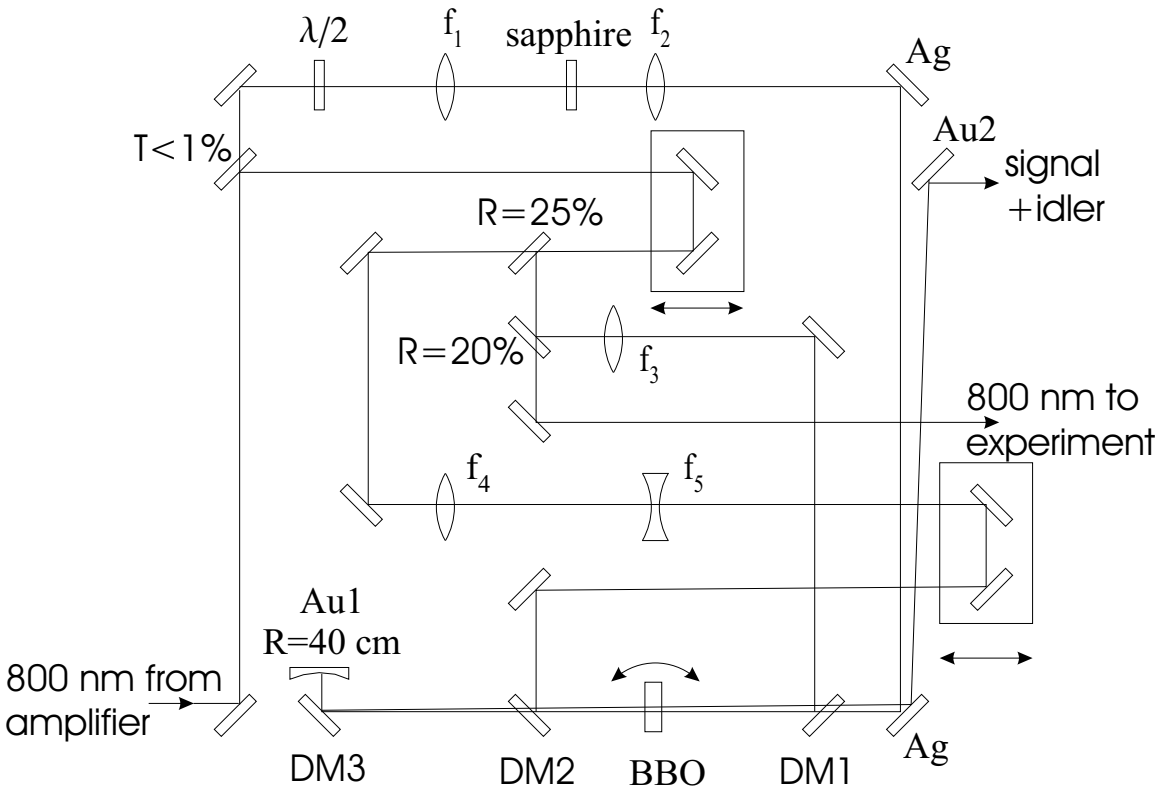

Figure 1.1: White-light-seeded double-pass OPA design used for most of the experiments in this dissertation. All unlabelled elements in the figure are dielectric mirrors for p-polarized broadband 800 nm radiation. DM1 and DM2 are dichroic mirrors to reflect p-polarized 800 nm radiation and transmit s-polarized radiation from 0.95 to 1.6 μm and p-polarized radiation from 1.6 to 5 μm. DM3 is a dichroic mirror to reflect s-polarized radiation from 0.95 to 1.6 μm and transmit p-polarized radiation from 1.6 to 5 μm. The focal lengths of the lenses are (f_1, f_2, f_3, f_4, f_5)=(75 mm, 25 mm, 450 mm, 175 mm, -50 mm). The dashed beam path from Au1 to Au2 is out of the plane of the page and directly above the path of the continuum seed. For KTP the dashed beam is in the plane of the page, as drawn, and the crystal is tuned by rotation about an axis in the plane of the page.

the statistical nature of photon counting exceed the shot-to-shot fluctuations of the amplifier and OPA outputs, so the most important parameter is the long-term stability of the OPA average output energy. As long as the room temperature is stable to better than 0.5° C, the average amplifier and OPA output remain stable. The range of frequencies produced by this OPA is 1.2-2.5 μm, which is limited by absorption in BBO at $\lambda > 2.5$ μm.

To generate wavelengths as long as 3.5 μm, the BBO crystal can be replaced by a $KTiOPO_4$ (KTP) crystal (5 mm long, cut for Type-III phase matching: $\theta = 41°$, $\phi = 0°$). The lower damage threshold of KTP requires pumping with lower intensities ($\sim 15\%$

conversion efficiency). However, this scheme could still produce stable output greater than 20 μJ at 3.3 μm (i.e., in the CH stretch region for vibrational spectroscopy).

The signals in our experiments are detected with photomultiplier tubes (PMTs) in the case of surface-specific signals and photodiodes for bulk signals. The signal from the detector is sent to a boxcar amplifier (Stanford Research Systems Model SR250). Readout of the boxcar signals as well as all experimental control is performed by LabView software via a PC DAQ board (National Instruments LAB-PC-1200), which is usually triggered by a 1 kHz TTL synchronization trigger output from the Spitfire amplifier synchronization and delay generator. In the case of surface-specific signals, all of the data in this dissertation was obtained by using the PMTs in photon counting mode. We count photons only indirectly through counting photoelectron pulses, the generation of which at a PMT photocathode is governed by Poisson statistics. If the average number of photoelectrons produced at a PMT photocathode per pulse is $\bar{n}$, then the probability that n photoelectrons are generated at the cathode is given by

$$P_n(\bar{n}) = \frac{\bar{n}^n}{n!} e^{-n}. \tag{1.4}$$

The probability $\mathcal{P}_{count}$ that there is at least one photoelectron pulse from the PMT is then given by

$$\mathcal{P}_{count} = 1 - P_0(\bar{n}) = 1 - e^{-\bar{n}}. \tag{1.5}$$

The photon counting data (average number, $\bar{n}$, of photons counted by a PMT per pulse) presented in this dissertation are determined from the probability, $\mathcal{P}$, that a pulse from the PMT is detected via the equation $\bar{n} = -\ln\left(1 - \mathcal{P}_{count}\right)$.

Experimental details relevant only to particular experiments are described in later chapters.

1.4 Outline

The rest of this dissertation describes two sets of experiments that make use of the unique properties of femtosecond laser pulses to probe alternately the second- and fourth-order nonlinear responses of surfaces. In Chapter 2 we take advantage of the short length of

100 fs pulses to probe the dynamic dephasing of the Si(111)7×7 surface. By using the second harmonic of a probe beam as a surface-specific probe of the spectral hole produced by a pump beam at 800 nm, we measure the homogeneous linewidth of a surface electronic transition and its dependence on the density of excited carriers. In Chapter 3 we exploit the broad bandwidth of femtosecond pulses by developing a Fourier-transform technique for obtaining arbitrary resolution of vibrational resonances in IR-visible sum-frequency generation spectroscopy. This technique allows the operation of ultrafast lasers as tools for both time- and frequency-resolved spectroscopy.

Chapter 2

Second-Harmonic Hole Burning at the Si(111)7×7 Surface

The Si(111)7×7 surface is of interest for numerous scientific and technological reasons. Hydrogen adsorption on the silicon surface is important in the passivation of etched silicon surfaces [44, 45] and has been studied as a model for chemisorption on semiconductor surfaces [46]. The oxidation of silicon surfaces plays a crucial role in the fabrication of semiconductor devices and has been a subject of extensive study [47]. In particular, the initial oxidation of the Si(111)7×7 surface has been studied in great detail, though many questions remain open [48, 49]. The chemistry of hydrocarbons on silicon is of interest for its relevance to the growth of silicon carbide [50, 51]. In all of these cases, the behavior of the silicon surface is determined by the interplay of surface spatial structure, phonons and electronic structure.

The importance of studying electron dynamics at surfaces has already been discussed in Chapter 1. Understanding coherent electronic dynamics at the Si(111)7×7 surface should yield a greater understanding of charge-carrier interactions at the surface and the phenomena that they influence. To measure these dynamics, we implement a surface-specific variation of hole-burning spectroscopy, a common technique used to measure dynamic dephasing in bulk systems, in which we measure the second harmonic generated by the interaction of the probe fundamental with the surface as a function of the detuning of the probe rel-

ative to the pump. By varying the pump fluence, we can measure the effect of changing charge-carrier densities on electronic dephasing. This can yield clues about the dominant dephasing processes.

The organization of this chapter is as follows. We begin with a review of the results of studies of the Si(111)7×7 spatial and electronic structure with particular attention to those aspects that are related to our optical studies. The review concludes with a discussion of the SHG spectrum of the Si(111)7×7 surface and a discussion of previous studies of electron dynamics at Si surfaces. This review is followed by a discussion of the basic theory of transient spectral hole burning probed by second-harmonic generation in order to understand what information can be gained by such an approach to measuring dynamic dephasing. We then discuss the details of the experimental setup. Finally, we present the experimental results, explain their analysis, and discuss their implications.

2.1 The Si(111)7×7 Surface: Spatial and Electronic Structure

The 7×7 reconstruction of the Si(111) surface was first observed by low-energy electron diffraction (LEED) in 1959 [52]. However, interpretation of LEED is usually dependent on calculations that are model-dependent, and the large size of the unit cell of the Si(111)7×7 surface poses serious challenges to calculations. Although various models were proposed [53, 54, 55], conclusive evidence in favor of any one was lacking [56]. The surface was also studied in reciprocal space by ion backscattering [57] and in real space by scanning tunnelling microscopy [58], but it was the analysis of transmission electron diffraction (TED) measurements by Takayanagi *et al.* that finally yielded the dimer-adatom-stacking fault (DAS) model shown in Figure 2.1 [56]. Further studies such as the X-ray diffraction study by Robinson *et al.* [60], the LEED study by Tong *et al.* [61], and the STM study by Hamers *et al.* [62] confirmed and refined this model, which is now widely accepted.

The 7×7 reconstruction represents a dramatic balancing act between the decrease of the electronic energy resulting from reduction of the number of dangling bonds and the

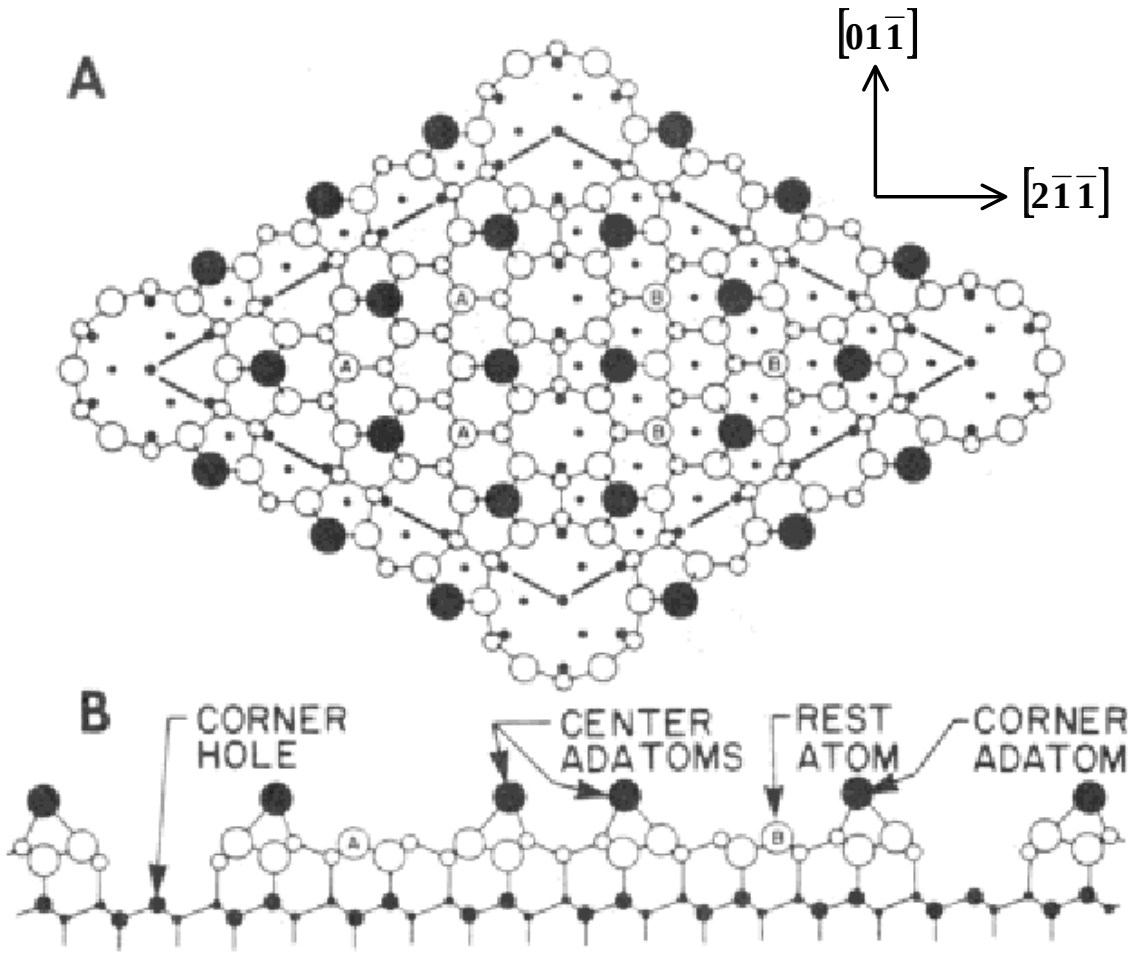

Figure 2.1: Real space structure of the Si(111)7×7 surface (From [59]). Figure B is a view in the $[01\bar{1}]$ direction of the mirror symmetry plane.

increase in the lattice strain produced by the reconstruction. By forming back bonds with 3 atoms in the rest-atom plane, the 12 adatoms reduce the number of dangling bonds by 24. The stacking fault arising from a shift from staggered to eclipsed stacking in one triangular half of the unit cell allows for the formation of dimers in the rest-atom bilayer along the boundaries between triangular subunits; this further reduces the number of dangling bonds by 6. As will be discussed below, the electronic states of the rest-atom dangling bonds are lower in energy than those of the adatoms. Electron transfer from the adatoms to the rest atoms results in lone pairs in the rest-atom dangling bonds. Electron transfer from the adatom dangling bonds to the corner-hole dangling bonds may further reduce the number of electrons not in doubly occupied dangling bonds to five, though whether this is actually

the case is as yet unclear [63]. The corner-hole dangling bonds may instead be half filled, leaving six electrons in the adatom-dangling-bond-derived states.

The electronic structure of the Si(111)7×7 surface has gradually been established over many years of research. The locations and dispersion of the surface electronic bands have been established by photoemission spectroscopy and inverse photoemission spectroscopy. Photoemission spectra clearly show the presence of three occupied bands S_1, S_2, and S_3 centered at energies of about -0.2 eV, -0.9 eV, and -1.9 eV relative to the Fermi level [63, 64, 65, 66, 67]. A weaker feature, S_1', has also been reported at about 0.5 eV below the Fermi level [67]. Inverse photoemission shows unoccupied states U_1 and U_2 at about 0.5 eV and about 1.6 eV above the Fermi level [66, 68, 69, 70]. Measurements of the dispersion of these bands show dispersive widths of about 0.3 eV for S_1 [63], 0.05 eV for S_1' [67], 0.12 eV for S_2 [66, 67, 71], 0.4 eV for S_3, and 0.2 eV for U_1 [72]. The dispersion of the U_2 band has not been measured in detail. These data are tabulated in Table 2.1. Clear indications of band dispersion are also seen in electron energy loss (EELS) spectra [64, 65, 73]. Comparisons with scanning tunnelling spectroscopy demonstrate that S_1 and U_1 are associated primarily with the adatoms, S_2 is associated primarily with the rest atoms, and S_3 and U_2 are associated primarily with the adatom backbonds [62, 74, 75]. Although the S_1' band has not been seen distinctly in STM measurements, S_1' is also conjectured to correspond to adatom dangling bonds [67]. This is summarized in Figure 2.2, where the width and location of each band is based on the most recent data for each band given in Table 2.1. The basic features of the electronic structure are reproduced in theoretical calculations [76, 77].

There remain details of the electronic structure that are unclear, in particular the electronic structure near the Fermi level [63]. Naively, the odd number of electrons in the 7×7 unit cell should produce a metallic surface. Photoemission (inverse photoemission) spectra of the surface electronic structure show nonzero intensity up (down) to the Fermi level [63, 66, 67, 70]. Photoemission and inverse photoemission measurements also indicate that the Fermi level position of the Si(111)7×7 surface is strongly pinned within the bulk band gap for both n- and p-type doping of the bulk at the position $E_F = E_V + 0.65$ eV,

band	location $(E - E_F)$(eV)	dispersion	FWHM	resolution	reference
U_2	1.6	-	0.4	0.3	[68, 69, 70]
U_1	0.5	0.23	0.5	0.35	[72]
	0.5	-	-	0.3	[70]
S_1	-0.15	0.3	0.2	0.027	[63]
	-0.15	0.06	0.2	0.05	[67]
	-0.20	0.1	0.2	0.15	[66]
S_1'	-0.50	0.05	0.2	0.05	[67]
S_2	-0.90	0.12 ± 0.03	0.4	0.05	[67]
	~ -0.95	0.15	0.3	0.15	[66]
	~ -0.8	0.1	0.3	0.2	[71]
S_3	~ -1.9	0.4	0.5	0.15	[66]
	-1.75	0.3	0.6	0.2	[71]

Table 2.1: Summary of the most recently published values of the locations, dispersions, and widths of the surface electronic bands of the Si(111)7×7 surface. The dispersion is the entire range of dispersion of the photoemission or inverse photoemission peak location (i.e., the dispersion of the peak about the specified location is ± half of the noted dispersion value). The column FWHM gives the approximate full-width-at-half-maximum of the photoemission (inverse photoemission) peaks obtained for a particular choice of electron momentum in the surface plane as judged from the data curves presented in the references. The resolution is the combined electron and photon resolution of the equipment used in the studies. All quantities are given in eV.

where E_F is the Fermi level and E_V is the bulk valence band maximum [63, 78]. Electron energy loss spectra also display characteristics of infinitesimal transitions across a Fermi level, namely loss features at very low energies [64, 65, 79]. All of these observations suggest that the surface is indeed metallic. Otherwise, one would expect a gap in the surface electronic structure near the Fermi level. In the case of a nonzero gap, photoemission would yield electrons only up to an energy of the surface valence band maximum $E_{V,s}$, and inverse photoemission would yield photons with maximum energies equal to the difference of the input electron energy E_i and the surface conduction band minimum $E_{C,s}$. With $E_{C,s} \neq E_{V,s}$,

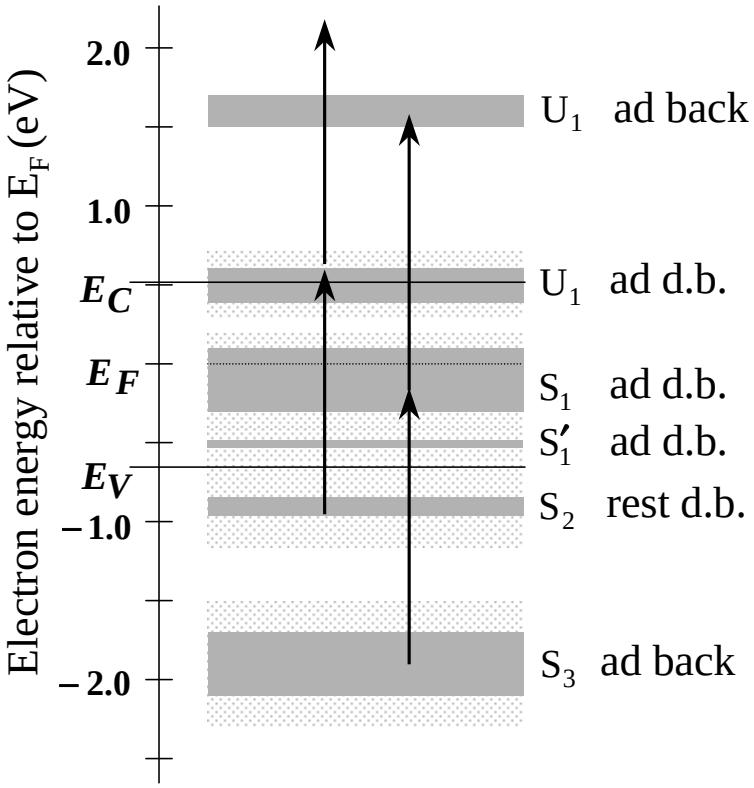

Figure 2.2: Electronic bands of the Si(111)7×7 surface and their source (adatom dangling bonds, adatom back bonds, and rest-atom dangling bonds). The darker region of each band indicates the dispersive range of the peaks measured in angle-resolved photoemission and inverse photoemission, and the dotted region indicates roughly the combined dispersion and measured photoemission linewidth after accounting for the resolution of the measurements listed in Table 2.1. The solid lines labelled E_V and E_C indicate respectively the locations of the bulk valence band maximum and bulk conduction band minimum. The solid arrows represent the presumed optical transitions probed in this work with the left pair representing SHG via a one-photon resonance between rest-atom dangling bonds and adatom dangling bonds and the right pair representing SHG via a two-photon resonance between adatom back-bond states.

one could not have both processes (photoemission and inverse photoemission) indicating transitions from (photoemission) or to (inverse photoemission) the Fermi level. Likewise, if there were a gap at the surface, although the Fermi level might still be pinned for a given type of doping (n- or p-type), the location of the pinning would be different according to whether the sample was n- or p-type [80]. Finally, if there were a surface gap, then the lowest surface EELS feature would also correspond to the surface gap. Therefore, if there is a gap between the occupied and unoccupied states at the surface, the gap is expected to

be very small.

However, there are indications that the surface might not be conducting or at least is a poor conductor. Direct measurements of the surface conductivity by different techniques have yielded widely varying results [81, 82, 83]. NMR measurements of ^{8}Li atoms at low coverage on the Si(111)7×7 surface hint at correlation times associated with fluctuating electron spins that are at least an order of magnitude greater than those typical of metals [84]. EELS measurements at low temperatures suggest that there may be a very narrow (∼2 meV wide), partially occupied state at the Fermi level [64, 65]. This has been interpreted as evidence of a Mott insulator. In fact, as demonstrated by such highly correlated systems as Mott insulators, a non-zero density of states at the Fermi level is not necessarily evidence of metallic character [63, 64, 65, 84]. Theoretical calculations [77] also suggest that the correlation times of the electron gas at the surface may exceed those typical of classical metals [84].

For optical spectroscopy, it is not only the locations of the energy bands and their dispersion that matter but the selection rules for transitions between bands. In EELS, scattering in the specular direction is dominated by long-range dipole scattering and hence yields the same information as obtained by reflection-absorption infrared spectroscopy (RAIRS) but with greater surface sensitivity. (In contrast, off-specular scattering involves short range interactions and is not restricted to dipole-allowed transitions.) Low temperature EELS spectra of specularly scattered electrons show well defined loss features associated with the clean Si(111)7×7 surface at 95, ∼210, ∼340, ∼900, and ∼1500 meV [64, 65, 73, 85, 86]. A detailed study of the loss feature at ∼1.5 eV in which the input electron energy and output detection angle were varied yielded a dispersive energy loss spectrum from about 1.0 to 1.7 eV (about 1.5 eV near zero in-plane wave-vector transfer, $\Delta k_{||} = 0$, i.e., for negligible in-surface-plane momentum transfer as occurs in a purely optical transition) [73]. Based on the locations of the surface bands discussed above and shown in Figure 2.2, the EELS features at ∼ 210 and ∼340 meV were attributed to transitions from the S_1 state to unoccupied surface states within about 50 meV above the Fermi level. Likewise the loss feature at about 900 meV corresponds to transitions between the S_2 band and states within 50 meV

of the Fermi level [64, 65]. The dispersive loss feature from 1.0 to 1.7 eV is interpreted as being due to a transition between the S_2 and U_1 states [73]. These results from EELS studies indicate that one should observe dipole-allowed optical transitions in the range from about 0.9 to 1.7 eV. Indeed, a peak at 1.8 eV is seen in differential reflectivity measurements of the Si(111)7×7 surface [87, 88, 89]. Theoretical calculations qualitatively reproduce the main features of EELS and differential reflectivity studies and assign a calculated EELS and differential reflectance feature at 1.5 eV to transitions from the S_2 to the U_1 band [90].

In the case of nonlinear optical measurements, the symmetry of the surface is particularly important in determining which sets of input and output polarizations will yield nonzero signals and which independent susceptibility tensor elements contribute to the signal for a given set of polarizations. The Si(111)7×7 surface has the same symmetry as the unreconstructed Si(111) surface, namely C_{3v}. If we define our coordinate system such that the z-axis is perpendicular to the surface and the x-axis is normal to the mirror plane (i.e., the x-axis is parallel to the $[01\bar{1}]$ axis in Figure 2.1), then the nonzero second-order susceptibility tensor elements are [4, 7]

$$\begin{aligned} \chi_{zzz} &\equiv \chi_{\perp\perp\perp}, \\ \chi_{xzx} = \chi_{yzy} &\equiv \chi_{\parallel\perp\parallel}, \\ \chi_{xxz} = \chi_{yyz} &\equiv \chi_{\parallel\parallel\perp}, \\ \chi_{yyy} = -\chi_{yxx} = -\chi_{xxy} = -\chi_{xyx} &\equiv \chi_{\parallel\parallel\parallel}, \end{aligned} \tag{2.1}$$

where, from left to right, the indices refer respectively to the output frequency, the higher input frequency, and the lower output frequency, and $\parallel$ and $\perp$ correspond respectively to directions in the surface plane and perpendicular to the surface. In the case of second-harmonic generation, which is the case of interest to us in the following, $\chi_{\parallel\perp\parallel} = \chi_{\parallel\parallel\perp}$. It is worth noting that for an isotropic surface the second-order nonlinear susceptibility tensor elements that are allowed by symmetry to be non-zero include $\chi_{\perp\perp\perp}$, $\chi_{\parallel\perp\parallel}$, and $\chi_{\parallel\parallel\perp}$, whereas for an isotropic surface, $\chi_{\parallel\parallel\parallel} = 0$. Hence, the element $\chi_{\parallel\parallel\parallel}$ is often referred to as the anisotropic element.

Several groups have published second-harmonic spectra of the Si(111)7×7 surface [91, 92, 93, 94, 95]. The spectra are all consistent in their basic features. One such spectrum taken at

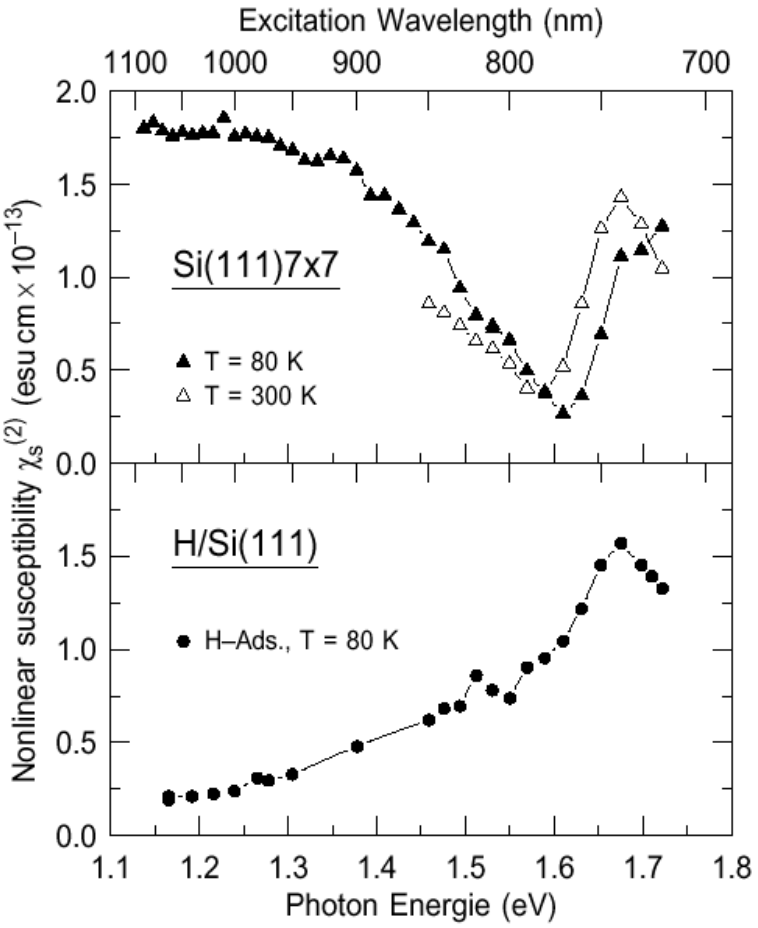

Figure 2.3: SHG spectrum of the magnitude of the anisotropic nonlinear susceptibility element $\chi^{(2)}_{\parallel\parallel\parallel}$ of the Si(111)7×7 surface in a range of fundamental photon energies of about 1.2 to about 1.7 eV at a temperature of 80 K (From reference [91]).

the same temperature as the experiments to be described below is shown in Figure 2.3. The SH spectrum of Si(111)7×7 is dominated by a broad feature extending from a fundamental photon energy below 1.0 eV to about 1.6 eV and a narrower feature extending from a fundamental photon energy of about 1.6 eV to about 1.8 eV. The broad feature from 1.0 to 1.6 eV disappears upon adsorption of atomic hydrogen, but the feature at 1.7 eV (corresponding to a second-harmonic photon energy of 3.4 eV) shows little sensitivity to the adsorption of hydrogen. A similar feature is seen in SHG spectra of the hydrogen-terminated Si(111)1×1 structure [96]. Theoretical calculations of the SHG spectrum expected from the H-terminated Si(111)1×1 surface (a surface with a unit cell of a single atom and so more

amenable to calculation than the Si(111)7×7 surface) indicate that this feature arises from the surface-modified bulk states. A two-photon resonance at a second-harmonic energy of about 3.4 eV is also seen in SHG spectra of the Si(100) surface [91, 95, 97]. Moreover, the bulk E_1 transition between the uppermost valence and lowest conduction bands is at 3.4 eV [98]. All of these observations indicate that the feature seen at a fundamental photon energy of 1.7-eV in the SHG spectra of the Si(111)7×7 surface has little to do with the adatom dangling bonds but is due to a two-photon transition of the strained bulk structure near the surface or between the S_3 and U_2 bands arising from the bonding and antibonding states of the adatom backbonds. In contrast, the extreme sensitivity of the lower energy resonance between 1.0 and 1.6 eV indicates that this feature is due to transitions involving the adatom dangling bonds. From Table 2.1, the sum of the dispersion widths and the photoemission linewidths minus the resolution for S_2 and U_1 indicate that one would expect transitions between these bands to occur for energies from about 1.0 to about 1.8 eV. As with electron energy loss spectra in the range from 1.0 to 1.7 eV, the correspondence of the energy range of the feature in the SHG spectrum to the range of energy differences between the S_2 and U_1 bands shown in Figure 2.2 indicates that the lower-energy feature in the SHG spectrum is likely due to transitions between the S_2 and U_1 bands.

2.2 Ultrafast Electron Dynamics at the Si Surface

Although the surface electronic structure and the corresponding second-harmonic generation spectra of the Si(111)7×7 surface have been characterized in some detail, as noted in Chapter 1 the intrinsic dephasing processes are much more difficult to determine at a surface. To date, there have been a limited number of studies of ultrafast electron dynamics at Si surfaces, and most of these studies have focused on incoherent (population) electron dynamics. Transient-grating techniques have been used to probe the near-surface region of silicon [99]. However, these measurements do not actually address what happens at the surface, particularly in the surface states, but rather probe the bulk within a distance from the surface equal to about a reduced optical wavelength. Early two-photon photoemission experiments on Si(100) probed electron dynamics on the picosecond to tens of picoseconds

timescales [100, 101]. Only recently have experiments been performed with subpicosecond resolution at the Si(100) surface [102, 103].

Measurements of subpicosecond carrier dynamics at the Si(111)7×7 surface by U. Höfer and his collaborators include the only prior study of coherent electronic dynamics at a silicon surface [15, 104, 105]. Using 800 nm radiation, Voelkmann, *et al.* measured a fourth-order transient-grating signal at the Si(111)7×7 surface [15, 105]. However, since the estimated homogeneous dephasing time of only 20 fs yields a photon-echo decay time of 5 fs, even with their 14 fs pulses, an echo signal could not be clearly distinguished, and it was difficult to determine the dephasing time. In such a case, the choice of a population grating complicates matters, since the observed signal arises from both phase and population gratings. Moreover, the energies available even from their cavity-dumped Ti:sapphire oscillator operated at the reduced repetition rate of 10 MHz were so limited that the range of carrier excitation densities studied was limited to a single point.

2.3 Theory of Second-Harmonic Hole Burning

By using the 100 fs output of a regeneratively amplified Ti:sapphire laser system and OPA, we have access to pulses that, despite their broad bandwidth, have narrow bandwidth compared to the spectral features of interest, as is required for hole-burning spectroscopy, yet (as will be seen later) are still shorter than the timescales of the population dynamics of the surface transitions around 1.5 eV. These considerations make spectral hole burning an attractive option for obtaining a clearer measurement of ultrafast dynamic dephasing at a surface than can readily be obtained with photon-echo measurements. Moreover, the large pulse energies produced by such a system allow us to explore a range of pump fluences so as to investigate the effect of changing charge-carrier densities on the electronic dephasing.

Before going into mathematical details of the analysis of hole burning, we discuss some general issues in hole burning and photon-echo spectroscopy, to which hole burning is related, at a surface. In its simplest manifestation, photon-echo spectroscopy from a bulk sample is a two-pulse experimental technique in which a first pulse (at time 0) of length shorter than the homogeneous dephasing time T_2 excites a coherent polarization of the

medium and a second short (again compared T_2) pulse at time T leads to a reversal of the temporal evolution of the system so that the polarization of the medium becomes rephased (or echoes) at time $2T$. This echo is manifested in a pulse of radiation at time $2T$. At sufficiently low excitation intensities that a perturbation expansion of the material response can be terminated at third order in the fields, a photon echo is described in terms of one interaction between the medium with the first pulse field and a pair of interactions between the medium and the second pulse field. Spectral hole burning in a bulk sample is also a two pulse technique. However, in the case of hole burning, one uses a pair of pulses of bandwidth narrower than $1/T_2$ (In elementary descriptions, continuous wave fields are typically assumed). In this case, one measures not an echo at a delayed time but rather the change produced by the first (pump) pulse in the material response (absorption) to the second (probe) pulse as a function of the spectral detuning of the probe relative to the pump. This process can be described as the modification of the first-order response of the medium to the probe by the pump. In a perturbation expansion of the material response that is limited to third order, one can regard this process as arising from two interactions between the medium and the pump field and a single interaction between the medium and the probe field. The generation of a photon echo is a fully coherent process, while the hole-burning signal is largely incoherent. However, as will be seen below, both photon echo and spectral hole burning can be treated by the same, unified formalism. The basic difference between the two techniques is in the timescales of the pulses used and the parameters that are tuned. In photon-echo spectroscopy one must use pulses short compared to T_2 and vary their delay, while in hole-burning spectroscopy one must use pulses long compared to T_2 and vary their detuning.

In many cases, photon echoes and spectral hole burning at a surface can be treated exactly like their bulk counterparts. As noted in Chapter 1, in terms of perturbation expansions of the material response, one must go one order higher at a surface compared to the bulk to get the same dynamic or spectral information. Suppose that we are dealing with a two-level system with resonant frequency ω_{ba} in both the bulk and at the surface. One way to look at photon-echo spectroscopy at a surface is that (at least) a pair of input pulses

of carrier frequency $\omega_1 \approx \omega_{ba}$ produce a rephasing in the surface and bulk polarization at ω_{ba} at time $2T$. At time $2T$ there will be an echo of coherent radiation at frequency ω_{ba} from both the bulk and the surface. By the simple two-pulse photon-echo approach, the echo at frequency ω_{ba} from the surface will be overwhelmed by the echo from the bulk. However, a third pulse at carrier frequency ω_2 and time $2T$ that spatially overlaps the other pulses will interact with the (polarized) material to yield a fourth-order response at frequency $\omega_2+\omega_{ba}$. The pulse at ω_2 will upconvert the surface polarization at ω_{ba} to $\omega_2+\omega_{ba}$. Since this response is even-order (at least fourth-order) in the input fields, the echo signal observed at $\omega_2+\omega_{ba}$ will be due to the surface alone (in the dipole approximation). Likewise, for a surface hole-burning signal, instead of measuring the change in absorption of a probe pulse at frequency ω_2 due to a pump pulse at ω_1, which would be due overwhelmingly to the bulk response, one can look at the change in second-harmonic generation of the probe ($\omega_{\mathrm{SHG}} = 2\omega_2$). Again, this can be viewed as a selective upconversion of the surface polarization at ω_2 to $2\omega_2$.

More generally, one can observe photon echoes from the bulk (surface) using more than two (three) pulses and spectral holes using more than two pulses. In the lowest orders of perturbation theory that can account for these phenomena (third order for bulk and fourth order for surfaces) one can use three (four) separate input fields to observe these processes from the bulk (surface).

2.3.1 Continuous-Wave Treatment

We gain a basic understanding of transient second-harmonic hole burning by following the traditional, continuous-wave analysis of bulk hole burning in terms of a system consisting of an inhomogeneous distribution of oscillators with homogeneous Lorentzian lineshapes [4]. In this picture, we regard the second harmonic of the probe as being generated by a second-order process involving a second-order nonlinear susceptibility modified by the pump. In the absence of a pump pulse, the probe second harmonic in reflection from a surface is given by

$$I(2\omega) = \frac{32\pi^3\omega^2\sec^2\theta_{2\omega}}{c^3\varepsilon_1(\omega)\varepsilon_1^{1/2}(2\omega)}\left|\chi^{(2)}_{\mathrm{eff}}(2\omega;\omega)\right|^2 I^2(\omega), \tag{2.2}$$

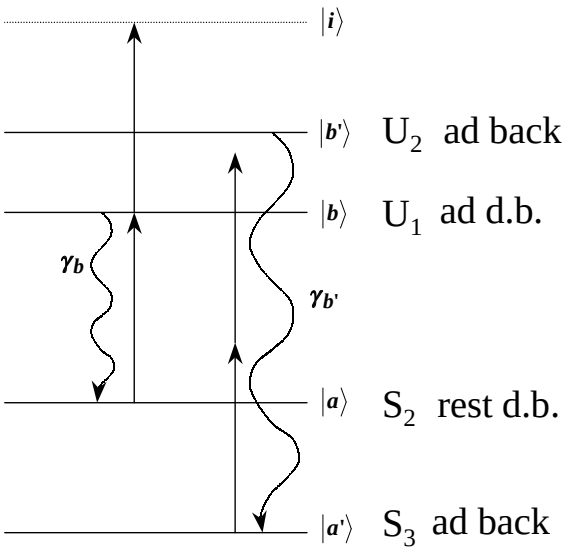

Figure 2.4: Energy level scheme used to model the second-harmonic hole-burning response of the Si(111)7×7 surface at fundamental pump and probe photon energies of about 1.5 eV. Solid arrows represent optically allowed transitions. Wavy arrows represent relaxation pathways. The model is explained in the text.

where ε_1 indicates the dielectric function of the medium from which the fundamental beam is incident and $\theta_{2\omega}$ is the angle of the second-harmonic beam in reflection [6]. The effective second-order susceptibility of the surface is related to the second-order susceptibility $\chi^{(2)}(2\omega;\omega)$ by

$$\chi^{(2)}_{\text{eff}}(2\omega;\omega) = \left[\overleftrightarrow{L}\,(2\omega)\cdot\hat{e}_{2\omega}\right]\cdot\overleftrightarrow{\chi}^{(2)}\,(2\omega;\omega) : \left[\overleftrightarrow{L}\,(\omega)\cdot\hat{e}_{\omega}\right]\left[\overleftrightarrow{L}\,(\omega)\cdot\hat{e}_{\omega}\right], \tag{2.3}$$

where $\overleftrightarrow{L}$ and $\hat{e}$ denote respectively the tensorial Fresnel factor and the unit polarization vector for the corresponding field.

In general, the second-order susceptibility is a sum of various contributions, both resonant and nonresonant, and it helps to have a particular model in mind. Based on the surface states depicted in Figure 2.2 and the SHG spectrum shown in Figure 2.3, we adopt the model shown in Figure 2.4. The levels $|a\rangle$ and $|a'\rangle$ represent the occupied states of the system out of which optical transitions can be made using radiation at about 1.5 eV, namely the rest-atom dangling-bond band S_2 and the adatom back-bond band S_3. Levels $|b\rangle$ and $|b'\rangle$ represent the unoccupied states into which these electronic transitions occur, namely the unoccupied adatom dangling-bond band U_1 and the unoccupied adatom back-bond band

U_2. Level $|i\rangle$ represents virtual states involved in the nonresonant steps in the SHG process. The transition from $|a\rangle$ to $|b\rangle$ models the transitions giving rise to the broad one-photon resonance observed below a fundamental photon energy of 1.6 eV in the SHG spectrum of the Si(111)7×7 surface, and the transition from $|a'\rangle$ to $|b'\rangle$ models the surface transitions giving rise to the two-photon-resonance feature observed at fundamental photon energies just above 1.6 eV in the SHG spectrum of the surface [91]. For our present discussion, the important features of this model are that there are two uncoupled sets of energy levels giving rise to SHG: the unprimed levels, which yield SHG through a one-photon resonance, and the primed levels, which yield SHG through a two-photon resonance.

If we assume that the frequency ω is in the vicinity of a single one-photon resonance at frequency ω_{ba} and that there is no inhomogeneous broadening of the resonance at ω_{ba}, then the susceptibility can be written as

$$\chi^{(2)}(2\omega;\omega) = \chi^{(2)}_{res}(2\omega;\omega) + \chi^{(2)}_{NR}(2\omega;\omega), \tag{2.4}$$

where

$$\chi^{(2)}_{res}(2\omega;\omega) = A\frac{\eta\Delta\rho}{\omega - \omega_{ba} + i\Gamma_{ba}} \tag{2.5}$$

is the resonant contribution of interest, A is a constant, $\Delta\rho = \rho_{aa} - \rho_{bb}$, ρ_{aa} and ρ_{bb} are the populations of the lower and upper states of the resonant transition, η is the number density of oscillators at frequency ω_{ba}, and $\chi^{(2)}_{NR}$ includes all other resonant and nonresonant contributions to the second-order susceptibility (i.e., the two-photon resonance between levels b' and a' of Figure 2.4).

We now add a pump beam. We assume that only the resonance at ω_{ba} is affected by the pump, while $\chi^{(2)}_{NR}$ is unaffected. In the case that we use short pulses and do not temporally overlap the pump and probe, the effect of the pump is merely to modify the populations ρ_{aa} and ρ_{bb}, so that in the presence of the pump,

$$\chi^{(2)}(2\omega_{pr};\omega_{pr};\omega_{pu}) = \chi^{(2)}_{res}(2\omega_{pr};\omega_{pr};\omega_{pu}) + \chi^{(2)}_{NR}(2\omega_{pr};\omega_{pr}), \tag{2.6}$$

where

$$\chi^{(2)}_{res}(2\omega_{pr};\omega_{pr};\omega_{pu}) = A\frac{\eta\Delta\rho(\omega_{pu})}{\omega_{pr} - \omega_{ba} + i\Gamma_{ba}}, \tag{2.7}$$

$$\Delta\rho(\omega_{pu}) = \Delta\rho^{(0)} \Big/ \left(1 + \frac{\Gamma_{ba}^2 I/I_s}{(\omega_{pu}-\omega_{ba})^2 + \Gamma_{ba}^2}\right), \tag{2.8}$$

$I_S = c\hbar^2\Gamma_{ba} \Big/ \left[8\pi n(\omega_{pu})|\vec{\mu}_{ba}\cdot\hat{e}_{\omega_{pu}}|^2 T_1\right]$ is the saturation intensity, $n(\omega_{pu})$ is the index of refraction at the pump frequency, μ_{ba} is the transition dipole matrix element, $\hat{e}_{\omega_{pu}}$ is the unit vector in the direction of the pump electric field, and T_1 is the population relaxation time [4]. (Note that there is a logical inconsistency in stipulating that two continuous wave beams do not overlap temporally. The artifice of not overlapping the beams is merely used to neglect coherent effects that arise from their overlap. However, for $I/I_S \lesssim 1$ these coherent effects are small [4].) In the case of a pump intensity well below the saturation intensity, i.e., $I/I_s \ll 1$, the population difference becomes

$$\Delta\rho(\omega_{pu}) = \Delta\rho^{(0)}\left(1 - \frac{\Gamma_{ba}^2 I/I_s}{(\omega_{pu}-\omega_{ba})^2 + \Gamma_{ba}^2}\right). \tag{2.9}$$

We further assume that any effect of the pump on the Fresnel factors is negligible, in which case we can write

$$\begin{aligned}\chi^{(2)}_{\text{eff}}(2\omega_{pr};\omega_{pr};\omega_{pu}) &= \left[\overleftrightarrow{L}\,(2\omega_{pr})\cdot\hat{e}_{2\omega_{pr}}\right]\cdot\overleftrightarrow{\chi}^{(2)}\,(2\omega_{pr};\omega_{pr};\omega_{pu}) \\ &\quad : \left[\overleftrightarrow{L}\,(\omega_{pr})\cdot\hat{e}_{\omega_{pr}}\right]\left[\overleftrightarrow{L}\,(\omega_{pr})\cdot\hat{e}_{\omega_{pr}}\right].\end{aligned} \tag{2.10}$$

We now consider an inhomogeneous distribution $g(\omega_{ba})$ of resonant frequencies ω_{ba}. The resonant contribution of interest in the second-order susceptibility becomes the integral over the inhomogeneous distribution of $\chi^{(2)}_{res}$ in the absence of inhomogeneous broadening

$$\chi^{(2)}_{res}(2\omega_{pr};\omega_{pr};\omega_{pu}) = A\,\eta\,\Delta\rho^{(0)}\int_{-\infty}^{\infty} d\omega_{ba}\; g(\omega_{ba})\frac{1}{\omega_{pr}-\omega_{ba}+i\Gamma_{ba}}\left(1 - \frac{\Gamma_{ba}^2 I/I_s}{(\omega_{pu}-\omega_{ba})^2+\Gamma_{ba}^2}\right), \tag{2.11}$$

If the distribution $g(\omega_{ba})$ is much broader than Γ_{ba}, then we can pull the term $g(\omega_{ba})$ outside the integral:

$$\chi^{(2)}_{res}(2\omega_{pr};\omega_{pr};\omega_{pu}) = A\,\eta\,\Delta\rho^{(0)} g(\omega_{pu})\int_{-\infty}^{\infty} d\omega_{ba}\frac{1}{\omega_{pr}-\omega_{ba}+i\Gamma_{ba}}\left(1 - \frac{\Gamma_{ba}^2 I/I_s}{(\omega_{pu}-\omega_{ba})^2+\Gamma_{ba}^2}\right). \tag{2.12}$$

The preceding integral is easily evaluated, and we obtain

$$\begin{aligned}\chi^{(2)}_{\text{eff}}(2\omega_{pr};\omega_{pr};\omega_{pu}) &= \chi^{(2)}_{NR,\,\text{eff}}(2\omega_{pr};\omega_{pr}) + \\ &\quad \chi^{(2)}_{res,\,\text{eff},\,0}(2\omega_{pr};\omega_{pr})\left\{1 - i\frac{I}{I_s}\frac{\Gamma_{ba}}{\omega_{pr}-\omega_{pu}+i2\Gamma_{ba}}\right\},\end{aligned} \tag{2.13}$$

where $\chi^{(2)}_{res,\,\mathrm{eff},\,0}(2\omega_{pr};\omega_{pr})$ is the effective second-order nonlinear susceptibility in the absence of the pump beam. Hole burning is found to yield a deviation from the unpumped nonlinear susceptibility characterized by a Lorentzian line with a half width at half maximum of $2\Gamma_{ba}$.

The preceding yields the basic result for spectral hole burning of the second-order nonlinear susceptibility. However, the derivation is based on a steady-state approach. For a better understanding of transient hole burning at a surface, one should implement a formalism using time-domain response functions. A fully coherent treatment in the time domain also illustrates the connections between hole burning and photon-echo spectroscopy and the limitations of hole-burning spectroscopy.

2.3.2 Transient Second-Harmonic Hole Burning

The theoretical framework for understanding transient second-harmonic hole burning at a surface that is presented here is drawn from the established theory for bulk hole burning [5, 106, 107]. The approach is based on an expansion of the density operator in powers of the field-matter interaction. Between interactions, the evolution of the density matrix is determined by the system and system-bath interaction Hamiltonians. Once the value of the density matrix at a given time is known, the material polarization is also known. The polarization can be formally expressed in terms of a response function that relates the polarization to the electric field at the sample. Even if the system Hamiltonian is known, the system-bath interaction presents a major impediment to a detailed calculation of the evolution of the system. However, we can find a solvable model that still illuminates general features of hole burning and other spectroscopic techniques. For the system Hamiltonian, we use the simple model of Figure 2.4 in Section 2.3.1, which captures the essential features seen in second-harmonic and sum-frequency spectroscopy of the Si(111)7×7 surface. By modelling the system-bath interaction through a stochastic variation of the system eigenfrequencies, we can treat phenomena on a wide range of timescales and thereby move beyond the assumption that the timescales of the system-bath interaction are either much shorter or much longer than all relevant experimental timescales, in contrast to the continuous-wave derivation above. We can characterize the polarization of the system in terms of correlation

functions of matrix elements of the dipole operator for both transient hole burning and photon-echo spectroscopy, which illustrates their similarities and differences. By assuming perturbations of the system by the bath to be strictly separated into very fast (compared to the field envelopes) and very slow (compared to all experimental timescales) perturbations and making similar assumptions as were made in the continuous-wave derivation of hole burning, we obtain the same basic result as we found in the preceding treatment.

General Formalism

The temporal evolution of the density operator, $\hat{\rho}$, under the Hamiltonian, $\hat{H}$ is described by the Liouville equation:

$$\frac{d\hat{\rho}}{dt} = -\frac{i}{\hbar}[\hat{H}, \hat{\rho}]. \tag{2.14}$$

We write the Hamiltonian as

$$\hat{H}(t) = \hat{H}_0 + \hat{H}_{int}(t) + \hat{H}_{sb}(t), \tag{2.15}$$

where $\hat{H}_0$, $\hat{H}_{int}(t)$, and $\hat{H}_{sb}(t)$ represent respectively the Hamiltonians of the system, which is assumed to be exactly solvable; the field-matter interaction; and the interaction between the system and the bath. We begin by setting $\hat{H}_{sb}(t) = 0$. We make the dipole approximation for the interaction Hamiltonian:

$$\hat{H}_{int}(t) = -E(\vec{r}, t) \cdot \hat{\mu}, \tag{2.16}$$

where $E(\vec{r}, t)$ is the perturbing electric field and $\hat{\mu}$ is the dipole operator. We expand the density operator in powers of the perturbing field:

$$\hat{\rho}(t) = \hat{\rho}^{(0)}(t) + \hat{\rho}^{(1)}(t) + \hat{\rho}^{(2)}(t) + \hat{\rho}^{(3)}(t) + \cdots. \tag{2.17}$$

From the Liouville equation, we find that $\hat{\rho}^{(n)}(t)$ is related to $\hat{\rho}(t_0)$ by

$$\begin{aligned} \hat{\rho}^{(n)}(t) &= \left(\frac{i}{\hbar}\right)^n \int_{t_0}^{t} d\tau_n \int_{t_0}^{\tau_n} d\tau_{n-1} \cdots \int_{t_0}^{\tau_2} d\tau_1 E(\vec{r}, \tau_n) E(\vec{r}, \tau_{n-1}) \cdots E(\vec{r}, \tau_1) \\ &\quad \times \hat{U}_{(0)}(t, t_0) \left[\hat{\mu}_I(\tau_n), \cdots [\hat{\mu}_I(\tau_2), [\hat{\mu}_I(\tau_1), \hat{\rho}(t_0)]] \cdots\right] \hat{U}^{\dagger}_{(0)}(\tau_t, t_0), \end{aligned} \tag{2.18}$$

where

$$\hat{\mu}_I(\tau) = \hat{U}_0^{\dagger}(\tau, t_0) \hat{\mu} \hat{U}_0(\tau, t_0) \tag{2.19}$$

and $\hat{U}_0(t_2, t_1)$ is the time-evolution operator with respect to the system Hamiltonian:

$$\hat{U}_0(t_2, t_1) = \exp_+ \left[-\frac{i}{\hbar} \int_{t_1}^{t_2} dt\, \hat{H}_0 \right]. \tag{2.20}$$

The + sign in Eq. (2.20) indicates the positive-time-ordered exponential, i.e., for each term in the power series expansion of the operator, each $\hat{H}_0(t_n)$ occurs temporally after all $\hat{H}_0(t_i)$ terms to its right. In terms of this formal expression for the n^{th}-order contribution to the density operator, we can write a formal expression for the n^{th}-order polarization.

The material polarization is given by

$$P(\vec{r}, t) = \eta \, \mathrm{Tr}[\hat{\mu}\hat{\rho}(t)], \tag{2.21}$$

where η is the number density of particles constituting the system. From this point onward, we will generally dispense with explicitly writing vectors and tensors as such. The vector or matrix character of fields, matrices and operators can always be accounted for later. The n^{th}-order contribution to the polarization is then given by

$$\begin{aligned} P^{(n)}(\vec{r}, t) &= \int_0^\infty dt_n \int_0^\infty dt_{n-1} \cdots \int_0^\infty dt_1 R^{(n)}(t_n, t_{n-1}, \ldots, t_1) E(\vec{r}, t - t_n) \\ &\quad \times E(\vec{r}, t - t_n - t_{n-1}) \cdots E(\vec{r}, t - t_n - t_{n-1} - \cdots - t_1), \end{aligned} \tag{2.22}$$

where $R^{(n)}(t_n, t_{n-1}, \ldots, t_1)$ is the n^{th}-order response function, which is given by

$$\begin{aligned} R^{(n)}(t_n, t_{n-1}, \ldots, t_1) &= \eta \left(\frac{i}{\hbar} \right)^n \mathrm{Tr} \{ \hat{\mu}_I(t) \, [\hat{\mu}_I(t - t_n), [\hat{\mu}_I(t - t_n - t_{n-1}), \\ &\quad \cdots \, [\hat{\mu}_I(t - t_n - t_{n-1} - \cdots - t_1), \hat{\rho}(-\infty)] \cdots]] \}. \end{aligned} \tag{2.23}$$

In Eqs. (2.22) and (2.23), we have switched the temporal variables to the time between interactions, i.e., $t_i = \tau_{i+1} - \tau_i$, and we have set $t_0 \to -\infty$, at which time the system is in equilibrium and no pulses have yet arrived. Note that one can see explicitly that the n^{th}-order nonlinear response function is directly related to a sum of $(n+1)$-point correlation functions of the dipole operator $\hat{\mu}_I$.

In the case of second-harmonic hole-burning spectroscopy we are interested in the second-harmonic signal of a probe fundamental beam as a function of the arrival time of the probe

pulse at the sample relative to the arrival time of a pump pulse. Assuming plane-wave fields, we write the pump and probe electric fields as

$$E_{pu}(\vec{r},t) = \mathcal{E}_{pu}(t)e^{i(\vec{k}_{pu}\cdot\vec{r}-\omega_{pu}t)} + c.c. \tag{2.24}$$

and

$$E_{pr}(\vec{r},t) = \mathcal{E}_{pr}(t)e^{i(\vec{k}_{pr}\cdot\vec{r}-\omega_{pr}t)} + c.c., \tag{2.25}$$

with the envelope functions $\mathcal{E}_{pu}(t)$ and $\mathcal{E}_{pr}(t)$ describing pulses. The total field appearing in Eq. (2.22) is

$$E(\vec{r},t) = E_{pu}(\vec{r},t) + E_{pr}(\vec{r},t). \tag{2.26}$$

We can now write for the fourth-order contribution to the polarization with wave vector $2\vec{k}_{pr}$

$$\begin{aligned} P^{(4)}(2\vec{k}_{pr},t) = e^{i(2\vec{k}_{pr}\cdot\vec{r}-2\omega_{pr}t)} \int_0^\infty dt_4 \int_0^\infty dt_3 \int_0^\infty dt_2 \int_0^\infty dt_1 R^{(4)}(t_4,t_3,t_2,t_1) \\ \times\Big[\, e^{i(2\omega_{pr}t_4+\omega_{pr}t_3-\omega_{pu}t_1)}\mathcal{E}_{pr}(t-t_4)\mathcal{E}_{pr}(t-t_4-t_3)\mathcal{E}_{pu}(t-t_4-t_3-t_2) \\ \times\mathcal{E}^*_{pu}(t-t_4-t_3-t_2-t_1) \,+\, \text{other time orderings}\Big]. \end{aligned} \tag{2.27}$$

The meaning of the various temporal variables is illustrated in Figure 2.5, where for later reference we illustrate the most general case in fourth-order spectroscopy of four separate pulses (For second-harmonic hole burning we will treat the case in Figure 2.5 of $\tau_{pump} = \tau_{probe} = 0$, $E_{pump,1} = E_{pump,2} \equiv \mathcal{E}_{pu}$, and $E_{probe,1} = E_{probe,2} \equiv \mathcal{E}_{pr}$). Henceforth, we shall drop the argument $2\vec{k}_{pr}$ of the nonlinear polarization and assume it to be understood. In the following, our task will be the calculation of the fourth-order nonlinear response function $R^{(4)}(t_4,t_3,t_2,t_1)$ or, equivalently, the corresponding five-point correlation function of the dipole operator.

Model Hamiltonian

We now analyze the fourth-order polarization in terms of a simplified model for the electronic levels and transitions at the Si(111)7×7 surface presented in Figure 2.4. The system Hamiltonian is

$$\hat{H}_s = \sum_{\nu=a,a',b,b',i} \hbar\omega_\nu |\nu\rangle\langle\nu|. \tag{2.28}$$

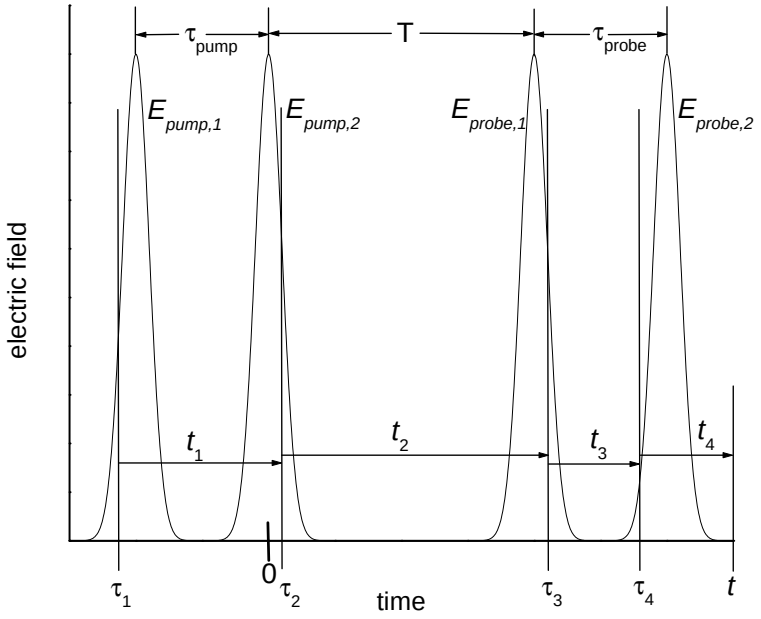

Figure 2.5: Electric-field envelopes and temporal variables for a fourth-order process involving four separate pulses. In the case of spectral hole burning, there are only two separate pulses, and $\tau_{pump} = \tau_{probe} = 0$.

The interaction Hamiltonian is

$$\begin{aligned} \hat{H}_{int}(t) &= \mathcal{E}(t)\Big(\mu_{ba}|b\rangle\langle a| + \mu_{ib}|i\rangle\langle b| + \mu_{ia}|i\rangle\langle a| + \\ &\quad \mu_{b'a'}|b'\rangle\langle a'| + \mu_{ia'}|i\rangle\langle a'| + \mu_{ib'}|i\rangle\langle b'|\Big) + c.c. \end{aligned} \tag{2.29}$$

At this point we take the system-bath interaction Hamiltonian $\hat{H}_{sb}$ to be nonzero and model the effect of this perturbation as a sum of a dissipative term and a term representing a stochastic shift $\hbar\Delta_\nu(t)$ in the energies $\hbar\omega_\nu$ of the eigenstates $|\nu\rangle$:

$$\hat{H}_{sb}(t) = \sum_{\nu=a,a',b,b'} \hbar(\Delta_\nu(t) - i\frac{\gamma_\nu}{2})|\nu\rangle\langle\nu|, \tag{2.30}$$

where $\Delta_\nu(t)$ is a random function, while γ_ν accounts for relaxation of population from level $|\nu\rangle$ [106, 107]. This model, specifically the stochastic variation of the eigenfrequencies by $\Delta_\nu(t)$, is chosen because it provides a straightforward means of accounting for dephasing processes on arbitrary timescales, as will be seen below [108]. The terms γ_ν give rise to the population damping traditionally characterized by the time T_1 and the dephasing to which such population damping gives rise, while the terms $\Delta_\nu(t)$ give rise to pure dephasing. (To

get an idea of how such a Hamiltonian can represent the physical process of dephasing, we consider the example of collisions in an atomic vapor. One way to look at the effect of an elastic collision is as a rapid shift in the positions of the energy levels of the outermost electronic orbitals due to their deformation by the interaction with the other atom(s) during the course of the collision. In the elastic case, no energy relaxation takes place; all that occurs is a change in the phase of oscillations of the atoms at their resonant frequencies relative to the case in which no collision takes place and phase evolves only due to the temporal evolution imposed by the system and interaction Hamiltonians. This change in phase relative to the bath-free evolution results in a loss of coherence because collisions occur randomly. In a collision-broadened vapor, these collision-induced shifts in phase account for the homogeneous dephasing time T_2.) We take $\gamma_a = \gamma_{a'} = 0$, as $|a\rangle$ and $|a'\rangle$ represent the fully occupied states of the system in the ground state. It is assumed that the only processes that produce significant fourth-order response are those that are maximally resonant, i.e., those that create a fourth-order coherence in the density operator through three resonant steps. This is a reasonable assumption given the expected weakness of a fourth-order response. This means that only levels $|a\rangle$ and $|b\rangle$ are involved in the fourth-order response, whereas both processes shown in Figure 2.4 contribute to the second-order response.

The preceding system-bath interaction Hamiltonian accounts for the evolution of the phase of a system due to both population decay and pure dephasing, but it does not fully account for the evolution of the population of the system. Although population decay terms are included, we have not specified to where the population decays. Specifically, the Hamiltonian does not account for the stipulation in our model that population in state $|b\rangle$ decays to state $|a\rangle$. Although we can properly account for such decay by adding off-diagonal terms to the system-bath interaction Hamiltonian, for calculating the evolution of diagonal terms of the density matrix, it is easier to simply work with a master equation for those terms:

$$\frac{d}{dt}\rho_{aa} = -\frac{d}{dt}\rho_{bb} = \gamma_b \rho_{bb}(t), \tag{2.31}$$

for which the solutions are

$$\begin{aligned} \rho_{aa}(t) &= \rho_{aa}(0) + (1 - e^{-\gamma_b t})\rho_{bb}(0) \\ \rho_{bb}(t) &= e^{-\gamma_b t}\rho_{bb}(0). \end{aligned} \tag{2.32}$$

The Fourth-Order Nonlinear Response Function

In light of the preceding model, for a probe pulse arriving after the pump pulse, all of the triply resonant processes that can contribute to the fourth-order polarization in the direction of the probe second harmonic are shown in Figure 2.6. To be specific, in the case of hole burning, we take the two pump field envelopes to overlap in time and be peaked at time $t = 0$, while the two probe field envelopes are also taken to overlap in time and peak at a later time $t = T$. For the present, we leave the pulse lengths unspecified other than stipulating that the pump and probe pulses do not overlap. In the general case of fourth-order photon-echo spectroscopy, which can be treated by the same formalism outlined below for fourth-order hole burning, one would temporally (and usually spatially) separate all of the pulses, as illustrated in Figure 2.5. Of the diagrams shown in Figure 2.6, only diagrams (a) and (b) produce the rephasing that is characteristic of techniques such as hole burning and photon echoes (Rephasing will only occur if there are two periods in which the phase of the density matrix evolves oppositely, e.g., a period in which the system is described by the coherence ρ_{ab} and another period in which it is described by the coherence ρ_{ba}). These rephasing processes dominate the others, which will be neglected in our calculations. The two rephasing diagrams yield the following contribution (labelled with the subscript 1γ to indicate that it is due to processes involving the one-photon resonance between states $|a\rangle$ and $|b\rangle$) to the fourth-order response function:

$$\begin{aligned} R^{(4)}_{1\gamma}(t_4, t_3, t_2, t_1) = \eta\, \mu_{ai}\mu_{ib}\mu_{ba}\mu_{ab}\mu_{ba} \left(\frac{i}{\hbar}\right)^4 \langle G_{ia}(t_4 + t_3 + t_2 + t_1, t_3 + t_2 + t_1) \\ \times G_{ba}(t_3 + t_2 + t_1, t_2 + t_1)\, [\, G_{bb}(t_2 + t_1, t_1) + G_{aa}(t_2 + t_1, t_1)\,]\, G_{ab}(t_1, 0)\rangle, \end{aligned} \tag{2.33}$$

where $G_{mn}(t_j, t_i)$ describes the evolution of the density operator $|m\rangle\langle n|$ (or equivalently the density operator matrix element ρ_{mn}) from time t_i to time t_j under the interaction of the system and system-bath interaction Hamiltonians. For resonantly excited off-diagonal

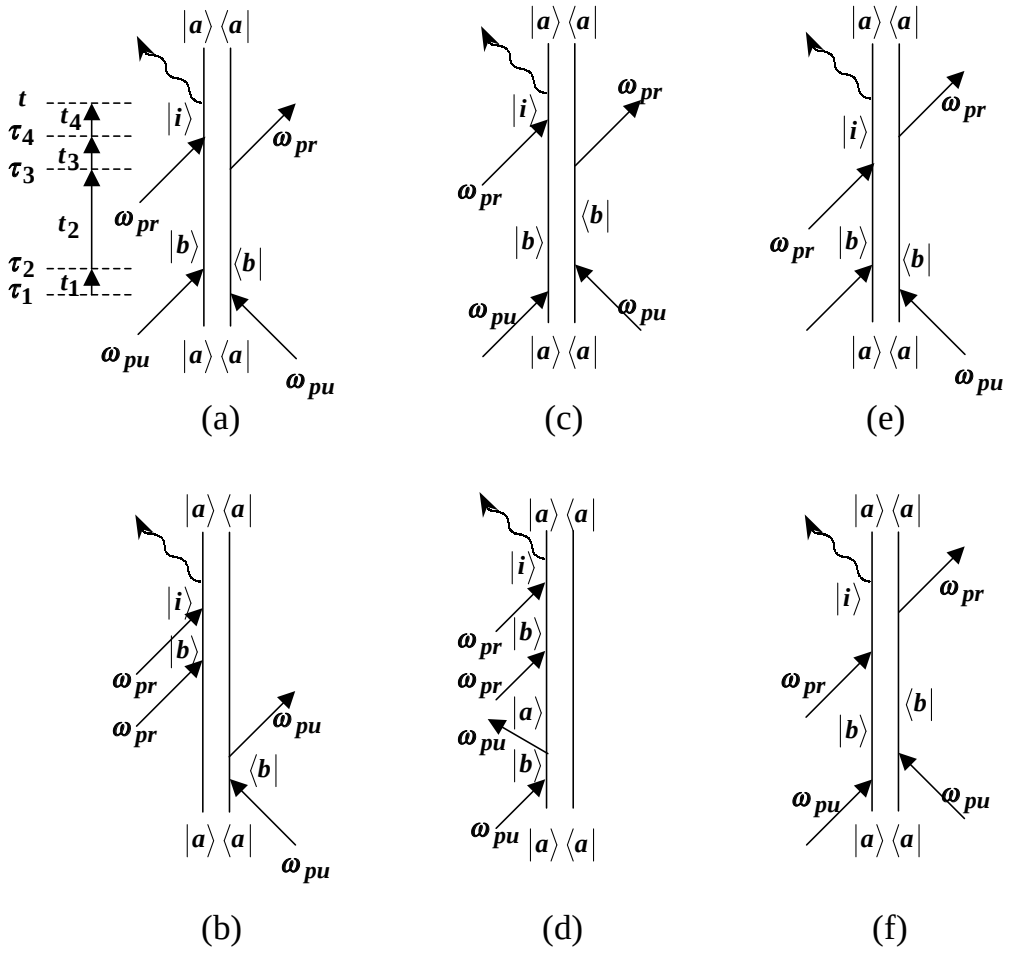

Figure 2.6: Double-sided Feynman diagrams contributing to the fourth-order response function of the system shown in Figure 2.4.

elements ($m \neq n$), these terms are determined by substituting Eqs. (2.19) and (2.20) into Eq. (2.23):

$$\begin{aligned} G_{mn}(t_j, t_i) &= \langle m|\hat{U}(t_j, t_i)|m\rangle\langle n|\hat{U}^{\dagger}(t_j, t_i)|n\rangle \\ &= \langle m|\exp_{-}\left[\frac{i}{\hbar}\int_{t_i}^{t_j} dt\ \left(\hat{H}_s + \hat{H}_{sb}^{\dagger}\right)\right]|m\rangle\langle n|\exp_{+}\left[+\frac{i}{\hbar}\int_{t_i}^{t_j} dt\ \left(\hat{H}_s + \hat{H}_{sb}\right)\right] \end{aligned} \quad (2.34)$$

where exp_{-} indicates a negative time-ordered exponential. The response of the system to far-off-resonance excitation is assumed to be instantaneous. The evolution of the diagonal terms is determined from the master equation (2.31). The angled brackets in Eq. (2.33) indicate a trace over the stochastic processes modelling the system-bath interaction. Via

the equivalence of temporal and ensemble averages, this trace is equivalent to a trace over the states of the system and bath.

To include the fact expressed in the master equation (2.31) that population decays from the state $|b\rangle$ to the state $|a\rangle$, we must add to the sum $G_{bb}(t_2+t_1,t_1)+G_{aa}(t_2+t_1,t_1)$ in the square brackets of Eq. (2.33) a term $-G_{aa,bb}(t_2+t_1,t_1)$ that describes the decay of the population $|b\rangle\langle b|$ in the diagram of Figure 2.6a to $|a\rangle\langle a|$. (The minus sign arises from the fact that the evolution of this term is determined initially by the first two interactions of the diagram of Figure 2.6a and then, after relaxation from $|b\rangle\langle b|$ to $|a\rangle\langle a|$, by the evolution specified after the first two interactions of Figure 2.6b. In terms of the translation of a Feynman diagram to a mathematical equation, each interaction from the left carries a factor of -1 compared to a factor from the right, and this extra term has three such interactions on the bra side of the density matrix, rather than the two such interactions in Figures 2.6a and 2.6b.) From the solution (Eq. (2.32)) of the master equation (2.31), we see that $G_{aa}(t_j,t_i)=1$, $G_{bb}(t_j,t_i)=\exp\left[-\gamma_b(t_j-t_i)\right]$, and $G_{aa,bb}(t_j,t_i)=1-\exp\left[\gamma_b(t_j-t_i)\right]$. Therefore,

$$G_{aa}(t_2+t_1,t_1)+G_{bb}(t_2+t_1,t_1)-G_{aa,bb}(t_2+t_1,t_1)=2e^{-\gamma_b t_2}. \tag{2.35}$$

There are two types of off-diagonal terms whose evolution is of interest: the non-resonant coherences ρ_{ia} and the resonant coherences ρ_{ba}. As noted above, for the non-resonant coherences we assume an instantaneous response

$$G_{ia}(t_j,t_i)=g\,\delta(t_j-t_i). \tag{2.36}$$

The evolution of the resonant terms of the density matrix are determined by using the model Hamiltonians of the previous section in Eq. (2.34):

$$\begin{aligned} G_{mn}(t_2,t_1) &= \theta(t_2-t_1)\exp\Bigg[-(\gamma_m/2+\gamma_n/2)(t_2-t_1) \\ &\qquad -i(\omega_m-\omega_n)(t_2-t_1)-\frac{i}{\hbar}\int_{t_1}^{t_2}dt\;\hbar\Big(\Delta_m(t)-\Delta_n(t)\Big)\Bigg], \end{aligned} \tag{2.37}$$

where $\theta(t)$ is the Heaviside step function

$$\theta(t)=\begin{cases} 1 & , \quad t>0 \\ 0 & , \quad t<0 \end{cases}. \tag{2.38}$$

Inserting Eqs. (2.35), (2.36), and (2.37) into Eq. (2.33) yields

$$R_{1\gamma}^{(4)}(t_4,t_3,t_2,t_1) = A\,\delta(t_4)\,e^{-\gamma_b t_2}\,e^{-\gamma_b(t_1+t_3)/2}e^{-i\omega_{ba}(t_3-t_1)}C(t_3,t_2,t_1), \tag{2.39}$$

where $A = 2\eta\,\mu_{ai}\mu_{ib}\mu_{ba}\mu_{ab}\mu_{ba}\left(\frac{i}{\hbar}\right)^4 g$, and

$$C(t_3,t_2,t_1) = \left\langle \exp\left\{-i\left[\int_{t_2+t_1}^{t_3+t_2+t_1} d\tau\;\Delta_{ba}(\tau) - \int_0^{t_1} d\tau\;\Delta_{ba}(\tau)\right]\right\}\right\rangle. \tag{2.40}$$

Comparison with Eq. (2.23) shows that $C(t_3,t_2,t_1)$ is just the five-point correlation function of the dipole operator, except that we have stripped out all constants and the time-dependent terms that do not originate from the system-bath interaction Hamiltonian. In general, a fourth-order process measures a five-point correlation function, but our assumption of an instantaneous response to the nonresonant fourth field term means that, for our model, the fifth point is equal to the fourth point (i.e., $t_4 = 0$), which reduces the correlation function to a four-point correlation function (described by three delays t_1, t_2, and t_3). By stripping out the exponential decay due to the system Hamiltonian, we are left with a function that describes the evolution of the correlations of the dipole operator due to the interactions of the system with the bath. In particular, if the autocorrelation of the function $\Delta_{ba}(\tau)$ decays on a timescale much longer than $t_3+t_2+t_1$, then

$$\begin{aligned} C(t_3,t_2,t_1) &\approx \left\langle \exp\left\{-i\Delta_{ba}(0)\left[\int_{t_2+t_1}^{t_3+t_2+t_1} d\tau - \int_0^{t_1} d\tau\right]\right\}\right\rangle \\ &= \langle \exp\{-i\Delta_{ba}(0)\,[((t_3+t_2+t_1)-(t_2+t_1))-((t_1)-0)]\}\rangle \\ &= 1, \end{aligned} \tag{2.41}$$

and there is no significant loss of coherence due to interactions of the system with the bath.

To go further we need to make assumptions about the stochastic fluctuations in the system eigenfrequencies produced by the bath. We suppose that the perturbations of the bath can be split into processes on three timescales:

$$\Delta_{ba}(t) = \Delta_s(t) + \Delta_i(t) + \Delta_f(t), \tag{2.42}$$

where the functions labelled s, i, and f refer respectively to slow perturbations with correlation times that are much longer than all relevant experimental timescales, intermediate

perturbations with correlation times shorter than the time between pump and probe pulses but longer than the pump and probe pulse lengths, and fast perturbations with correlation times much shorter than all pulse lengths. We assume that the slow coordinates are uncorrelated with the intermediate and fast ones, in which case

$$C(t_3, t_2, t_1) = \left\langle e^{-i\Delta_s(t_3 - t_1)} \right\rangle_{\Delta_s} C_D(t_3, t_2, t_1), \tag{2.43}$$

where $C_D(t_3, t_2, t_1)$ is the *dynamic* four-point correlation function

$$C_D(t_3, t_2, t_1) = \left\langle \exp\left\{ -i \left[\int_{t_2+t_1}^{t_3+t_2+t_1} d\tau \left(\Delta_i(\tau) + \Delta_f(\tau)\right) - \int_0^{t_1} d\tau \left(\Delta_i(\tau) + \Delta_f(\tau)\right) \right] \right\} \right\rangle. \tag{2.44}$$

To understand the significance of Eq. (2.43), we note that the slow variables can include static contributions to the system-bath interaction. Static perturbations account for such effects as the Doppler width of an atomic vapor or the different local environments of impurities in a crystal, two traditional inhomogeneously broadened systems. Eq. (2.43) shows that in the optical processes considered here, the effects of inhomogeneous broadening are eliminated at $t_3 = t_1$. For $|t_3 - t_1|$ greater than the width of the instantaneous distribution of the slow coordinates, the rapidly oscillating term $e^{-i\Delta_s(t_3 - t_1)}$ averages to zero. Physically, oscillators in different environments (and consequently having different resonant frequencies) can only oscillate coherently with one another for a time corresponding to the inverse of the total width of the resonant feature constituted by those oscillators. In the case of an inhomogeneously broadened system, this width is dominated by essentially static perturbations by the bath. If the evolution of the individual oscillators induced by an initial resonant excitation is reversed, then at $t_3 \approx t_1$, the oscillators at different frequencies (in different local environments) will all be in phase as long as oscillators at each frequency have not yet decohered with oscillators at the same frequency (irreversible decoherence). The oscillators at different frequencies can all radiate coherently at this time ($t_3 \approx t_1$). However, after a time corresponding to the inverse of the frequency-domain width of the static distribution of coordinates the oscillators at different frequencies will again be out of phase with one another. In other words, an inhomogeneously broadened system rephases at $t_3 \approx t_1$, but the resulting echo only lasts for a time of about the inverse inhomogeneous linewidth, as is

known from derivations of the photon echo starting from the optical Bloch equations [18]. Interaction between the probe field and the material excitation at this time will basically upconvert the rephased polarization and create a material polarization at $2\omega_{pr}$ that gives rise to the detected signal at $2\omega_{pr}$. We assume that the system is predominantly inhomogeneously broadened within the spectral range of interest, as this is the expected case for the Si(111)7×7 surface, given the different local environments of the different adatoms and the broad linewidth (of order 1 eV) of the feature around a fundamental photon energy of 1 eV in the second-harmonic generation spectrum of Si(111)7×7. For simplicity, we treat the system as having a uniform instantaneous distribution g_s of values of $\Delta_s(t)$, in which case Eq. (2.43) becomes

$$C(t_3, t_2, t_1) = g_s \delta(t_3 - t_1)\, C_D(t_3, t_2, t_1). \tag{2.45}$$

This is equivalent to the assumption in the continuous wave case that the distribution $g(\omega_{ba})$ is much broader than the homogeneous linewidth Γ_{ba} and so can be pulled outside the integral in Eq. (2.12). Finally, inserting Eq. (2.45) in Eq. (2.39), we obtain for the fourth-order response function

$$R^{(4)}_{1\gamma}(t_4, t_3, t_2, t_1) = A\, g_s\, \delta(t_4)\delta(t_3 - t_1)\, e^{-\gamma_b t_2}\, e^{-\gamma_b (t_1+t_3)/2} e^{-i\omega_{ba}(t_3 - t_1)} C_D(t_3, t_2, t_1). \tag{2.46}$$

Inserting the preceding in Eq. (2.27) and integrating over t_4 and t_3 yields for the fourth-order polarization

$$\begin{aligned} P^{(4)}(t) = e^{i2\vec{k}_{pr}\cdot\vec{r}} \int_0^\infty dt_2 \int_0^\infty dt_1 A\, g_s\, e^{-\gamma_b t_2}\, e^{-\gamma_b t_1} C_D(t_1, t_2, t_1) \\ \times e^{i(\omega_{pr} - \omega_{pu})t_1} \mathcal{E}_{pr}(t)\mathcal{E}_{pr}(t - t_1)\mathcal{E}_{pu}(t - t_2 - t_1)\mathcal{E}^*_{pu}(t - t_2 - 2t_1). \end{aligned} \tag{2.47}$$

Only at this point do we need to make assumptions about the pulse lengths. In particular, for hole burning we assume that the pulse envelopes are long compared to the timescale of the decay time of $C_D(t_1, t_2, t_1)$ in t_1. This will be seen below to be equivalent to assuming that the pulse lengths are greater than the homogeneous dephasing time. (In contrast, in the case of photon echoes, one tries to use pulses that are shorter than the decay time of $C_D(t_1, t_2, t_1)$ in t_1.) From the perspective of the field envelopes, the decay of $C_D(t_1, t_2, t_1)$

is virtually instantaneous at $t_1 \approx 0$, and the dependence of the fields on t_1 can be neglected in the integrand:

$$P^{(4)}(t) = e^{i2\vec{k}_{pr}\cdot\vec{r}} A\, g_s\, \mathcal{E}_{pr}^2(t) \int_0^\infty dt_2 \int_0^\infty dt_1\, e^{-\gamma_b(t_2+t_1)} C_D(t_1,t_2,t_1)\, e^{i(\omega_{pr}-\omega_{pu})t_1}\, |\mathcal{E}_{pu}(t-t_2)|^2 \,. \tag{2.48}$$

In contrast, for both hole burning and photon-echo spectroscopy, we assume that the electric-field envelopes are short compared to the decay time of $C_D(t_1,t_2,t_1)$ in t_2. In this case, the fields appear approximately as delta functions from the perspective of the variation of $C_D(t_1,t_2,t_1)$ in t_2, so we can neglect the variation of $C_D(t_1,t_2,t_1)$ with respect to t_2 in the integrand:

$$P^{(4)}(t) = e^{i2\vec{k}_{pr}\cdot\vec{r}} A\, g_s\, \mathcal{E}_{pr}^2(t) \left[\int_0^\infty dt_2\ |\mathcal{E}_{pu}(t-t_2)|^2 \right] e^{-\gamma_b T} \tilde{C}'_D(\omega_{pr}-\omega_{pu},T), \tag{2.49}$$

where

$$\tilde{C}'_D(\omega_{pr}-\omega_{pu},T) = \int_0^\infty dt_1\ e^{i(\omega_{pr}-\omega_{pu})t_1}\, e^{-\gamma_b t_1} C_D(t_1,T,t_1) \tag{2.50}$$

and T is the delay between the peaks of the pump and probe pulses as shown in Figure 2.5. It is worth reiterating that our only assumptions about the pulse lengths regard their lengths relative to the decay times of the correlation function $C_D(t_1,t_2,t_1)$ in t_1 and t_2.

In the most general case of photon-echo spectroscopy, we use four separate pulses as shown in Figure 2.5. The only difference in our assumptions about the pulse lengths is that the field envelopes are assumed to be much shorter than the decay time of $C_D(t_1,t_2,t_1)$ in t_1. If we approximate these short pulses by delta functions at times $t = -\tau_{pu}$, 0, T, and $T+\tau_{pr}$ (e.g., the last pulse would be given by $\mathcal{E}_{pr,2}(t) = \mathcal{E}_{pr}\delta(t-T-\tau_{pr})$), respectively, then at $\tau_{pu} = \tau_{pr} = \tau$, Eq. (2.47) yields

$$P^{(4)}(t) \propto \mathcal{E}_{pr}^2 |\mathcal{E}_{pu}|^2 \delta(t-T-\tau) e^{-\gamma_b(T+\tau)} C_D(\tau,T,\tau). \tag{2.51}$$

We will refer to the case in which the delay between the second and third pulses is nonzero ($T \neq 0$) as the stimulated photon echo and the case of $T = 0$ as the simple photon echo, as the latter is the case that is usually treated in elementary introductions to photon-echo spectroscopy in which there is also no fourth input field since the case of usual interest is the

photon echo from the bulk. As seen from Eqs. (2.49), (2.50), and (2.51), the contribution of the fourth-order polarization to the hole-burning signal is simply proportional to the Fourier transform with respect to τ of the product of $\exp(-\gamma_b \tau)$ and the dynamic correlation function $C_D(\tau, T, \tau)$ that appears in the fourth-order polarization of the photon echo.

To clarify the connection with simpler pictures of hole burning, as in Section 2.3.1, and photon-echo spectroscopy, we consider the simple case of a system in which there is a strict separation of timescales, so that the slow fluctuations in Eq. (2.42) for the system-bath interaction are static and the intermediate-timescale fluctuations are zero. If the random perturbations Δ_f are sufficiently weak, then for times $t_2 - t_1 \gg \tau_c$, where τ_c is the correlation time of the fluctuations of Δ_f, it can be shown that $\exp\left[-\frac{i}{\hbar}\int_{t_1}^{t_2} dt\, \Delta_f(t)\right] = \exp\left[-(t_2 - t_1)/T_2\right]$, where T_2 is the (homogeneous) dephasing time [108, 109]. [‡] This is just the traditional picture of a Lorentzian homogeneous spectrum broadened into an inhomogeneous spectral feature. In this case, Eq. (2.44) for the dynamic four-point correlation function yields

$$C_D(t_3, t_2, t_1) = e^{-(t_3 + t_1)/T_2}, \tag{2.52}$$

and we can drop the variable t_2. Inserting this in Eq. (2.50) yields (again dropping the variable T)

$$\tilde{C}'_D(\omega_{pr} - \omega_{pu}) = \frac{i}{(\omega_{pr} - \omega_{pu}) + i\,(\gamma_b + 2/T_2)}. \tag{2.53}$$

Therefore, the fourth-order polarization in a hole-burning measurement is characterized by a Lorentzian lineshape with a full-width at half-maximum of $4/T_2$. Likewise, we see from Eq. (2.51) that the fourth-order polarization in a measurement of a photon echo is given by

$$P^{(4)}(t) \propto \mathcal{E}_{pr}^2 |\mathcal{E}_{pu}|^2 \delta(t - T - \tau) e^{-\gamma_b T} e^{-(\gamma_b + 2/T_2)\tau}. \tag{2.54}$$

The signal that is detected (at time $T + \tau$) in a photon-echo experiment is proportional to $\left|P^{(4)}\right|^2$, so the photon-echo signal decays with respect to τ as $e^{-(2\gamma_b + 4/T_2)\tau}$. Excluding

[‡] This is a simple consequence of a perturbation analysis of the Liouville equation (Eq. (2.14)) in which the Hamiltonian appearing in that equation is the Hamiltonian $\hat{H}_{rand}$ describing the random perturbations of the system by the bath under the following set of assumptions: 1. the random perturbations are fluctuations that average to zero ($\langle \hat{H}_{rand}(t) \rangle = 0$); 2. the random processes are stationary ($\frac{\partial}{\partial t}\langle \hat{H}_{rand}(t)\hat{H}_{rand}(t+\tau)\rangle = 0$); 3. the random process are random with a correlation time τ_c ($\langle \hat{H}_{rand}(t)\hat{H}(t+\tau)\rangle = 0$ for $\tau > \tau_c$); 4. the perturbations are sufficiently weak that we can limit ourselves to second-order perturbation theory [108, 109].

effects due to population relaxation, the rate of decay of the photon-echo signal is four times the homogeneous dephasing rate $1/T_2$, exactly as found in elementary treatments of photon echoes.

Eq. (2.44) for the dynamic four-point correlation function shows that, in the general case ($\Delta_i \neq 0$), both hole burning and the stimulated photon echo are sensitive to perturbations of the system by the bath on intermediate timescales through their T-dependence. A simple photon echo is sensitive to dynamics on intermediate timescales only if the delay τ becomes comparable to the correlation time of those dynamics. A stimulated photon echo reflects the presence of system-bath interactions on multiple timescales in an echo decay rate with respect to τ that changes when T changes [110, 111] (In the absence of intermediate timescale interactions, fixing T at $T = T'$ yields the same exponential dependence of the echo decay on τ as is seen when T is fixed at $T = T'' \neq T'$). In hole-burning measurements the presence of multiple timescales is reflected in a T-dependent hole width, a phenomenon known as spectral diffusion [112, 113]. However, as hole-burning measurements are performed with pulses that are long compared to the τ-dependence of the dynamic correlation function $C_D(\tau, T, \tau)$, hole-burning measurements may yield apparent homogeneous dephasing times shorter than those measured by photon-echo measurements if there are dynamics on timescales intermediate between the lengths of the pulses used in a photon-echo measurement and the length of the pump and probe pulses used in a hole-burning measurement. Likewise, the definition of the fast fluctuations that comprise the system-bath interaction will depend on the length of the pulses used in an experiment.

The Second-Harmonic Hole-Burning Signal

The preceding discussion illustrates the essential features of the fourth-order contribution to a second-harmonic hole-burning measurement, but the signal that is measured in a hole-burning experiment is the result of interference between the fourth-order polarization $P^{(4)}(t)$ written above and the second-order polarization $P^{(2)}(t)$, which also gives rise to a signal at frequency $2\omega_{pr}$ in the same direction as the fourth-order signal. In the simple model of

Figure 2.4,

$$P^{(2)}(t) = P^{(2)}_{1\gamma}(t) + P^{(2)}_{2\gamma}(t), \tag{2.55}$$

where the terms labelled 1γ and 2γ are due respectively to transitions in the unprimed levels, attributed to a one-photon resonance, and those in the primed levels, attributed to a two-photon resonance. Calculations of $P^{(2)}_{1\gamma}(t)$ and $P^{(2)}_{2\gamma}(t)$ are performed in the same manner as for $P^{(4)}(t)$. The 1γ contribution to $P^{(2)}(t)$ is given by

$$P^{(2)}_{1\gamma}(t) = e^{i(2\vec{k}_{pr}\cdot\vec{r}-2\omega_{pr})t}\int_0^\infty dt_2 \int_0^\infty dt_1 R^{(2)}_{1\gamma}(t_2,t_1)e^{i(2\omega_{pr}t_2+\omega_{pr}t_1)}\mathcal{E}_{pr}(t-t_2-t_1)\mathcal{E}_{pr}(t-t_2), \tag{2.56}$$

where

$$R^{(2)}_{1\gamma}(t_2,t_1) = \mu_{ai}\mu_{ib}\mu_{ba}\left(\frac{i}{\hbar}\right)^2 \langle G_{ia}(t_2+t_1,t_1)G_{ba}(t_1,0)\rangle\,. \tag{2.57}$$

Based on our model for the system, we can write

$$R^{(2)}_{1\gamma}(t_2,t_1) = \mu_{ai}\mu_{ib}\mu_{ba}\left(\frac{i}{\hbar}\right)^2 g\,\delta(t_2)\left\langle \exp\left\{-i\omega_{ba}t_1 - i\int_0^{t_1} dt'\Delta_{ba}(t') - \gamma_b t_1/2\right\}\right\rangle. \tag{2.58}$$

As above, taking a uniform instantaneous distribution g_s for the perturbation $\Delta_s(t)$, yields

$$\begin{aligned} R^{(2)}_{1\gamma}(t_2,t_1) &= \mu_{ai}\mu_{ib}\mu_{ba}\left(\frac{i}{\hbar}\right)^2 g\,g_s\,\delta(t_2)\delta(t_1) \\ &\quad\times\left\langle \exp\left\{-i\omega_{ba}t_1 - i\int_0^{t_1} dt'\,(\Delta_i(t')+\Delta_f(t')) - \gamma_b t_1/2\right\}\right\rangle. \end{aligned} \tag{2.59}$$

Inserting this in Eq. (2.56) yields

$$P^{(2)}_{1\gamma}(t) = e^{i2\vec{k}_{pr}\cdot\vec{r}}\mu_{ai}\mu_{ib}\mu_{ba}\left(\frac{i}{\hbar}\right)^2 g\,g_s\,\mathcal{E}^2_{pr}(t). \tag{2.60}$$

Adding the second- and fourth-order (Eq. (2.49)) terms due to the one-photon resonance, we obtain

$$P^{(2)}_{1\gamma}(2\omega_{pr},t) = P_{1\gamma,0}(2\omega_{pr},t)(1-\Delta n_{ba}(\omega_{pr}-\omega_{pu},T,t)), \tag{2.61}$$

where

$$P^{(2)}_{1\gamma,0}(2\omega_{pr},t) = e^{i2\vec{k}_{pr}\cdot\vec{r}}\mu_{ai}\mu_{ib}\mu_{ba}\left(\frac{i}{\hbar}\right)^2 g g_s \mathcal{E}^2_{pr}(t) \tag{2.62}$$

is the polarization at frequency $2\omega_{pr}$ in the absence of the pump, and

$$\Delta n_{ba}(\omega_{pr}-\omega_{pu},T,t)=2\mu_{ab}\mu_{ba}\left(\frac{1}{\hbar}\right)^2\tilde{C}'_D(\omega_{pr}-\omega_{pu},T)\,e^{-\gamma_b T}\int_0^\infty dt_2\,|\mathcal{E}_{pu}(t-t_2)|^2\,. \quad (2.63)$$

For non-overlapping pump and probe pulses (for which $\mathcal{E}(t-t_2)=0$ when $t_2<0$), the lower limit in the integral can be extended to $-\infty$, and $\Delta n_{ba}(\omega_{pr}-\omega_{pu},T)$ then is independent of t. The notation Δn_{ba} is chosen in analogy to the term in Eq. (2.13), derived on the basis of a cw approach, due to the change in population induced by the pump. However, as discussed above, in the present approach, we have included the possibility of spectral diffusion due to perturbations of the system by the bath on intermediate timescales. The 2γ contribution to $P^{(2)}$ is described by

$$P^{(2)}_{2\gamma}(2\omega_{pr},t)=e^{i2\vec{k}_{pr}\cdot\vec{r}}\mu_{a'b'}\mu_{b'i}\mu_{ia'}\left(\frac{i}{\hbar}\right)^2 g'g'_s\mathcal{E}^2_{pr}(t), \quad (2.64)$$

where g' and g'_s are the terms for the 2γ process corresponding respectively to the terms g and g_s of Eqs. (2.36) and (2.45).

Based on our model, in which the 1γ and 2γ processes are uncoupled and in which the pump does not significantly change the populations of $|a'\rangle$ and $|b'\rangle$, to fourth order the polarization at the second harmonic of the probe is now given by

$$P(2\omega_{pr},\omega_{pu},T,t)=P^{(2)}_{1\gamma,0}(2\omega_{pr},t)\,[1-\Delta n_{ba}(\omega_{pr}-\omega_{pu},T,t)]+P^{(2)}_{2\gamma}(2\omega_{pr},t). \quad (2.65)$$

The signal, $S(2\omega_{pr},\omega_{pu},T)$, that is ultimately detected is the integral of the radiated intensity:

$$S(2\omega_{pr},\omega_{pu},T)\propto\int_{-\infty}^{\infty}dt\,|P(2\omega_{pr},\omega_{pu},T,t)|^2\,. \quad (2.66)$$

Inserting Eqs. (2.61) and (2.64) into this equation yields

$$S(2\omega_{pr},\omega_{pu},T)=\int_{-\infty}^{\infty}dt\,|\mathcal{E}_{pr}(t)|^4\,|\alpha_{1\gamma}[1-\Delta n_{ba}(\omega_{pr}-\omega_{pu},T,t)]+\alpha_{2\gamma}|^2\,, \quad (2.67)$$

where $\alpha_{1\gamma}$ and $\alpha_{2\gamma}$ are constants of proportionality. As explained immediately after Eq. (2.63), if the delay between pump and probe exceeds the pulse lengths, then we can rewrite Eq. (2.67) as

$$\begin{aligned}S(2\omega_{pr},\omega_{pu},T) &= |\alpha_{1\gamma}[1-\Delta n_{ba}(\omega_{pr}-\omega_{pu},T)]+\alpha_{2\gamma}|^2\int_{-\infty}^{\infty}dt\,|\mathcal{E}_{pr}(t)|^4\\ &\propto |\alpha_{1\gamma}[1-\Delta n_{ba}(\omega_{pr}-\omega_{pu},T)]+\alpha_{2\gamma}|^2\,, \quad (2.68)\end{aligned}$$

where

$$\Delta n_{ba}(\omega_{pr}-\omega_{pu},T)=2\mu_{ab}\mu_{ba}\left(\frac{1}{\hbar}\right)^2\tilde{C'}_D(\omega_{pr}-\omega_{pu},T)\,e^{-\gamma_b T}\int_{-\infty}^{\infty}dt\;|\mathcal{E}_{pu}(t)|^2\,. \tag{2.69}$$

We see explicitly that, other than a contribution from the population relaxation described by $e^{-\gamma_b T}$, $\Delta n_{ba}(\omega_{pr}-\omega_{pu},T)$ as a function of the detuning of the probe relative to the pump has the same shape as $\tilde{C}'_D(\omega_{pr}-\omega_{pu},T)$. Within the limits already discussed, by measuring $\Delta n_{ba}(\omega_{pr}-\omega_{pu},T)$ we measure the timescales for dynamic dephasing in the system of interest.

As discussed in the preceding section on the fourth-order polarization, in the case that there is a strict separation of the timescales of the perturbations of the system by the bath into very fast and slow timescales and the fast dynamics are due to a sufficiently weak perturbation, we find a Lorentzian form for $\tilde{C}'_D(\omega_{pr}-\omega_{pu},T)$. Inserting Eq. (2.53) in Eqs. (2.69)

$$\Delta n_{ba}(\omega_{pr}-\omega_{pu},T)=-i\,2\frac{|\mu_{ba}|^2}{\hbar^2}\left(\int_{-\infty}^{\infty}dt\,|\mathcal{E}_{pu}(t)|^2\right)\,e^{-\gamma_b T}\frac{1}{(\omega_{pr}-\omega_{pu})+i(\gamma_b+2\Gamma_{ba})}, \tag{2.70}$$

where $\Gamma_{ba}=1/T_2$ is the homogeneous dephasing rate. We see that Eqs. (2.68) and (2.70) yield the same functional form for the transient second-harmonic hole-burning signal as a function of detuning $\omega_{pr}-\omega_{pu}$ as does Eq. (2.13).

2.4 Experimental Setup

The experiments to be described rely on the ability to measure very weak, transient second-order signals over a range of a few thousand wave numbers from the dangling bonds of a well ordered Si(111)7×7 surface. At the powers used in these experiments, the signal can be as weak as tens of photon counts per second, which means that the sample must remain clean for the thousands of seconds that can be required for a single data scan. These constraints require both tunable femtosecond laser pulses and ultrahigh vacuum conditions.

A schematic representation of the UHV chamber is shown in Figure 2.7. The base pressure obtained within two days after baking the chamber was below 1.0×10^{-10} mbar.

Measurements were usually performed at pressures of $5.0 - 8.0 \times 10^{-11}$ mbar. A combined four-grid retarding-field low-energy electron diffraction (LEED)/Auger electron spectroscopy (AES) instrument (Perkin Elmer Φ15-120 LEED optics, Φ11-020 LEED electronics and Φ11-500A Auger system controller) allowed for *in situ* inspection of the sample surface condition.

The sample was mounted in the UHV chamber on a holder based on the design used in the group of U. Höfer [114]. A schematic of the holder is shown in Figure 2.8. The sample temperature could be controlled by resistive heating of the liquid-nitrogen-cooled sample. Cooling of the holder via a liquid N_2 flow cryostat maintained the temperature of the sample holder near the insulating sapphire plate at below 110 K even at the highest sample temperatures of over 1300 K. The sample temperature was measured with a type K (NiCr/NiAl) thermocouple attached by ceramic adhesive to a thin layer of the ceramic adhesive that was previously applied to the back of the sample to prevent direct contact between the thermocouple and sample. The thermocouple voltage was measured by the amplifier circuit shown in Figure 2.9 over the entire temperature range from 80 K to over 1300 K. The thermocouple readings at high temperatures were within ±10 K of the readings from an optical pyrometer.

The material used in these experiments was single-crystal, Czochralski-grown (Cz) Si (WaferNet, Inc.) doped with phosphorus (n-type) such that the resistivity was specified to be between 1 and 2 Ω cm, corresponding to a phosphorus concentration of $n_P \sim 3\times10^{15}$ cm^3. The nominally flat 4-inch diameter wafers were of 525 μm thickness and polished on a single side along the [111] direction. Samples of dimensions 50×10 mm^2 were cut from the wafers with a diamond scribe and mounted on the sample holder such that the $[2\bar{1}\bar{1}]$ crystallographic axis was perpendicular to the optical plane. The samples were blown free of dust with a rubber bulb and wiped with a piece of lens paper and a drop of reagent-grade methanol before being placed in the chamber. Any remaining contaminants were desorbed with the native oxide in the UHV chamber.

Clean, well ordered Si(111)7×7 surfaces were prepared in the UHV chamber by resistive heating and protected by passivation with hydrogen. During baking of the chamber at

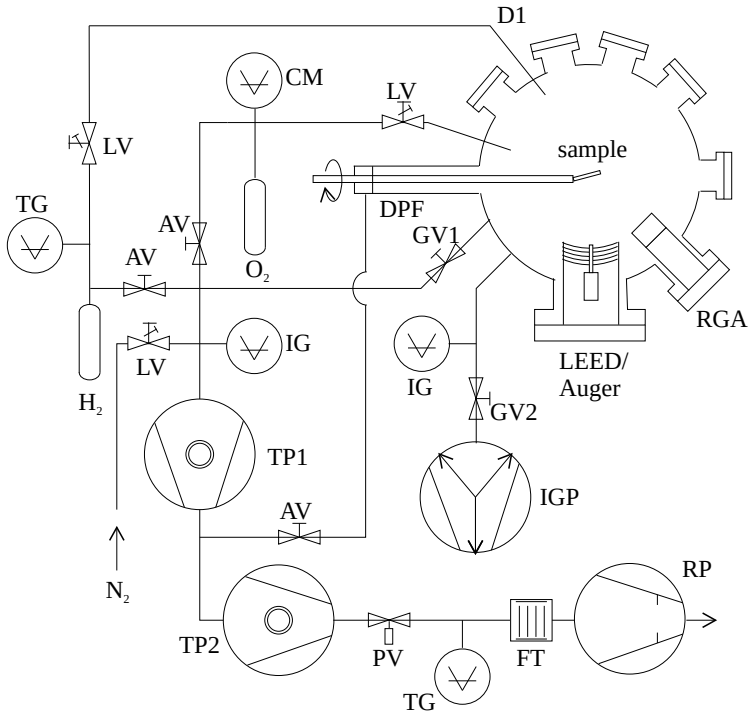

Figure 2.7: Schematic representation of the ultra-high vacuum system. The abbreviations are explained in Table 2.2.

IGP	Ion getter pump: Perkin-Elmer, 500 l/s
TP1, TP2	Turbomolecular pumps: Balzers TPU-240, 230 l/s; Pfeiffer TPU-110, 170 l/s
RP	Rotary vane pump: Edwards E2M-18
FT	Foreline trap
DPF	Differentially pumped feedthrough
RGA	Residual gas analyzer: Ametek Dycor LC100MS
IG	Ionization gauge
TG	Thermocouple gauge
CM	Capacitance manometer
D1	Doser with tungsten filament
PV	Pneumatic protection valve
LV	Leak valve
AV, GV	Angle valve, gate valve

Table 2.2: List of vacuum components represented in the schematic of the ultra-high vacuum system shown in Fig. 2.7.

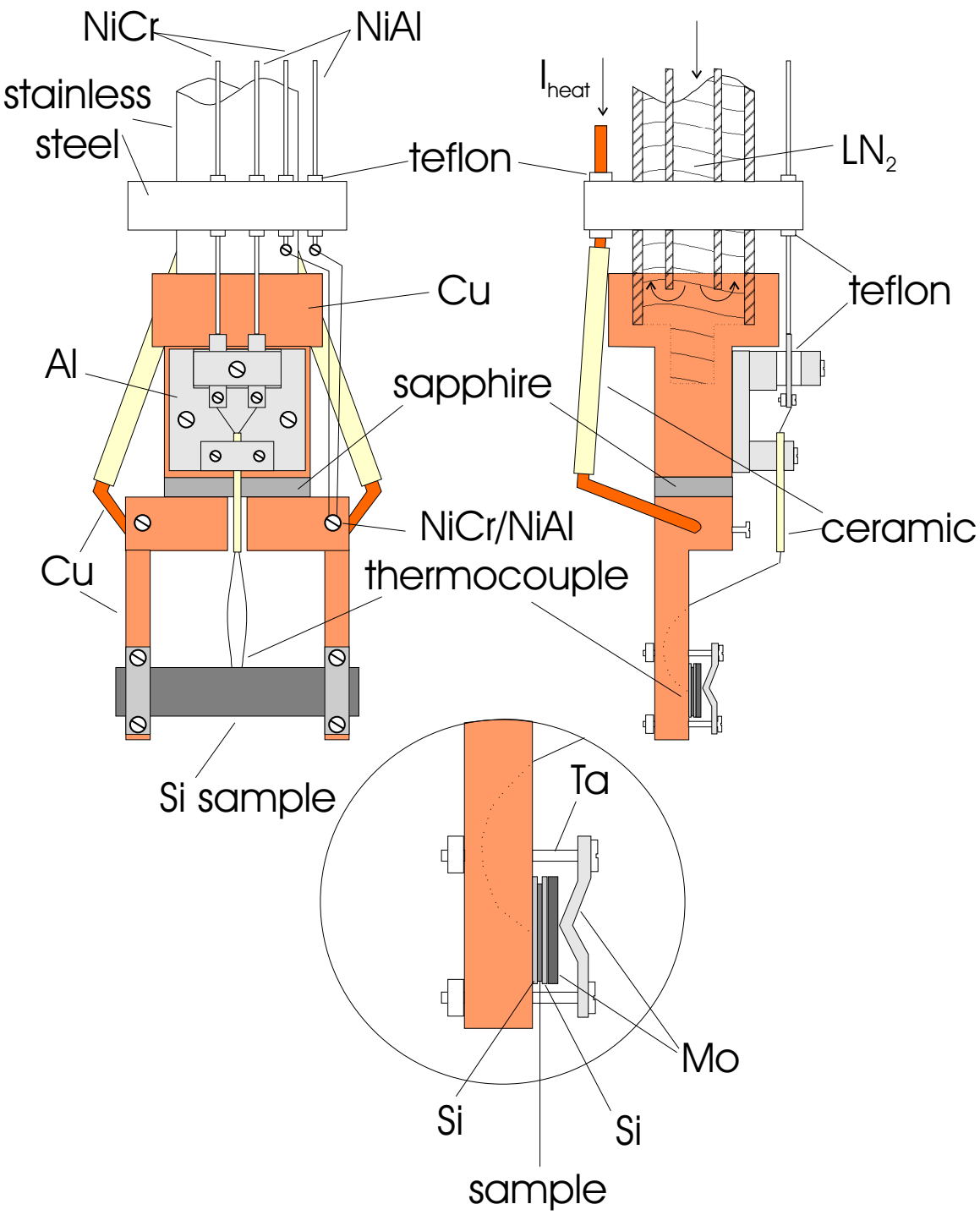

Figure 2.8: Schematic representation of the UHV sample holder based on the design in Reference [114].

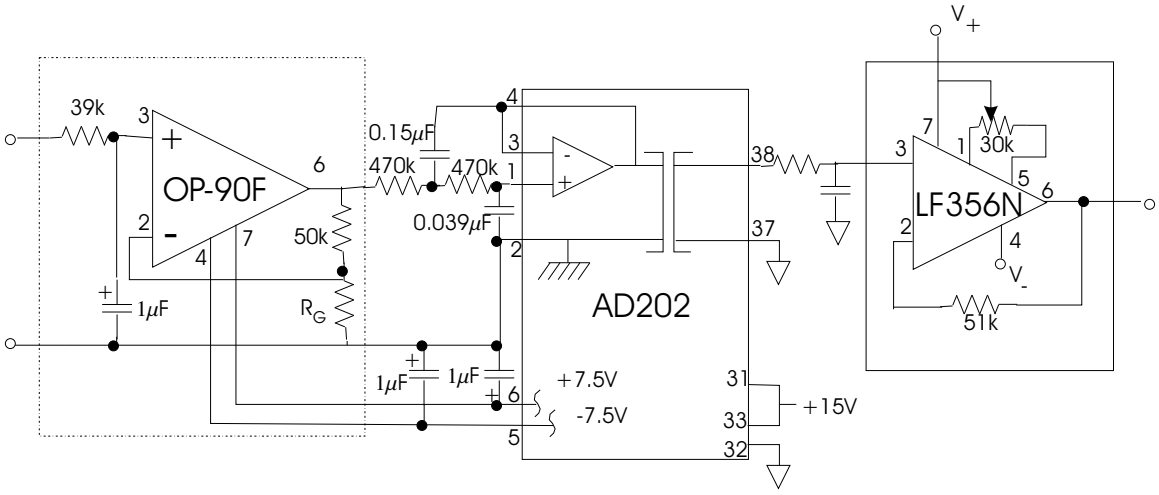

Figure 2.9: Diagram of the amplifier circuit used to measure the thermocouple voltage. The circuit consists of a precision low-voltage micropower operational amplifier followed by a unity gain isolation amplifier and an output buffer.

430 K, the sample temperature was maintained at about 550 K. After baking the chamber, the native oxide was removed from the sample by a series of heating ramps in which the sample temperature was increased at about 3.0 K/s and then decreased at about 1.5 K/s. The peak temperature of each current ramp was gradually increased so that the chamber pressure did not exceed 1×10^{-9} mbar, except at the highest temperatures, where the pressure did not exceed 3×10^{-9} mbar. The maximum sample temperature was about 1310 K. This procedure resulted in a clean, well ordered 7×7 reconstructed surface. A LEED image of the Si(111)7×7 surface at a primary electron energy of 91 eV is shown in Fig. 2.10. The AES spectrum in Fig. 2.11 shows that any impurities are below the detection limit of the Auger analyzer. To protect the sample surface from contamination by the constituents of the chamber background pressure between experiments, the sample surface was passivated by exposure to molecular hydrogen at a pressure of about 2×10^{-7} mbar in the presence of a hot tungsten filament ($T_W = 1800 \pm 75$ K) that dissociates the molecular hydrogen into its atomic form, which readily bonds with the dangling bonds of the Si(111)7×7 surface. The sample temperature was ramped to 1310 K at the same rates described above at the beginning of each day of measurements (so as to remove the passivating hydrogen and reorder the surface) and then after approximately 0.3 Langmuir ($1\,\mathrm{L} = 10^{-6}$ torr·s) exposure

Figure 2.10: LEED image of clean, reconstructed Si(111)7×7 surface.

to the background chamber pressure.

The optical layout for the SH hole-burning experiments is illustrated in Figure 2.12. All the measurements were carried out with fundamental photon energies of about 1.55 eV ($\lambda =$ 800 nm). This range was chosen both because it corresponds to the output of the Ti:sapphire amplifier described in Chapter 1, which contributed to stability and simplicity compared to any other choice of photon energy, and because it is in the spectral region in which the broad dangling-bond-derived resonance in the SHG spectrum of the Si(111)7×7 surface is strong and dominates other contributions to the second-order nonlinear susceptibility (See Figure 2.3). The pump beam was directly from the output of the amplifier. One minor problem with the laser system was that the broad (FWHM∼35 nm) seed pulses from the oscillator made it difficult to control the center wavelength of the amplifier output from one day to the next. Consequently, the pump center wavelength varied over a range from 798 nm to 810 nm. The probe beam was generated by doubling the signal (for positive probe detunings) or idler (for negative detunings) from the BBO-based OPG/OPA described in Chapter 1 in a second BBO crystal (length=2 mm, $\theta = 22.8°$, $\theta = 0°$). This readily produced probe pulses of 20 μJ, which was more than enough energy even after spectral filtering and traversal of many optical elements to yield the pulses of approximately 2 μJ needed for the experiments. A pair of prisms designed for compression of 800 nm pulses (i.e.,

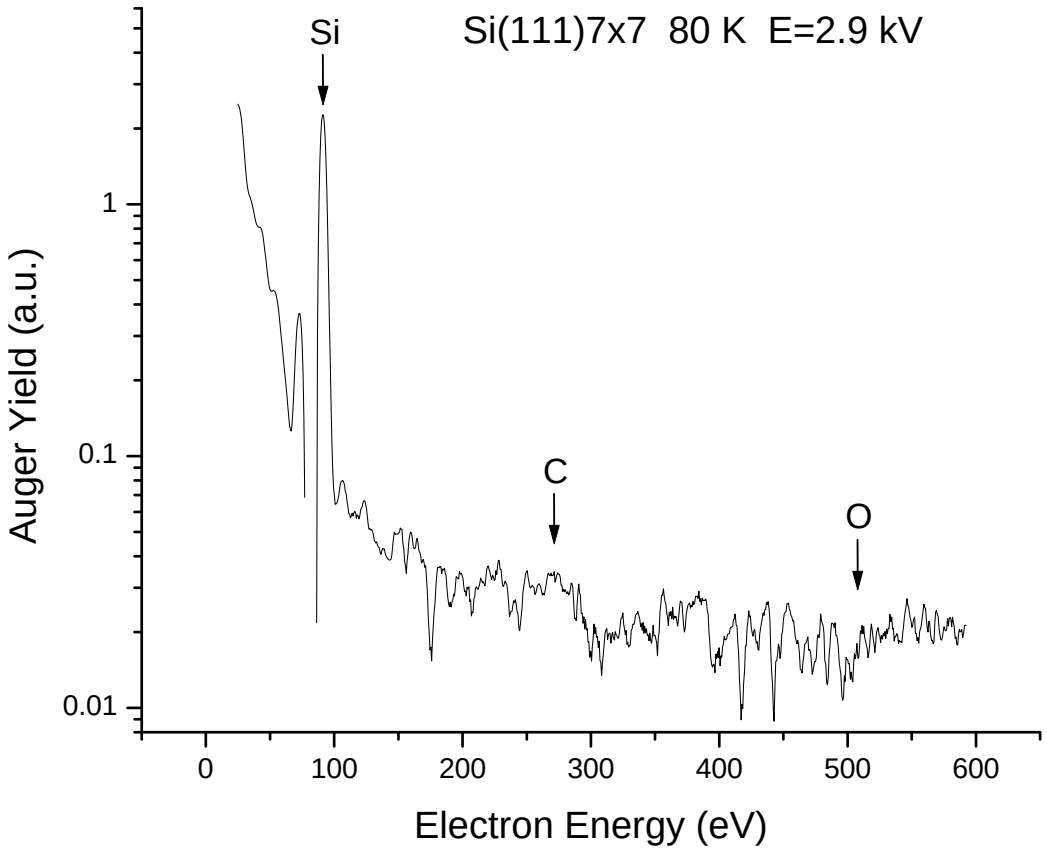

Figure 2.11: Auger electron spectrum of a clean Si(111)7×7 surface at 80 K obtained with a primary electron energy of 2.9 kV. The energies of electrons emitted from the silicon LMM, carbon KLL, and oxygen KLL transitions are indicated.

prisms cut at the Brewster angle for 800 nm radiation) compress the probe pulse, thereby providing nearly optimal temporal resolution and increasing the SHG signal intensity at a given signal fluence. To prevent degradation of the spectral resolution of the experiment, a slit (not shown) near prism Pr2 was used to reduce the bandwidth of the probe, since the processes of generation of signal and idler and their subsequent doubling can lead to significant increase of the probe bandwidth. Just before the UHV chamber, a fused silica plate was used to reflect part of the probe beam to a crystalline KTP sample of 5 mm thickness for normalization against fluctuations. In both the signal and reference arms, a combination of Schott glass filters and monochromators suppressed background light at frequencies other than the probe SH.

Since this investigation aims to compare the fluence-dependence of the sample dephasing

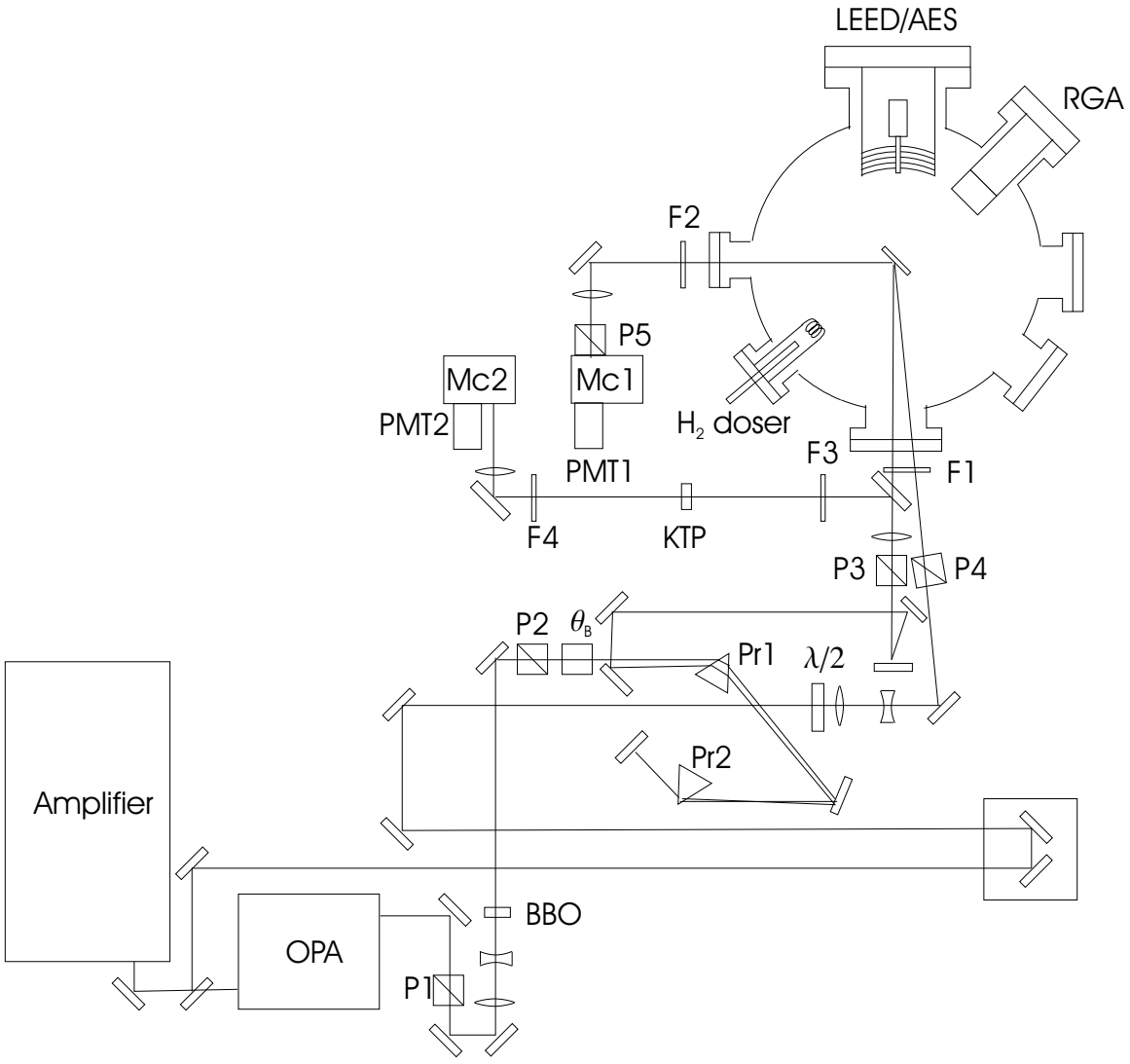

Figure 2.12: Optical layout for SH hole-burning measurements. The abbreviations refer to the following elements: BBO, crystal for doubling OPA signal or idler to produce probe; KTP, crystal for generating reference SHG; P1, Glan laser polarizer for separating signal and idler; P2, Glan laser polarizer for rejecting OPA output used to produce probe; P3 and P4, Glan laser polarizers for defining probe and pump input polarizations; P5, Glan Thompson polarizer; θ_B, Berek compensator; Pr1 and Pr2, probe compressor prisms; F1 and F3, Schott glass filters for blocking probe SH while transmitting fundamental beams; F2 and F4, Schott glass filters for blocking fundamental of probe and transmitting probe SH; Mc1 and Mc2, signal and reference monochromators.

dynamics, it is crucial to have an accurate measurement of the pump fluence in the probe region, especially as the pump spatial mode deviates somewhat from a TEM00 mode, the probe spatial mode often displays significant structure, and the spatial modes of both beams

vary from day to day. A flip-up mirror (not shown) immediately before the UHV chamber entry window was used to reflect the pump and probe beams at $\sim 90^\circ$ to a CCD camera positioned with its CCD array at the same distance from the mirror as was the sample. The pump energy was adjusted so that the most intense region containing 25% of the pump energy was located in an elliptical area of major and minor axes both approximately 1.3 mm perpendicular to the beam. Likewise, the probe beam was focused such that the most intense region contained about 60% of the probe energy in an elliptical area perpendicular to the beam of major and minor axes with a geometric mean of approximately 0.7 mm. With the pump and probe beams respectively oriented at 47° and 43° from the sample normal, their energies were adjusted such that, within the projections of the aforementioned ellipses onto the sample, the average pump fluence was set alternately to 1600, 800, 400, and 200 μJ/cm^2, while the average probe fluence was about 120 μJ/cm^2.

The preceding choices of beam sizes and angles allowed for sufficiently high signals at the fluences used but at the cost of some degradation of the temporal resolution of the experiments. For beams with Gaussian spatial and temporal profiles with the preceding spatial characteristics and with intensity envelopes of 100 fs FWHM, the FWHM of a SFG cross-correlation between the pump and probe beams is expected to be about 190 fs rather than 140 fs, as would be expected for pulses at the same incident angle (and as was observed if the beams were reduced in size so that transit effects became insignificant and the probe pulses were well compressed). Variations in the probe profile and suboptimal probe compression led to SFG cross correlations typically in the range of 200-250 fs. However, on account of hole-burning measurements being higher order than SFG, the temporal resolution of the hole-burning measurements was better than that of the SFG cross-correlation. For 100 fs (FWHM) pulses with Gaussian profiles at equal incidence angles, an instantaneous fourth-order response would result in a pulse-limited temporal resolution of 100 fs, rather than the 140 fs limit of the SFG cross-correlation. In practice, the temporal resolution of our measurements was typically about 200 fs.

The polarizations of the input pump and probe beams were p and s, respectively. With the input beams polarized perpendicularly to one another, no population gratings were

formed that might contribute to the probe SH signal. An analyzer in the signal detection arm was set to detect s polarization, so that the second-order nonlinear susceptibility was probed in the s-in/s-out polarization combination, and only the anisotropic element ($\chi^{(2)}_{\parallel\parallel\parallel}$) of the second-order nonlinear susceptibility was probed.

2.5 Experimental Results and Analysis

The ultimate goal of our experiments was the determination of the homogeneous dephasing time of the transitions giving rise to the broad dangling-bond-derived peak in the SHG spectrum of the clean Si(111)7×7 surface of Figure 2.3 at photon fundamental energies of about 1.5 eV. Hole burning is observed simply by comparing the probe SHG after the arrival of the pump pulse to the probe SHG before the arrival of the pump pulse over a range of probe-pump detunings. One can carry out complete temporal pump-probe scans and thereby obtain a picture of the temporal evolution of the spectral hole, which is determined by the evolution of the quantity $\Delta n_{ba}(\omega_{pr} - \omega_{pu}, T)$ with respect to T (See Eq. (2.68)). Such temporal scans provide valuable information about population dynamics and spectral diffusion. However, as seen in the discussion of Section 2.3, it is the value of $\Delta n_{ba}(\omega_{pr} - \omega_{pu}, T)$ at the smallest positive T that is relevant. As our primary interest is measurement of the fastest timescale dynamics to which we have access, we focus on measurements of the spectral hole in the probe SHG at the smallest times at which there is minimal overlap of the pump and probe pulses ($T \approx 200$ fs).

Extraction of an accurate measurement of the homogeneous dephasing time from the observed spectral hole requires ancillary measurements. As seen from the SHG spectrum from the passivated Si(111)7×7 surface of Figure 2.3, there is a second contribution to the SHG spectrum in the vicinity of 1.5 eV. The simple model of Section 2.3 yields Eq. (2.68) from which we clearly see that the second-harmonic hole-burning signal does not directly yield the function $\Delta n_{ba}(\omega_{pr} - \omega_{pu}, T)$. To determine $\Delta n_{ba}(\omega_{pr} - \omega_{pu}, T)$, we must determine the relative amplitude and phase of $\alpha_{2\gamma}$ and $\alpha_{1\gamma}$ of Eq. (2.68). In practice this is done by measuring the probe SHG as a function of exposure of the surface to hydrogen, which selectively passivates the dangling-bond feature. In particular, from measurements

at different wavelengths of the SHG signals corresponding to the completely unterminated surface, the completely terminated surface, and the partially terminated surface yielding the minimum SHG, one obtains two independent ratios that can be used to determine the two unknown quantities $|\alpha_{1\gamma}/\alpha_{2\gamma}|$ and $\phi_{2\gamma} = -i \ln\left(\frac{\alpha_{1\gamma}/\alpha_{2\gamma}}{|\alpha_{1\gamma}/\alpha_{2\gamma}|}\right)$. Once these relative amplitudes and phases are known, we can model our data. In particular, we find that we can fit most of our data with a simple, Lorentzian model for $\Delta n_{ba}(\omega_{pr} - \omega_{pu}, T)$. The two parameters for a Lorentzian fit are its amplitude and width. The latter is directly related to the homogeneous dephasing time T_2.

The discussion of the data is organized as follows. We begin with a presentation of temporal pump-probe scans in which we detect the evolution of the probe second harmonic as a function of delay relative to the pump. These measurements illustrate several important points. They indicate the extent of the validity of some of our assumptions made in Section 2.3. In particular, the temporal pump-probe scans show that we probe the system on timescales and with temporal resolution short relative to the population dynamics. These data also illustrate that at positive detunings a slightly more complicated picture of the surface electronic transitions is needed. Similar measurements on the hydrogen-terminated surface and linear reflectivity measurements also demonstrate that the pump-probe signals from the clean Si(111)7×7 surface are due primarily to surface rather than bulk processes. We then present the measurements of the probe SHG as a function of surface passivation that allow us to determine the relative amplitudes and phases of the two contributions to the probe SHG. These measurements also lead to a discussion of a complication due to a pump effect that persists on the millisecond timescale. Finally, we present data from the measurement of the spectral hole in the probe SHG at short delays and present fits to a simple, essentially cw model. The fit to the data reveals a pair of contributions to the hole-burning spectra. By measuring the spectral hole at the pump frequency at multiple pump fluences, we find a linear dependence of the homogeneous dephasing rate on the pump fluence.

2.5.1 Pump-Probe Second-Harmonic Generation

Figures 2.13 and 2.14 show the probe SHG signal as a function of delay relative to the pump pulse at several pump fluences for a pair of negative detunings and a pair of positive detunings, respectively. As noted in Section 2.4, the center wavelength of the pump pulses varied somewhat from day to day. However, these variations were within the full-width-at-half-maximum of the pump bandwidth, which was much narrower than all the spectral holes to be discussed later. Consequently, this variation in pump center wavelength was deemed insignificant. The main features of the data (except at the largest positive detuning, the data for which are displayed in Figure 2.14b) are the rapid initial change in the probe SH, which typically reaches its maximum deviation at a delay of about 200 fs, and the recovery of the signal on a timescale of about 500 fs. Except in magnitude, the data shown in Figures 2.13 and 2.14a are representative of the phenomena observed across the explored range of detunings. The data for different negative detunings show qualitatively similar recovery of the pump-induced decrease of the probe second harmonic as seen in Figure 2.13. At negative detunings different than those shown one only sees a change in the magnitude of the pump-induced decrease of the probe signal that diminishes at negative detunings of greater magnitude. The data of Figure 2.14a illustrate (ignoring for the moment the data for a pump fluence of 1600 μJ/cm^2 in Figure 2.14a) the typical recovery of the positively detuned probe second-harmonic signals. For all data except that of Figure 2.14b, the probe SHG quickly relaxes to a level below the unpumped level. The timescale for complete recovery of the signal was not fully investigated, but the signal remained at this decreased level up to the maximum measured time (data not shown) of tens of picoseconds. This latter observation was also made by Voelkmann *et al.* [15, 105]. This observation is not surprising given that the Si(111)7×7 surface electronic band structure is not highly dispersive and given the timescales of mechanisms for relaxation of excited carriers back to the ground state such as radiative recombination, which is expected to occur on nanosecond timescales.

With a dramatic pump-induced increase in the probe SH signal, the data for the largest positive detuning (Figure 2.14b) shows qualitatively different behavior than the data at all

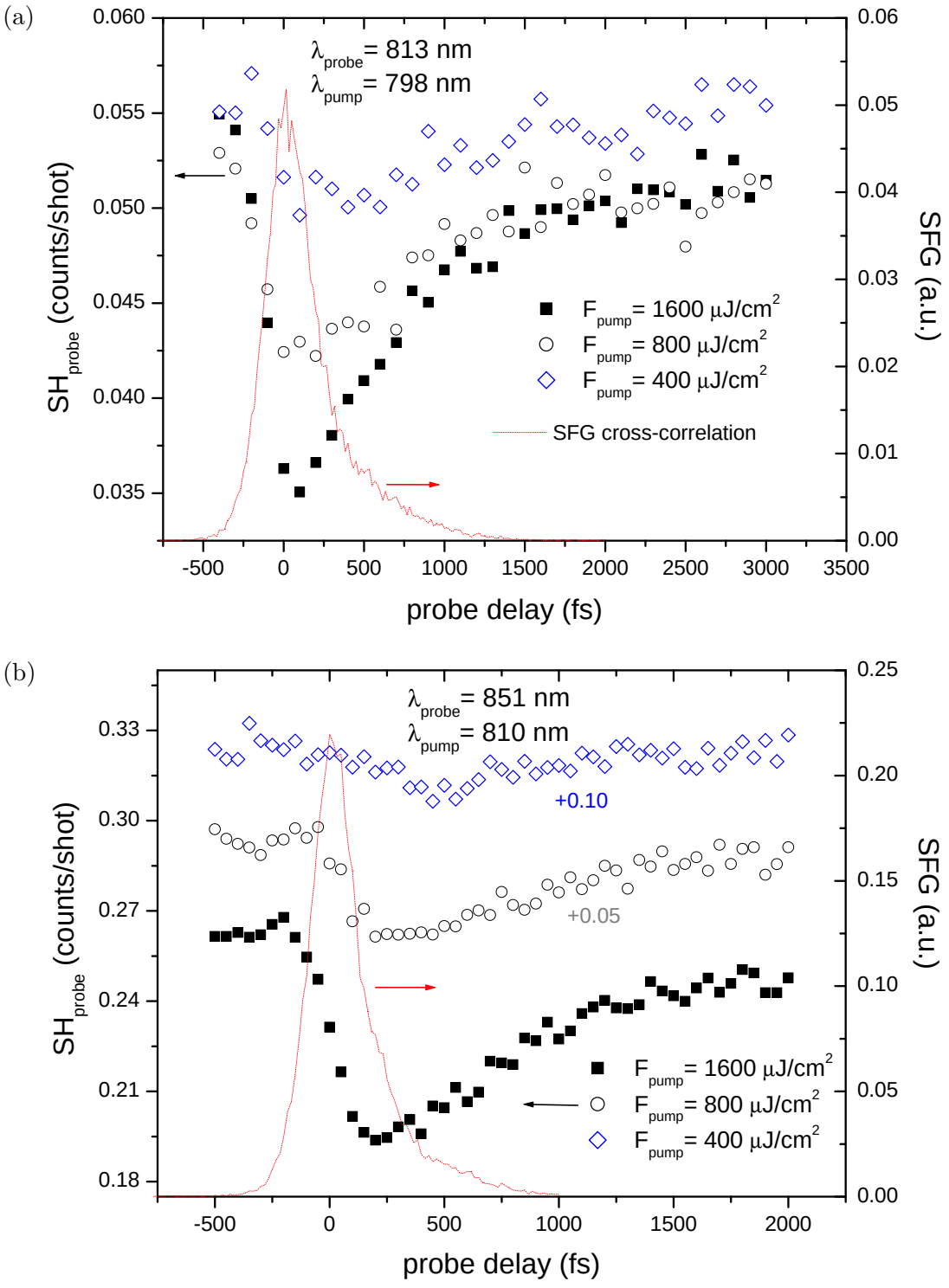

Figure 2.13: Pump-SH_{probe} scans for a pair of positive detunings for several pump fluences. Figure (a) is for a detuning of -29 meV (-231 cm^{-1}), and Figure (b) is for a detuning of -72 meV (-581 cm^{-1}). The solid curve is the SFG cross-correlation. The data for the pump fluences of 800 $\mu J/cm^2$ and 400 $\mu J/cm^2$ in Figure (b) are offset by 0.05 and 0.10 for clarity.

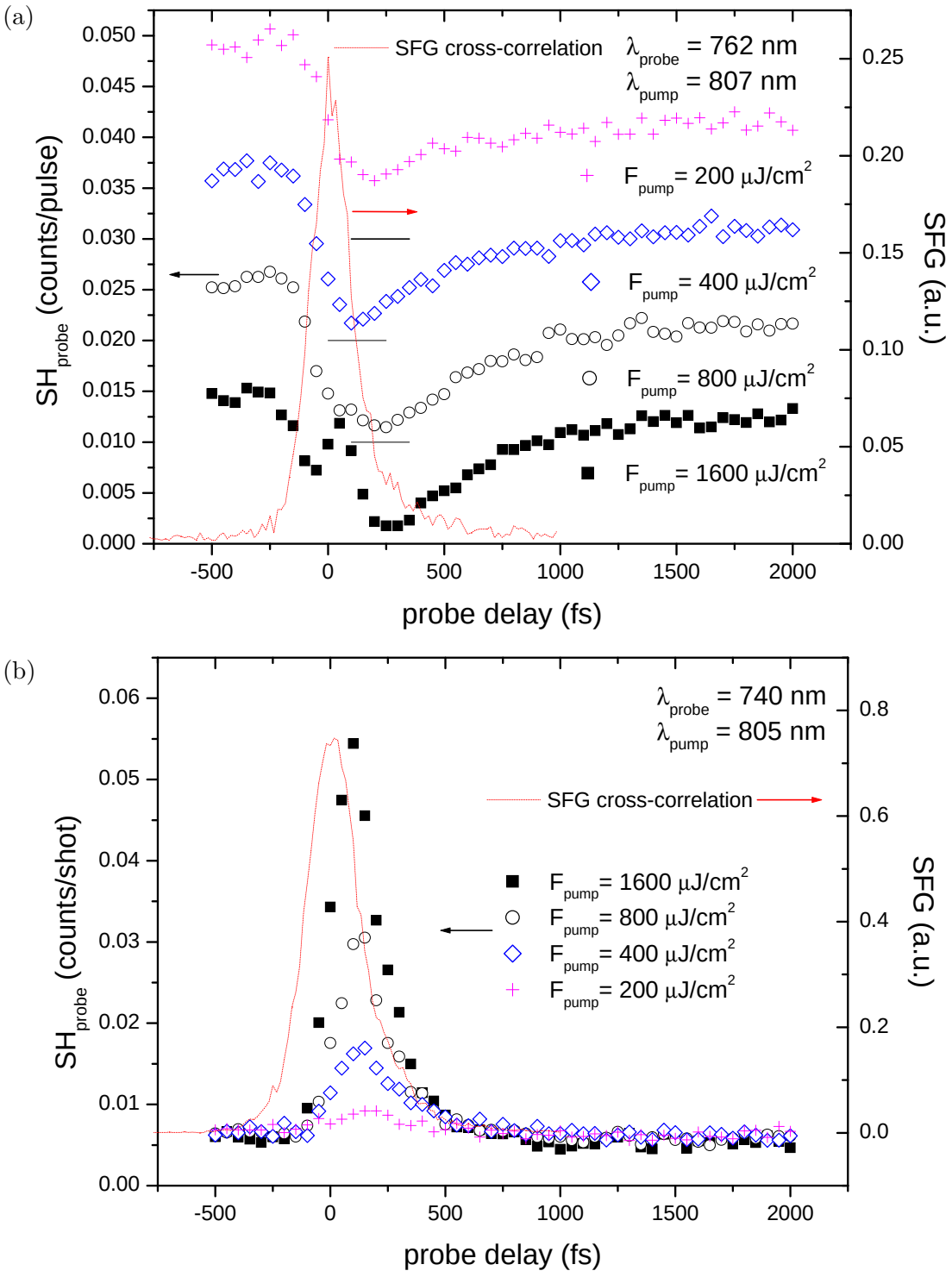

Figure 2.14: Pump-SH_{probe} scans for a pair of positive detunings for several pump fluences. Figure (a) is for a detuning of 93 meV (751 cm^{-1}), and Figure (b) is for a detuning of 136 meV (1096 cm^{-1}). The solid curve is the SFG cross-correlation. The short horizontal lines indicate the offset of the zero signal level for the probe at 762 nm.

other detunings. Such an increase is not necessarily inconsistent with the pump-induced dip observed at other detunings. Recalling Eq. (2.68), which states that the probe SHG signal is given by

$$\begin{aligned} S(2\omega_{pr}, \omega_{pu}, T) &\propto |\alpha_{1\gamma}[1 - \Delta n_{ba}(\omega_{pr} - \omega_{pu}, T)] + \alpha_{2\gamma}|^2 \\ &\propto \left| [1 - \Delta n_{ba}(\omega_{pr} - \omega_{pu}, T)] + \left|\frac{\alpha_{2\gamma}}{\alpha_{1\gamma}}\right| e^{i\phi_{2\gamma}} \right|^2, \end{aligned}$$

we see that, depending on the values of $|\alpha_{1\gamma}|$; $|\alpha_{2\gamma}|$; $\phi_{2\gamma}$, the relative phase between $\alpha_{2\gamma}$ and $\alpha_{1\gamma}$; and $\Delta n_{ba}(\omega_{pr} - \omega_{pu}, T)$, one may observe a pump-induced rise in the probe SH. For example, if $|\alpha_{2\gamma}/\alpha_{1\gamma}| > 1$ and $\phi_{2\gamma} = \pi$, then any $\Delta n_{ba} > 0$ yields a probe SH signal increase. Alternatively, if $1/2 < |\alpha_{2\gamma}/\alpha_{1\gamma}| < 1$ and $\phi_{2\gamma} = \pi$, then $\Delta n_{ba} > 2\,(1 - |\alpha_{2\gamma}/\alpha_{1\gamma}|)$ also yields a probe SH signal increase. In the former case, the relaxation of the system towards equilibrium results in a monotonic decrease of the probe SH signal back to its original level before the arrival of the pump pulse. In the latter case, the relaxation of the system is not monotonic but rather first falls towards zero as Δn_{ba} approaches $2\,(1 - |\alpha_{2\gamma}/\alpha_{1\gamma}|)$ and then rises back towards the level prior to the arrival of the pump pulse. In principle, such a situation could account for the local increase in the probe SH signal observed at a probe delay of about 50 fs in the data corresponding to a pump fluence of 1600 μJ/cm^2 in Figure 2.14a. However, a more careful look at the population dynamics shows that the explanation is not this simple.

The recovery of the signal data yields information on the population dynamics of the system. Excluding for the moment the data shown in Figure 2.14b and the data for a pump fluence of 1600 μJ/cm^2 in Figure 2.13a, in all cases in which the data was not too noisy (including the data from the many pump-probe scans not shown here), the initial (partial) recovery of the probe SH could be fit with a single exponential. The time constants for the initial population dynamics were found to be 700 ± 150 fs for negative detunings and 450 ± 75 fs for positive detunings at pump fluences of 800 and 1600 μJ/cm^2, at which the signal-to-noise ratios were highest. In contrast, as seen in Figure 2.14b, the recovery of the pump-induced increase at a probe fundamental wavelength of 740 nm occurs on a timescale of about 150 fs essentially determined by the temporal resolution of our measurements. If the rise in probe SH signal seen in Figure 2.14a were due to the possibilities raised in the

preceding paragraph, then the recovery times would be expected to be the same for both the pump-induced decreases and increases of Figures 2.13 and 2.14. Therefore, the data suggest that in the frequency range explored there are at least two transitions that are pumped.

The dangling bonds appear to play a crucial role in the transition responsible for the pump-induced increase in the data of Figure 2.14b, as passivation of the surface with hydrogen results in a far less dramatic pump-induced increase of the probe SHG at the largest positive probe detuning (Figure 2.15). We note that the photon energies at which this feature first becomes apparent as a distinct peak ($\hbar\omega_{pump} = 1.54$ eV and $\hbar\omega_{probe} = 1.63$ eV in Figure 2.14a) and at which it becomes dominant ($\hbar\omega_{pump} = 1.54$ eV and $\hbar\omega_{probe} = 1.68$ eV Figure 2.14b) are such that the sum $\hbar\omega_{pump} + 2\hbar\omega_{probe}$ is 4.80 eV in the former case and 4.90 eV in the latter. These energies are to be compared to the work function measured from a clean Si(111)7×7 surface of 4.85 eV [78, 115]. This suggests that the initial state for the transitions involved may be the adatom dangling bond states just below the Fermi level. However, the exact nature of this second pumped transition is otherwise unclear. Despite the presence of this unanticipated transition, this transition appears to be significant only at the largest positive detunings. Therefore, in discussing our hole-burning data later, we will focus our attention on the data for negative and small positive detunings, where the simple model described in Section 2.3 is still expected to hold.

A study of the population dynamics was not the focus of this study, but besides indicating that our assumption of a single pumped transition is no longer valid at our largest positive detuning, their measurement highlights a few important points. The data demonstrate that we are able to probe the system on timescales short compared to the population dynamics. On longer timescales, the perturbations responsible for the population dynamics could obscure the fastest timescale dynamics, i.e., spectral diffusion due to simple population dynamics could obscure the dephasing dynamics. Were we to study spectral hole burning on longer timescales, then some interactions that contribute to population dynamics would shift from being intermediate or slow contributions to the perturbation of the system to being fast perturbations and would then obscure the faster dynamics. To measure the fastest dynamics via spectral hole burning, we need to look at the spectral hole formed at the

earliest times. Moreover, the data for the population dynamics illustrate the importance of using femtosecond pulses to obtain a high signal-to-noise ratio in such a study; femtosecond pulses of a given fluence create a greater modulation of the probe SHG by the pump than picosecond pulses that would necessarily average over the recovery time of the signal. As discussed in Chapter 1, for a case such as this, where the dephasing times of the system are shorter than the 100 fs pulses used, the SHG signal level obtained with the same pulse energy and spot size would be markedly lower with picosecond pulses than with 100 fs pulses.

That the pump-induced changes in the probe SH are due to pump-induced changes in the surface states rather than rapid, pump-induced changes in the bulk dielectric constant or SHG signals originating in the bulk response (e.g., from higher multipole contributions to SHG) can be seen from ancillary measurements. Except at large positive detunings, probe SHG measurements from the hydrogen-passivated surface displayed only very small changes within the first couple of picoseconds after the arrival of the pump, as can be seen in Figure 2.15. Moreover, as will be shown in Section 2.5.2, the probe SHG signals from the passivated surface were much smaller than those from the clean surface, so any relative changes in signal that appear in the data of Figure 2.15 would produce much smaller relative changes in the signal from the clean surface. The results of pump-probe SHG scans at other wavelengths displayed the same features as the data for the wavelengths shown in Figure 2.15, namely negligible change within the first few hundred femtoseconds after the arrival of the pulse at all but the shortest wavelengths. At the shortest wavelengths (largest positive detunings), there was a pump-induced increase of up to about 20% at the highest pump fluences. A possible explanation for this effect at short wavelengths will be discussed below, but for most of the range of wavelengths explored, this effect is not observed. In addition to the pump-probe SHG measurements on the passivated surface, measurements of the reflected probe fundamental did not show any pump-induced change in the probe reflectivity above the signal-to-noise ratio of the measurements. An example of such a pump-probe reflectivity scan is shown in Figure 2.16. These results are consistent with what one would expect from the weak absorption by Si in the wavelength region

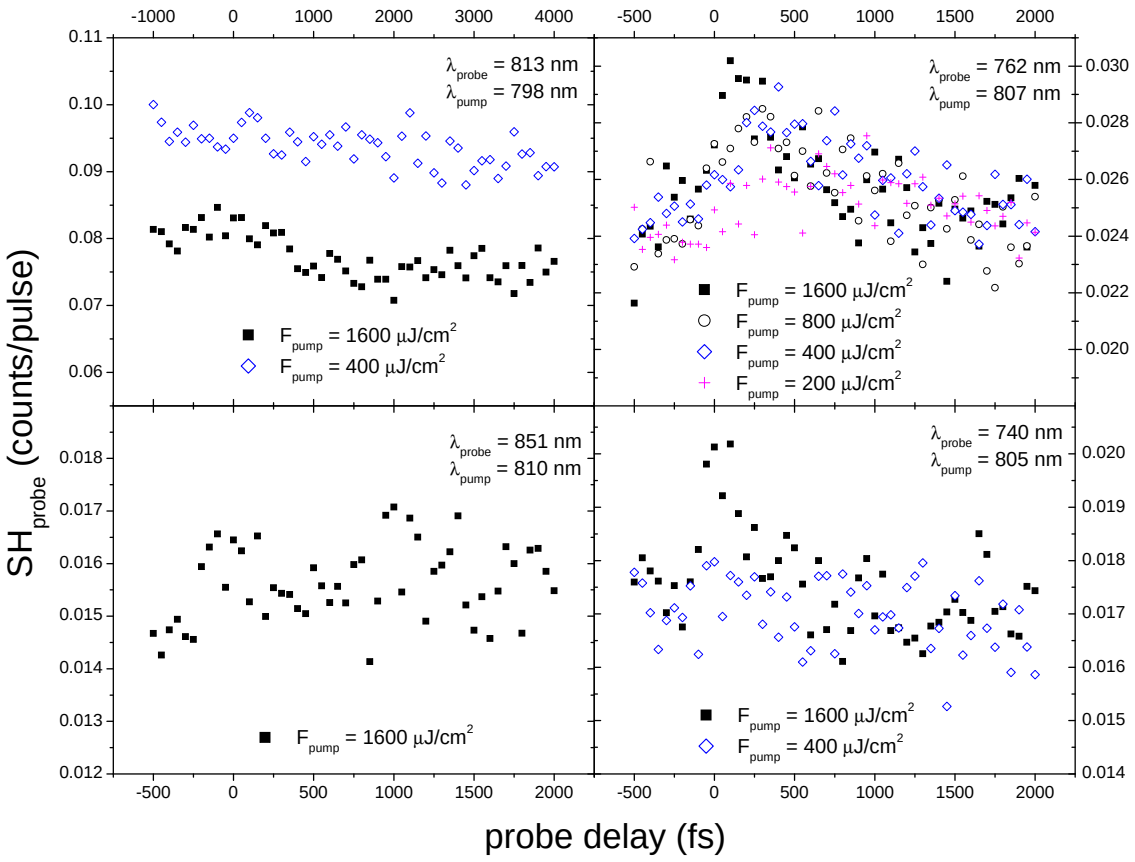

Figure 2.15: Pump-SH_{probe} scans from the passivated Si(111)7×7 surface for the same pump and probe wavelengths as in Figures 2.13 and 2.14.

investigated, where the absorption coefficient at room temperature ranges from 780 cm^{-1} at 1.5 eV to 1800 cm^{-1} at 1.7 eV [116].

2.5.2 Relative Phase Measurements of One- and Two-Photon-Resonance Contributions to SHG

From Eq. (2.68) we see that, to determine the quantity $\Delta n_{ba}(\omega_{pr} - \omega_{pu}, T)$ from the hole-burning data, it is necessary to know the relative magnitudes and phases of the terms $\alpha_{1\gamma}$, attributed to transitions between the S_2 and U_1 bands of Figure 2.2, and $\alpha_{2\gamma}$, attributed to a two-photon resonance between the S_3 and U_2 bands. These relative phases and magnitudes can be determined by means of passivating the Si(111)7×7 surface with atomic hydrogen. A variety of studies have shown that H initially reacts with the Si(111)7×7 adatom dangling

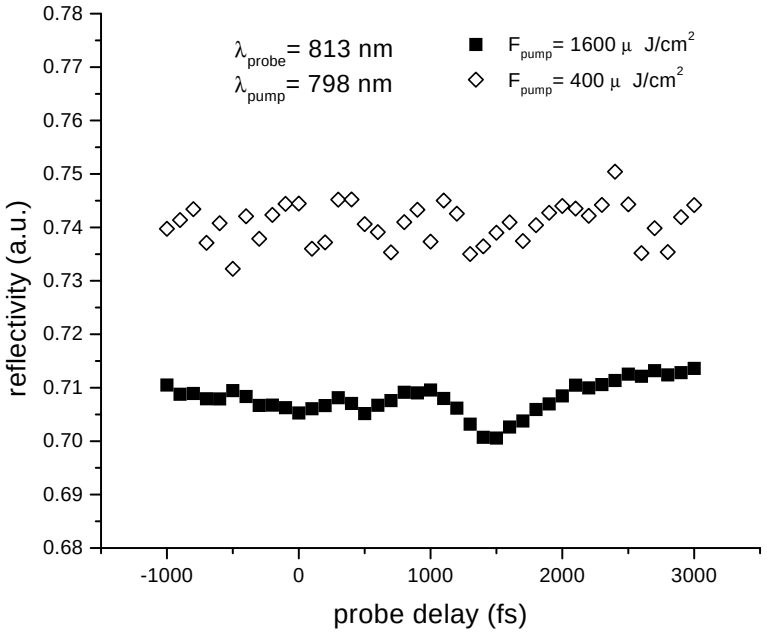

Figure 2.16: Reflected probe energy measured with an InGaAs photodiode as a function of delay relative to the pump for pump fluences of 400 μJ/cm^2 and 1600 μJ/cm^2.

bonds [46, 87]. Only as the adatom dangling bonds become saturated does H start to react with the adatom back bonds, eventually leading to a bulk 1×1 termination of the rest atom layer with preservation of the stacking fault and, hence, the 7×7 unit cell [46]. Therefore, it is expected that as the surface is passivated by exposure to hydrogen, $\alpha_{1\gamma}$ will gradually disappear, while $\alpha_{2\gamma}$ will remain unchanged. This is clearly suggested by Figure 2.3, which shows that under H adsorption the SHG spectral peak below a fundamental photon energy of 1.6 eV disappears, while the SHG spectral peak at about 1.7 eV remains unchanged. We assume that $\alpha_{1\gamma} = 0$ when the adatom dangling bonds are fully passivated and that H adsorption does not change $\phi_{2\gamma}$. In the absence of a pump, the probe SH signal from the unpassivated surface is given by Eq. (2.68) as

$$S(2\omega_{pr}, \theta = 0) = k\,|\alpha_{2\gamma}|^2 \left| \left| \frac{\alpha_{1\gamma}(\theta = 0)}{\alpha_{2\gamma}} \right| + e^{i\phi_{2\gamma}} \right|^2, \tag{2.71}$$

where θ is the surface coverage, k is a constant of proportionality, and $\phi_{2\gamma}$ is the relative phase between $\alpha_{2\gamma}$ and $\alpha_{1\gamma}$. For cases in which $\phi_{2\gamma} > \pi/2$ and $|\alpha_{2\gamma}\cos\phi_{2\gamma}| < |\alpha_{1\gamma}|$, as $\alpha_{1\gamma}$ is gradually eliminated by H adsorption there will be a minimum in the probe SH signal at

$\theta = \theta_{S_{pr,min}}$:

$$S(2\omega_{pr}, \theta = \theta_{S_{pr,min}}) = k\ |\alpha_{2\gamma}|^2 \left| \left| \frac{\alpha_{1\gamma}\left(\theta_{S_{pr,min}}\right)}{\alpha_{2\gamma}} \right| + e^{i\phi_{2\gamma}} \right|^2 = k\ |\alpha_{2\gamma}|^2\ \sin^2\phi_{2\gamma}. \quad (2.72)$$

Once the dangling bonds are completely passivated (at a coverage of $\theta_{term} \sim 0.4$), the nonlinear response should derive solely from the back bond response:

$$S\left(2\omega_{pr}, \theta_{term}\right) = k\ |\alpha_{2\gamma}|^2\,. \quad (2.73)$$

Therefore, the phase of the back-bond contribution to the nonlinear response relative to the dangling-bond contribution is given by

$$\phi_{2\gamma} = \arcsin\sqrt{\frac{S\left(2\omega_{pr}, \theta_{S_{pr,min}}\right)}{S\left(2\omega_{pr}, \theta_{term}\right)}}\,. \quad (2.74)$$

With the relative phase known, we can determine the relative magnitudes of $\alpha_{1\gamma}$ and $\alpha_{2\gamma}$ by comparing the probe SH from the unpassivated surface to the probe SH from the passivated surface. Combining Eqs. (2.71) and (2.73), we obtain for the ratio of the magnitudes of the dangling-bond and back-bond contributions to $\chi^{(2)}$

$$\left|\frac{\alpha_{1\gamma}}{\alpha_{2\gamma}}\right| = -\cos\phi_{2\gamma} + \sqrt{\cos^2\phi_{2\gamma} - 1 + \frac{S_{pr}(2\omega_{pr}, \theta = 0)}{S_{pr}(2\omega_{pr}, \theta_{term})}}. \quad (2.75)$$

This is illustrated in Figure 2.17, which shows as an example the SHG signal from the Si(111)7×7 surface at a fundamental photon wavelength of 762 nm and a cartoon of the evolution of $\chi^{(2)}(2\omega_{pr}; \omega_{pr})$ with hydrogen coverage. In general, the values of $\phi_{2\gamma}$ and $|\alpha_{1\gamma}/\alpha_{2\gamma}|$ vary with frequency. Figure 2.18 shows the probe SHG signal as a function of hydrogen dosing for the range of probe fundamental wavelengths studied in which there was a minimum in the probe SH at $\theta_{S_{pr,min}} \neq 0$.

Applying Eqs. (2.74) and (2.75) to the data in Figure 2.18 yields the values for $\left|\chi^{(2)}_{db}/\chi^{(2)}_{bb}\right|$ and $\phi_{2\gamma}$ shown in Figure 2.19 ($\chi^{(2)}_{db}$ and $\chi^{(2)}_{bb}$ are the contributions to the second-order susceptibility corresponding respectively to $\alpha_{1\gamma}$ and $\alpha_{2\gamma}$, to which they are proportional). At the shortest probe wavelength investigated there was no longer a minimum in probe SHG observable at nonzero θ, which indicates that either the phase $\phi_{2\gamma}$ was no longer greater than

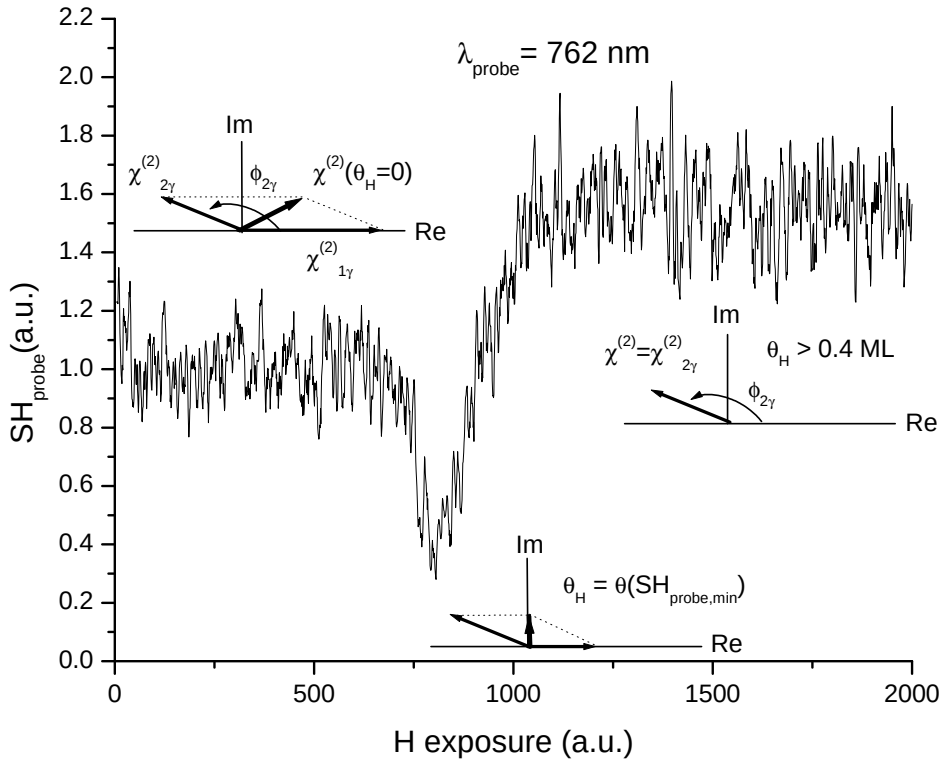

Figure 2.17: Second harmonic of the probe beam as a function of hydrogen exposure at a probe wavelength of 762 nm showing the effect of dosing on the two contributions to $\chi^{(2)}(2\omega_{pr};\omega_{pr})$. The individual contributions $\chi^{(2)}_{1\gamma}$ and $\chi^{(2)}_{2\gamma}$ are equivalent to the quantities $\alpha_{1\gamma}$ and $\alpha_{2\gamma}$ discussed in the text.

$\pi/2$ and/or $|\alpha_{1\gamma}| < |\alpha_{2\gamma}\cos\phi_{2\gamma}|$, so a relative amplitude could no longer be confidently determined by this procedure. Consequently, values for $\lambda_{pr} = 740$ nm are not included in Figure 2.19. Strictly speaking, by this method we can only narrow the value of the phase $\phi_{2\gamma}$ to two possible values ($\pi \pm \delta$, where $\delta > 0$). For our experiments, the choice is unimportant, and in Figure 2.19, we choose $\pi - \delta$. The values of the relative phases and magnitudes between the 1γ and 2γ contributions yield ratios for $\left|\chi^{(2)}(2\omega_{pr};\omega_{pr};\theta=1)/\chi^{(2)}(2\omega_{pr};\omega_{pr};\theta=0)\right|$ that are very close to those of the SHG spectra of Figure 2.3, and the calculated value of $\phi_{2\gamma}$ is consistent with measurements made by others [93, 117].

One point that should be addressed is that the inset in Figure 2.19 shows a difference in the value of $\left|\chi^{(2)}(2\omega_{pr};\omega_{pr};\theta=1)/\chi^{(2)}(2\omega_{pr};\omega_{pr};\theta=0)\right|$ according to whether the pump was blocked during passivation or incident on the sample with the probe pulse *preceding* the pump pulse derived from the same pulse from the Ti:sapphire amplifier. A significant

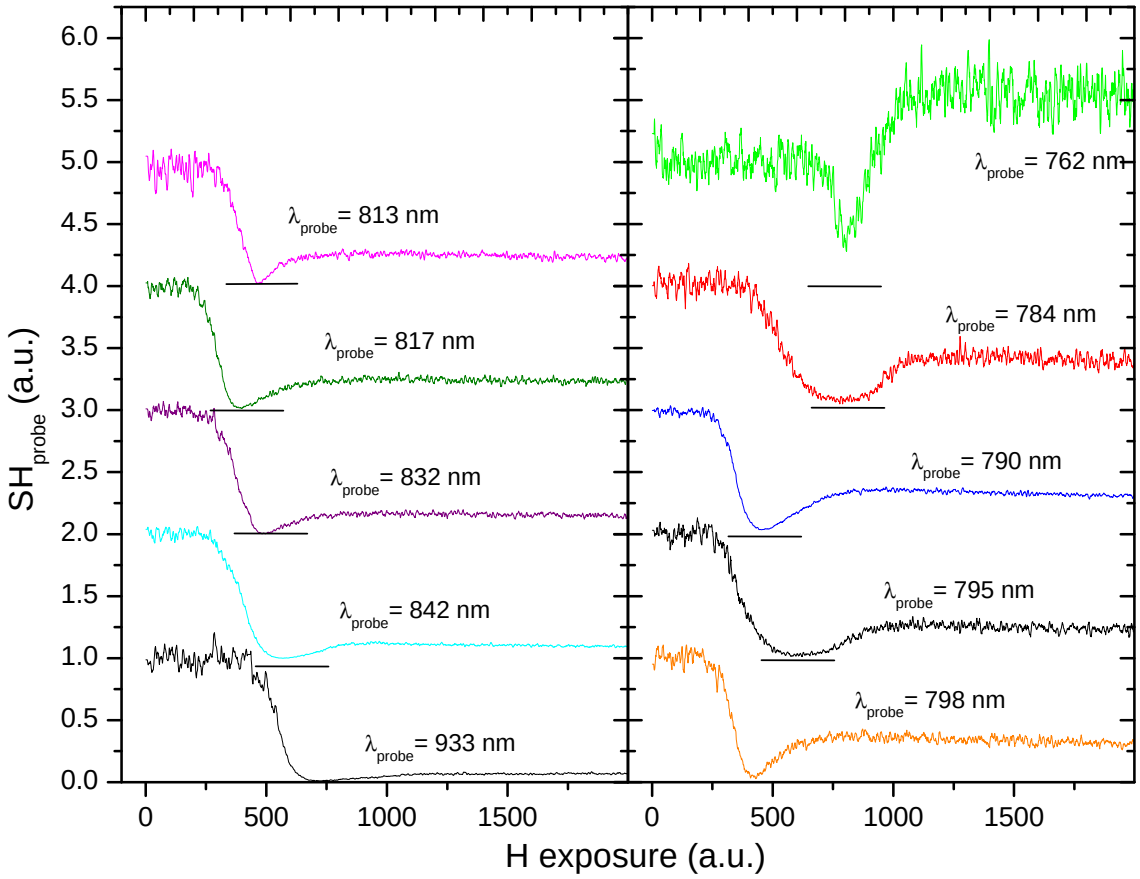

Figure 2.18: Second harmonic of the probe beam as a function of hydrogen exposure at various probe wavelengths. Each curve is normalized to the unterminated signal level and offset by 1.0 relative to the curve below it.

effect of the pump on the phase was not observed, but the effect on the magnitudes was marked. This effect results from changes in the probe SHG signal due to pump-induced changes in the material response caused by preceding laser pulses and persisting on the millisecond timescale between pulses from the Ti:sapphire amplifier. Figure 2.20 shows the effect for clean and passivated surfaces. The effect is not due to sample damage, since blocking the pump always resulted in recovery to the unpumped signal level. Although the signal-to-noise ratio of these measurements is not as high as for the measurements of the relative phases and magnitudes of the 1γ and 2γ contributions to the second-order nonlinear susceptibility, the basic trends are clear. In the case of the passivated surface, there is a pump-induced decrease in the probe SHG that is observed on a millisecond timescale and

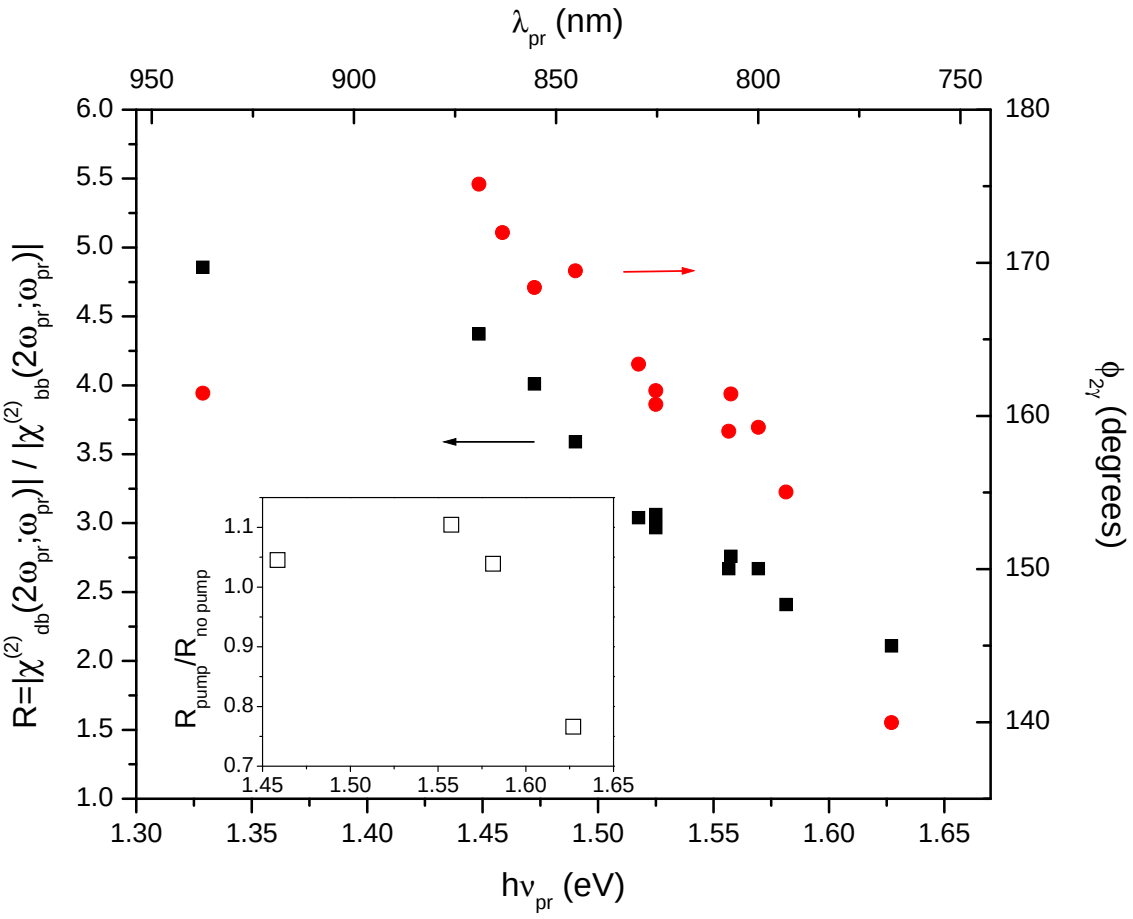

Figure 2.19: Ratio R = $\left|\chi^{(2)}_{db}(2\omega_{pr};\omega_{pr})\right| / \left|\chi^{(2)}_{bb}(2\omega_{pr};\omega_{pr})\right|$ of the amplitudes of the dangling-bond and back-bond contributions to the nonlinear susceptibility of the Si(111)7×7 surface and the relative phase between the two contributions plotted against probe fundamental photon energy. The solid symbols are derived from data for which the pump beam was blocked. The inset shows the ratio $R_{pump}/R_{no\ pump}$, where R_{pump} is the value of R when a pump pulse with a fluence of $F_{pump} = 200\,\mu J/cm^2$ was incident at a delay of 1 ps relative to the probe and $R_{no\ pump}$ is the ratio for $F_{pump} = 0$.

is especially pronounced at the shortest probe wavelengths (largest positive detunings). In the case of the clean surface, the change in the probe SHG is within about ±10%, except at the shortest probe wavelengths. One possible origin of this effect is drift of carriers created in the space-charge region. In particular, the adatom back bonds overlap greatly with the surface-projected bulk band structure, and diffusion of photogenerated charge carriers into the bands formed by the adatom back bonds would be expected to reduce the probe SHG signal due to the two-photon transition between the adatom back-bond bands S_3 and

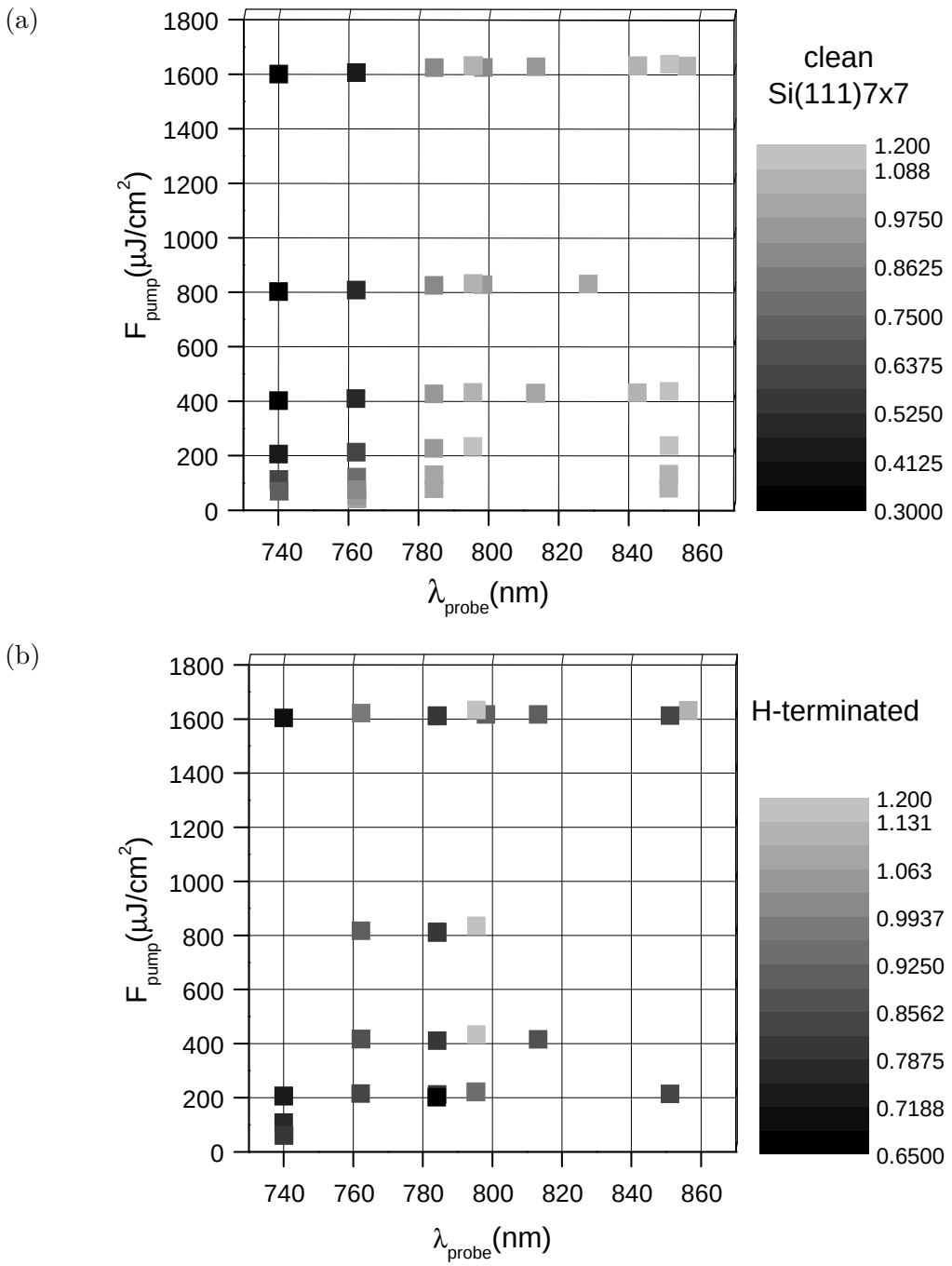

Figure 2.20: Plots of the ratio of the probe SHG signals in the presence and absence of pump pulses incident on the sample for probe pulses arriving 500 fs before the pump pulses ($\frac{\mathrm{SH_{probe}(F_{pump},\tau_{probe}=-500\ fs)}}{\mathrm{SH_{probe}(F_{pump}=0)}}$) as a function of probe wavelength and pump fluence. Figure (a) is data from the clean Si(111)7×7 surface, and Figure (b) is from the hydrogen-passivated surface.

U_2 via phase-space filling (i.e., occupation of the otherwise unoccupied final states for the transition). This process would be slow compared to picosecond timescales and so would not appear in picosecond-scale pump-probe scans. Where the 2γ contribution to the nonlinear response is dominant, i.e., at large positive detunings, particularly as the probe approaches resonance with the two-photon S_3-U_2 transition, and on a hydrogen-terminated sample, one would expect a decrease in the probe SHG even when the probe precedes the pump. Where the 1γ contribution is dominant, i.e., at wavelengths longer than about 760 nm on a clean (unpassivated) Si(111)7×7 surface, one would expect the pump to produce a relatively small increase in the probe SHG signal when the probe precedes the pump because the 2γ contribution, which is almost 180° out of phase with the 1γ contribution will decrease and thereby less effectively cancel the 1γ term. These phenomena qualitatively describe our observations. Photoemission measurements of photovoltage decays due to generation of carriers at the hydrogen-terminated Si(111) surfaces with 20 ns pulses of laser light (λ = 510 nm) by Long *et al.* revealed photogenerated photovoltage changes persisting beyond tens of microseconds even at fluences much less than 1 μJ/cm^2 [118]. The absorption coefficient of Si at a wavelength of 510 nm is about 20 times that at 800 nm, so one would expect that the effects observed by Long *et al.* could be observed using 800 nm radiation at fluences of 20 μJ/cm^2, well above our standard fluences.

2.5.3 Dynamic Electronic Dephasing Times at the Si(111)7×7 Surface

The data for the pump-induced changes in the probe SH signal and the relative magnitudes and phases of the terms $\alpha_{1\gamma}$ and $\alpha_{2\gamma}$ provide the basic elements for a determination from Eq. (2.68) of the function $\Delta n_{ba}(\omega_{pr} - \omega_{pu}, T)$, where T is the delay of the probe relative to the pump. However, given the signal levels seen in Figures 2.13 and 2.14, the time required to determine the entire T-dependent evolution of the pump-probe signal with an adequate signal-to-noise ratio to obtain an accurate measurement of the evolution of $\Delta n_{ba}(\omega_{pr}-\omega_{pu}, T)$ with respect to T would be prohibitive. As already noted at the beginning of Section 2.5, for the measurement of the most rapid dynamics, it is the hole width at the smallest delays T that is of greatest interest to us. To obtain precise values for the spectral

width of the pump-induced change in the probe SH, we performed two-point pump-probe scans in which the pump was scanned back and forth between an arrival time 500 fs after the probe and 200 fs before the probe (times chosen such that the probe pulse arrived well before or immediately after the pump pulse). In this way, there was sufficient time to acquire enough counts that the error due to the statistical nature of photon counting was below the 1% level before the sample could be exposed to 0.3 L of the residual chamber pressure.

The ratio of the probe SHG signal at a probe delay of 200 fs (after the pump) to the probe SHG signal at a probe delay of -500 fs (before the pump) are shown by the filled squares in Figure 2.21. Having determined the relative magnitudes and phases of the one- and two-photon resonances, we are now in a position to determine the dynamic electronic dephasing time. In accordance with our simple model of a single inhomogeneously broadened oscillator producing the 1γ contribution to the second-order nonlinear response, we model the quantity $\Delta n_{ba}(\omega_{pr} - \omega_{pu}, T)$ from Section 2.3 by a single Lorentzian (as in Eq. (2.70)) of the form

$$\Delta n_{ba}(\omega_{pr} - \omega_{pu}, T) = -i\, A_F \frac{1}{\omega_{pr} - \omega_{pu} + i\, 2\Gamma_F}, \tag{2.76}$$

where A_F and Γ_F are fluence-dependent amplitude and damping parameters. This yields the fits given by the open circles in Figure 2.21 and characterized by the parameters given in Table 2.5.3. Although our model fits well the data at negative detunings, there is a significant discrepancy at positive detunings.

To fit both the negative- and positive-detuning data, we must modify our model. The simplest modification is to suppose that the 1γ contribution to the second-order nonlinear response is due to a pair of inhomogeneously broadened oscillators. This is a reasonable possibility given that the Si(111)7×7 surface band structure is not known in sufficient detail to determine whether the surface bands are indeed single bands or separate, narrow, closely spaced bands. To account for such a modification, we can add a second Lorentzian term with a resonant frequency higher than the pump frequency. Leaving the parameters of the first Lorentzian fitting term unchanged and adding a second Lorentzian at $570\,\mathrm{cm}^{-1}$ above the pump frequency and characterized by the fluence-dependent amplitudes and phases given in Table 2.5.3 yields the fit given by the open triangles in Figure 2.21. (Good fits for the

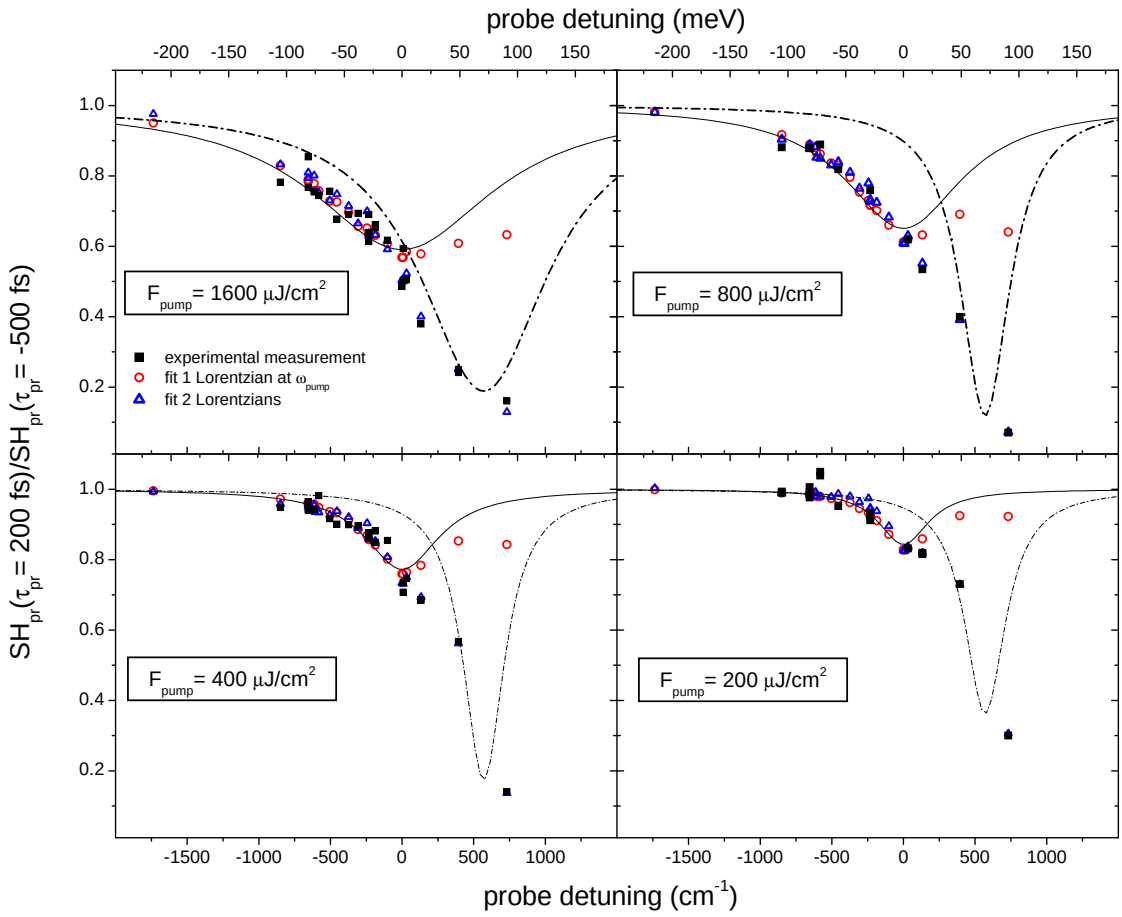

Figure 2.21: The solid squares show the measured values of $\frac{\mathrm{SH}_{\mathrm{probe}}(\tau_{probe}=200\,\mathrm{fs})}{\mathrm{SH}_{\mathrm{probe}}(\tau_{probe}=-500\,\mathrm{fs})}$ as a function of detuning and pump fluence. The open circles are the results of a fit using a single Lorentzian centered at zero detuning. The open triangles are the results of a two-Lorentzian fit in which the same parameters as in the one-Lorentzian fit are used for a Lorentzian centered at the pump frequency, while the second Lorentzian is centered at $570\,\mathrm{cm}^{-1}$ above the pump frequency. For illustrative purposes, the solid and dashed-dotted lines show the absorptive parts of Lorentzian lines with the same linewidths as used in fitting the data.

second hole could be obtained for choices of the second Lorentzian within about ± 40 cm^{-1}.) The Si(111)7×7 reconstruction has a surface optical phonon band at 570 cm^{-1} [119, 120], so the extra term in the fit may be a manifestation of scattering of photoexcited electrons or holes by optical phonons to a third band or to a different point in k-space of the ground or excited band giving rise to the hole at zero detuning. Although the fits involving the second Lorentzian term are fairly good, we must be cautious about the interpretation of

	$-i\,\frac{A_F}{\omega_{pr}-\omega_{pu}+i\,2\Gamma_F}$		$\frac{B_F e^{i\phi_F}}{\omega_{pr}-(\omega_{pu}+2\pi 570\,\mathrm{cm}^{-1})+i\,2\Delta_F}$		
Fluence (μJ/cm^2)	A_F [cm^{-1}]	$\Gamma_F/2\pi$ [cm^{-1}]	B_F [cm^{-1}]	ϕ_F	$\Delta_F/2\pi$ [cm^{-1}]
1600	132 (±11)	387 (44)	200 (54)	-98 (3)	271 (45)
800	73 (7)	251 (31)	101 (10)	-85 (5)	103 (23)
400	30 (2)	158 (14)	90 (6)	-85 (2)	87 (10)
200	14 (3)	107 (23)	61 (5)	-91 (5)	86 (19)

Table 2.3: Parameters for the Lorentzian curves used to model the pump-induced change in the second-order nonlinear susceptibility that are used in fitting the data for the pump-induced hole in Figure 2.21.

the fit. In particular, while both Lorentzian terms contribute significantly to the fit at positive detunings, we cannot readily measure any potential phase difference between two contributions to the 1γ term (i.e., the two transitions giving rise to the separate holes of Figure 2.21) in the second-order response. Moreover, there remain open questions about what is causing the pump-induced change in the probe SH signal from the hydrogen-terminated surface at the largest positive detunings (Figure 2.15) as well as the implications of the millisecond-timescale effect of the pump on the probe SH signal at large positive probe detunings.

Before identifying the linewidths of the Lorentzian fits with homogeneous linewidths of the transition, we must address the possibility of saturation broadening. The SH response of the surface was observed to depend on the square of the fluence of the fundamental ($S(2\omega) \propto U^2(\omega)$) up to the maximum fluences used. However, for short pulses, this is not a sufficient indication of the absence of saturation, since only the portion of the SH signal from the later portions of a pulse are expected to see the full saturation induced by the early portions of the same pulse. An estimate from the case of cw spectral hole burning suggests that saturation can be neglected in relation to the errors indicated in Table 2.5.3. First, we note that in a cw measurement of hole burning in an absorptive feature, the observed linewidth (HWHM) $\tilde{\Gamma}$ is related to the true homogeneous linewidth (HWHM) Γ_2 by $\tilde{\Gamma} = \Gamma_2\left[1+\left(1+\frac{I}{I_S}\right)^{1/2}\right]$, where I_S is the saturation intensity, and the depth of the differential absorption hole at zero detuning is given by $1-1/\left(1+I/I_S\right)^{1/2}$ [4].

Based on the parameters of Table 2.5.3, application of the cw equations for hole burning suggest that our values for Γ_F overestimate the homogeneous linewidth by less than 10% at pump fluences of 1600 and 800 μJ/cm^2 and by less than 5% at pump fluences of 400 and 200 μJ/cm^2. Of course, our measurements are not cw, so application of the cw results for saturation on a two-level system is open to question. For short dephasing times, one can show that the evolution of the population difference $\Delta\rho = \rho_{aa} - \rho_{bb}$ is governed by

$$\frac{d}{dt}\Delta\rho = -\frac{\mathcal{L}\, I}{T_1 I_S}\Delta\rho - \frac{1}{T_1}(\Delta\rho - \Delta\rho_{eq}), \tag{2.77}$$

where $\mathcal{L} = 1/\left(1 + ((\omega - \omega_{ba})T_2)^2\right)$ and T_1 is the population relaxation time [18]. Assuming that at time $t = 0$ the system is in its equilibrium state and that its value in the equilibrium state is $\Delta\rho_{eq} = 1$, the solution to Eq. (2.77) in the case of constant I is [18]

$$\Delta\rho(t,\omega) = \frac{1}{\mathcal{L}I/I_s + 1} + \left(1 - \frac{1}{\mathcal{L}I/I_s + 1}\right) e^{-(\mathcal{L}I/I_s+1)t/T_1}. \tag{2.78}$$

By setting $\omega = \omega_{ba}$, we can use this equation to estimate I/I_S at 200 fs based on the peak of our Lorentzian fit. This value of I/I_s can then be inserted into Eq. (2.78) to determine $\Delta\rho(-200\,\mathrm{fs}, \omega_{pr})$, the width of which can be compared to the width of the unsaturated Lorentzian characterized by the value of Γ_F obtained by the original fits. By means of this approach, we find very similar results as obtained by using the continuous-wave equations for saturation. The values of Γ_F in Table 2.5.3 overestimate the value of $1/T_2$ by 11%, 9%, 6%, and 4% at pump fluences of 1600, 800, 400, and 200 μJ/cm^2, respectively.

The linewidths of the two Lorentzians are plotted against the probe fluence in Figure 2.22. The linear fit for the hole at ω_{pump} is characterized by a slope of $(3.36 \pm 0.27) \times 10^{-5}$ cm$^2\mu$J^{-1}fs^{-1} and intercepts the vertical axis at 0.0144 ± 0.0016 fs^{-1}. The spectral hole centered at ~ 570 cm^{-1} appears to maintain a constant width at the three lower pump fluences and only increases in width at the highest pump fluence. However, the error bars for the hole at ~ 570 cm^{-1} are large enough to accommodate the possibility of a continuous rise in hole width with fluence. In the following, our discussion will focus on the contribution to the spectral hole due to the term that we fit by a Lorentzian at ω_{pump}.

One must initially ask whether the magnitudes of the derived linewidths are reasonable. Transient-grating measurements at the Si(111)7×7 surface with a total fluence of about

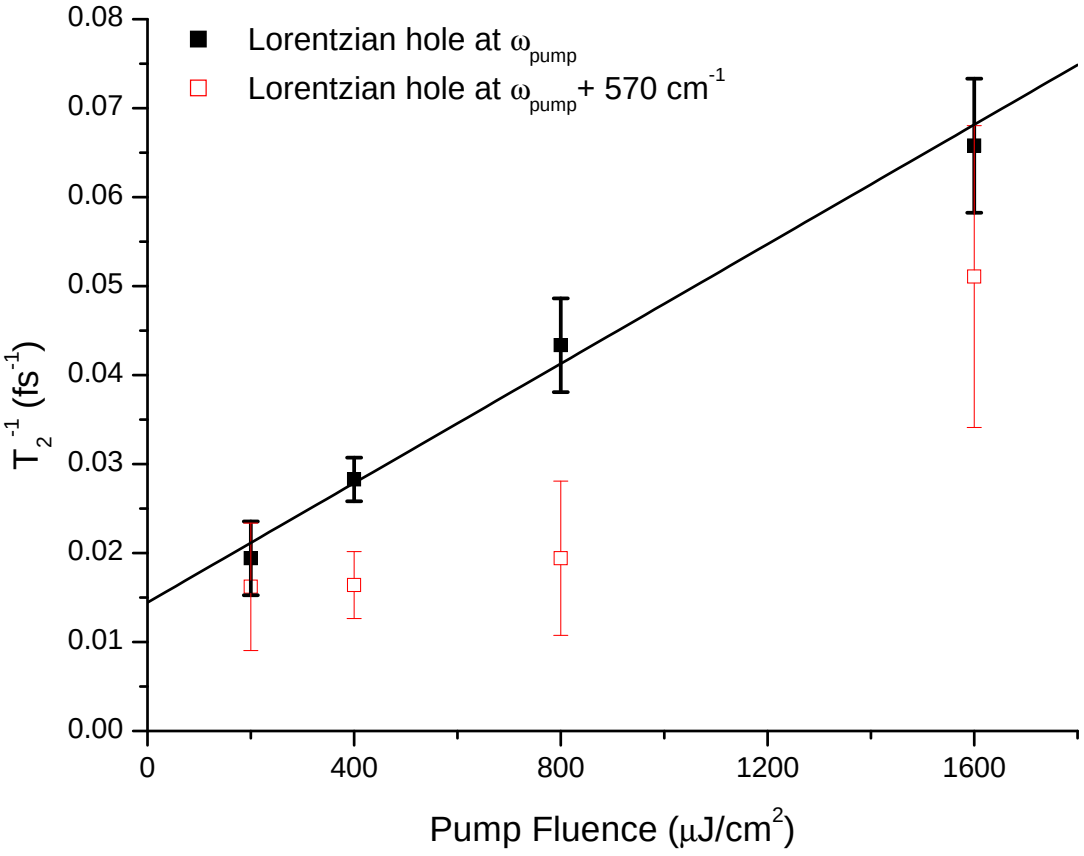

Figure 2.22: Plot of the homogeneous dephasing rates of the two Lorentzians used to fit the data in Figure 2.21 versus pump fluence. The points for the hole centered at ω_{pump} include corrections for the saturation effects discussed in the text. Also shown is a linear fit to the dephasing time corresponding to the hole width of the hole at zero detuning: $1/T_2 \left[\mathrm{fs}^{-1}\right] = 0.0144 + 3.36 \times 10^{-5} F_{pump} \left[\mu\mathrm{J/cm}^2\right]$.

400 μJ/cm^2 suggest the possibility of a dynamic dephasing time of approximately 20 fs [15, 105]. This is in qualitative agreement with our results at a pump fluence of 400 μJ/cm^2, where we obtain a value $T_2 = 34 \pm 3$ fs. The quantitative difference of a factor of less than 2 may be due to various factors. Firstly, it must be noted that the rapid dynamics observed in the transient-grating experiment make quantitative analysis of the transient-grating data strongly dependent on the details of the model used to interpret the data; in fact, both a completely homogeneous model and a primarily inhomogeneous model can account for their data [15, 105]. Secondly, there may be differences between the two sets of experimental results due to differences in the repetition rates of the lasers. The transient-

grating experiment used a repetition rate of about 10 MHz, which is four orders of magnitude greater than the repetition rate used in our hole-burning experiments. In experiments on the Si(100)$c(4\times2)$ surface performed at 76 MHz, Weinelt *et al.* have seen steady-state population of narrow surface states by population transfer from directly excited surface states [103]. The surface states they observed to be populated in a steady-state manner were identified as surface excitons, but surface defects can also be populated in a steady-state manner. Moreover, surface heating effects could be much more significant in the experiments of Voelkmann *et al.* given the orders of magnitude greater cw power per unit area deposited in the illuminated region. In light of the differences in the repetition rates at which the experiments were carried out, a slight difference in deduced dynamic dephasing times would not be surprising. It is worth pointing out that these factors may also account for the observed differences in SHG recovery rates, which yield the population dynamics, between our experiments and those of Voelkmann *et al.* In particular, Voelkmann *et al.* observed SHG recovery times of 200 fs. In contrast to Voelkmann's measurements, pump-probe SHG measurements at a fundamental photon wavelength of 800 nm performed in the same group (that of U. Höfer) by M. Mauerer but using a 1 kHz laser system displayed SHG recovery times of about 500 fs at the lowest pump fluence of 1.75 mJ/cm^2 [15, 105, 117].

The magnitude of the observed dephasing times is also consistent with what one would expect based on measurements of dynamic electronic dephasing at surfaces by time-resolved two-photon photoemission. Measurements of quantum beats from the interference of the $n = 3$ and $n = 4$ image-potential states at the clean Cu(100) surface yielded pure dephasing rates of hundreds of femtoseconds [29, 121]. Linewidth analysis of time-resolved two-photon photoemission spectra of image-potential states at the Cu(111) surface showed low-temperature dephasing rates of about 30 fs for the $n = 1$ state [122]. The order of magnitude difference between these dephasing rates has to do with the reduced penetration into the bulk of the higher-n image-potential states and the fact that the energies of the image-potential states discussed are in the band gap of the surface-projected bulk band structure of the Cu(100) surface but overlap with the surface-projected bulk band structure of the Cu(111) surface. Interferometric time-resolved two-photon photoemission experiments on

the Cu(111) surface found a homogeneous dephasing rate of 20 fs for a transition between an occupied surface state about 0.4 eV below the Fermi level and a surface state located in the bulk band gap [32]. However, approximately 85% of the probability density of the occupied surface-state wave function extends several layers into the bulk [122]. As can be seen from Figure 2.2, the energies of the dangling-bond states giving rise to the S_2 and U_1 bands of the Si(111)7×7 surface are below the bulk valence-band maximum and partly above the bulk conduction-band minimum respectively. Consequently, one might expect dephasing times for the transitions we probe to be similar to the dephasing time observed in photoemission for transitions involving the occupied surface state near the Fermi level of Cu(111). In contrast, one might expect more rapid dephasing of the Si(111)7×7 dangling bonds than of the image-potential states of higher quantum number n at the Cu(100) surface, since the latter states are not only energetically located within the bandgap of the surface-projected bulk band structure but also have a probability density that extends largely into the vacuum.

Another issue that must be addressed is the fluence-dependence of the dynamic dephasing rate. As shown in Figure 2.22 and Table 2.5.3, the deduced dynamic dephasing rate increases linearly with pump fluence. This immediately suggests that the dominant dephasing mechanism at the pump fluences investigated is scattering between charge carriers so that $T_2 \propto N^{-1} \propto F_{pump}^{-1}$, where N is the photoexcited carrier density and F_{pump} is the pump fluence. Carrier-carrier scattering has been investigated extensively in bulk (three-dimensional) systems. Of greater relevance to our studies are the many investigations of carrier-carrier scattering in two-dimensional electron gases created in quantum-well structures [123, 124, 125, 126]. Ultrafast photon-echo measurements in GaAs-GaAlAs quantum-well structures yielded photon-echo decay times from about 16 fs to about 50 fs (corresponding to homogeneous dephasing times of 64 to 200 fs) with echo decay times at low excitation densities showing an inverse-square-root dependence on excitation density ($T_{echo} \propto N^{-1/2}$) [123]. This carrier-density dependence is indicative of strong Coulomb screening of carriers so that carriers effectively interact only with their nearest neighbors [123]. Similarly, ultrafast optical measurements of k-space scattering dynamics in bulk GaAs displayed the equivalent $N^{-1/3}$-dependence of the scattering time expected for

a strongly screened three-dimensional system [124]. The inverse linear dependence on the pump fluence of the deduced homogeneous dephasing time in our case ($T_2 \propto N^{-1}$) indicates that, at the fluences investigated, Coulomb screening does not play a major role in the dynamic electronic dephasing at the Si(111)7×7 surface. This is not surprising given the relatively narrow dispersion of the Si(111)7×7 surface states and the consequently expected low mobility of the surface charge carriers.

Extrapolation of the observed linear dependence of the homogeneous dephasing rate on pump fluence to zero fluence yields an intrinsic homogeneous dephasing time of about 70 fs. The femtosecond timescale of the measured dynamic dephasing immediately excludes a number of dephasing mechanisms. Without even considering the barriers for diffusion out of surface states that may not overlap strongly with the bulk wave functions, diffusion of carriers near the surface into the bulk is found to occur on roughly μs timescales [118]. Measurements of carrier diffusion by transient gratings in the near-surface region of the Si(111) surface yield diffusivities of order 10 cm^2/s [99, 127], so lateral diffusion of the carriers out of the illuminated region is insignificant on the timescales of our experiment. As radiative recombination in bulk semiconductors occurs on timescales of nanoseconds or longer, radiative recombination can presumably be excluded as a source of femtosecond dephasing times at a surface. The centrosymmetry of the bulk Si crystal excludes the possibility of piezoelectric electron-acoustic-phonon interactions [128]. Assuming that the bonds at the Si surface are only weakly polar, the piezo-electric electron-phonon interactions are unlikely to play a major role in dephasing on the femtosecond timescale. Deformation potential electron-acoustic-phonon interactions can occur in Si, but in the bulk such scattering takes place on the picosecond to nanosecond timescales [129, 130, 131]. Extrapolating from the bulk, electron-acoustic-phonon interactions are not expected to contribute significantly to femtosecond electronic dephasing dynamics.

There remain a number of mechanisms that can potentially account for the observed femtosecond zero-fluence dephasing rate. In a time-resolved two-photon photoemission study of carrier dynamics at the Si(100)$c(4\times2)$ surface Weinelt and his collaborators concluded that optical-phonon emission via deformation-potential scattering of electrons excited from the

occupied D'_{up} to the unoccupied D_{down} surface bands (arising respectively from the raised and lowered atoms of the buckled dimers at the surface [132, 133, 134, 135]) occurs on a timescale of about 300 fs [103]. Scattering by optical phonons is an inelastic process that generally plays an important role in population decay. The rates of population recovery in our measurements (See Figures 2.13 and 2.14) might naively suggest that the optical phonon scattering rates may be too slow to account for the wide spectral hole observed at zero detuning. However, the spectral hole observed at 570 cm^{-1} indicates that scattering with the optical phonon band at 570 cm^{-1} is occurring on the sub-200 fs timescale. There are also optical phonon bands at about 240 cm^{-1} [119, 120]. It is possible that optical phonons are contributing significantly to the deduced dephasing times. Interferometric time-resolved two-photon photoemission studies of hole decoherence in the *d* bands at the Cu(100) surface found that Auger recombination produces a hole-hole scattering rate of about 24 fs [136]. Also, defects in the form of submonolayer coverage of a surface with adsorbates strongly increases the dephasing and population decay rates of image-potential states [30]. Likewise, steps were found to have a significant effect on the decay of population in image-potential states on the Cu(119) surface [137]. However, in the case of either type of defect, the density of defects studied was much greater than the density of defects present on our clean surfaces. Carrier-carrier scattering is another likely source of femtosecond dephasing times, especially given the suggestions of metallicity of the Si(111)7×7 surface. The presence of electrons in a partially filled band at the Fermi level provides a source of carriers for scattering even if only a small number of electron-hole pairs are created by photoexcitation. Model calculations of the electronic properties of the Si(111)7×7 ground state indicate that the electrons localized in the adatom dangling bonds form a correlated two-dimensional electron gas with correlation times of about 30 fs, which is of the same order of magnitude as the homogeneous dephasing times that we have measured [77, 84]. However, the exact relevance of such correlation times of electrons in the bands that cross the Fermi level to the electrons occupying the bands involved in the transitions studied here is not immediately obvious.

The preceding suggests that the mechanisms most likely to account for our observed

dynamic dephasing times are carrier-carrier scattering, electron-optical-phonon scattering, and Auger recombination. A definitive resolution of the matter would depend on additional experiments, either second-harmonic hole burning at different frequencies or time-resolved two-photon photoemission measurements. In particular, experiments at low temperatures and at energies such that one probes transitions from occupied band maxima to unoccupied band minima would eliminate dephasing mechanisms such as optical-phonon creation. Further theoretical treatments would also help to shed light on the problem, particularly treatments of the surface states away from the Fermi level.

Further experiments are also suggested by the measurements discussed above. It would be interesting to perform either SHHB or photon-echo measurements at lower frequencies involving excitation of electrons to states in the vicinity of the Fermi level, as these have been the states studied most thoroughly by theorists. Such experiments might help to clarify the nature of the two-dimensional adatom electron gas, particularly with regard to the degree of correlation. However, such experiments are potentially much more challenging than those that we have performed. At the very least, such experiments would either require two independently tunable OPAs in the case of SHHB experiments or the generation of < 10 fs tunable light from an OPA [138]. The most easily interpretable experiments would likely involve excitation of electrons from just below the Fermi level to just above it, but that would necessitate the generation of short pulses of far infrared radiation combined with nonlinear optical techniques.

Beyond studies of the Si(111)7×7 surface, the SHHB technique holds promise for application to other systems. In the most general sense, as an all-optical technique, SHHB is particularly well suited to the study of liquid interfaces and buried interfaces, systems not readily amenable to most other (UHV-based) surface techniques. One particular class of systems that might benefit from a variation of the SHHB technique would be water interfaces. Water interfaces show a broad (of the order of hundreds of wavenumbers) hydrogen-bonded OH stretch vibrational resonance ($\sim 3\,\mu$m) in sum-frequency generation experiments [139, 140]. In bulk water, the OH stretch spectrum has a full-width at half-maximum of greater than 200 cm^{-1}. This is an inhomogeneously broadened feature, but the homogeneous width is

still very broad. Mid-IR photon-echo experiments in the bulk display echoes decaying with a time constant of about 30 fs, which is much shorter than the pulses typically produced at 3 μm [141]. SHHB could be a more suitable technique for studying dephasing of the bonded OH stretch modes at water interfaces.

2.6 Conclusion

In summary, we have used second-harmonic generation as a probe of hole burning to measure dynamic electronic dephasing at the Si(111)7×7 surface. Transitions into an unoccupied adatom-dangling-bond band display homogeneous dephasing times of the order of tens of femtoseconds and varying inversely with the excitation density. Extrapolation of the dephasing rates to zero pump fluence yields an intrinsic homogeneous dephasing time of approximately 70 fs. Likely candidates for such fast dephasing mechanisms include carrier-carrier scattering, scattering of charge carriers with optical phonons, and Auger recombination. The all-optical and surface-specific nature of this technique suggests application to the measurement of homogeneous dephasing at other surfaces displaying ultrafast dynamics.

Chapter 3

Fourier-Transform Sum-Frequency Generation

One challenge posed by using femtosecond pulses for vibrational spectroscopy is the degradation in spectral resolution by their broad bandwidth. One can always resolve spectral features finer than the bandwidth of the excitation source, but this generally requires additional instruments or techniques. The oldest approach, predating the advent of the laser, to resolving spectral features in the optical and infrared regions of the electromagnetic spectrum employs a monochromator, though nowadays one often uses a CCD array in combination with a spectrometer to perform *multichannel* detection. Fourier-transform spectroscopy employing an interferometer is an alternative, and in many respects equivalent, approach. These two approaches are also used in laser spectroscopy, though heterodyne techniques further expand the array of tools for obtaining subbandwidth resolution in laser spectroscopy. The paucity and expense of CCD arrays for detecting IR radiation has limited multichannel detection largely to the visible spectrum. That Fourier-transform spectroscopy can be performed with a single-channel detector has long made Fourier-transform interferometry a powerful technique for performing *multiplex* spectroscopy in the IR. However, applications of Fourier-transform spectroscopy have focused largely on linear spectroscopy.

The use of femtosecond pulses for IR-visible sum-frequency (SF) vibrational spectroscopy poses particular challenges. In this chapter, we consider the case in which the broad band-

width of the IR input overlaps the vibrational resonances of the system, while the visible input and SF output are non-resonant with any material response or only in resonance with electronic features broader than any of the laser linewidths. The primary difficulty is that with temporally short, broadband IR and visible inputs, the SF spectrum does not directly reflect the vibrational spectrum but is a convolution between the visible input spectrum and the vibrational spectrum.

To overcome the problem, one approach is to narrow the visible input bandwidth [37], which necessarily lengthens the visible pulse. A narrow-band pulse establishes a one-to-one correspondence between the vibrational and the SF spectra. Multichannel detection of the SF spectrum can be achieved by passing the SF output through a spectrometer equipped with a CCD array. Such an approach has a number of attractive features including the fact that the full spectrum is obtained in every shot, making the technique very robust against pulse energy fluctuations. However, there are some potential disadvantages, particularly the loss of visible power that occurs in the process of producing a narrow-band visible pulse and the difficulty in eliminating a strong nonresonant background from the SF spectrum. In this chapter we explore the applicability of an alternative approach based on Fourier-transform techniques, namely Fourier-transform SFG, or FT-SFG, to obtaining vibrational spectra with subbandwidth resolution [38].

The application of Fourier-transform spectroscopy (FTS) to nonlinear optics is not a new idea, but here we discuss some important issues that have not been thoroughly addressed for the broad class of nondegenerate nonlinear spectroscopic techniques. Fourier-transform spectroscopic techniques have been adopted in the fields of multidimensional nonlinear spectroscopy (spectroscopy in which spectra are obtained by tuning more than one input frequency) [142, 143, 144, 145, 146]. However, previous implementations left open some questions of relevance to the implementation of FT-SFG. Among the differences between FT-SFG and ordinary multidimensional spectroscopy is the fact that the latter typically involves an output degenerate in frequency with the input and also resonant with the material normal modes. This permits the introduction of heterodyne detection schemes using a split-off portion of the input to serve as the local oscillator [143, 144, 145, 146]. In

contrast, FT-SFG involves an output signal at frequencies not present in the input beams, and the IR excitation of the vibrational mode occurs through a single resonant interaction between the medium and the field. Heterodyne detection schemes are not generally used in surface SFG due to the difficulty of producing a stable reference beam at the sum frequency and signal levels that are often below one signal photon per laser pulse. P.M. Felker and his collaborators demonstrated Fourier-transform nonlinear spectroscopies akin to what we describe here for FT-SFG insofar as the techniques involved a singly resonant excitation of the material response followed by up-conversion to a new frequency [147, 148, 149]. However, their investigations were on bulk systems, and while the effect of temporal variation of the visible upconverting pulse(s) was implicitly accounted for in their theoretical treatments of the detected signal, the physical implications of such temporal dependence on the shape of a spectrum in which multiple resonant modes lie within the bandwidth of the exciting lasers and so are simultaneously excited was not addressed. Moreover, important considerations of signal-to-noise ratios were neglected.

The organization of this chapter is as follows. We begin with a discussion of the basic features of Fourier-transform infrared (FTIR) spectroscopy with particular attention to the effects of finite step sizes and scan lengths on the derived spectra. We then present the basic theory of FT-SFG, where the implications of using a visible pulse to upconvert the infrared material polarization are highlighted. Results of two experimental implementations of this approach are discussed. Finally, we analyze the effect of noise on the spectra that can be obtained by FT-SFG and by the alternate multichannel approach to FT-SFG mentioned above.

3.1 Basics of FTIR

The first Fourier-transform spectroscopic technique developed was linear Fourier-transform infrared (FTIR) spectroscopy. A typical example of FTIR spectroscopy involves determining the spectrum of an IR source by collecting the light in a Michelson interferometer and detecting the output of the interferometer as a function of the optical-path-length difference between the two arms of the interferometer. As the basic issues for all Fourier-transform

spectroscopies are the same, we begin by discussing FTIR to illustrate the fundamentals of FT spectroscopy. We will only treat those issues necessary to yield a basic understanding of FT spectroscopy in general and the limitations of FT-SFG in particular. Details of linear FT spectroscopy can be found in the literature [150, 151, 152, 153, 154].

Consider a field

$$E(t) = \int_{-\infty}^{\infty} \tilde{E}(\nu) e^{-i2\pi\nu t}\, d\nu, \tag{3.1}$$

where we have neglected any spatial dependence or vectorial character of the field. Suppose this field is sent through an interferometer with a time delay τ between the two arms. Assuming a perfect 50:50 beam-splitter, the output field is then

$$E_{out}(t,\tau) = \frac{1}{2}\left[E(t) + E(t+\tau)\right]. \tag{3.2}$$

The output energy per unit area is

$$S(\tau) = \frac{c}{8\pi} \int_{-\infty}^{\infty} \left|E_{out}(t,\tau)\right|^2\, dt. \tag{3.3}$$

With Eqs. (3.1) and (3.2), it follows that

$$S(\tau) = \frac{c}{16\pi} \int_{-\infty}^{\infty} \left|\tilde{E}(\nu)\right|^2 \left[1 + \cos(2\pi\nu\tau)\right]\, d\nu. \tag{3.4}$$

The τ-independent term in the integrand only yields a signal at zero frequency that is not of any spectral interest to us. Fourier transformation of the interferogram $S(\tau)$ yields the spectral density

$$\begin{aligned} \tilde{S}(\nu) &= \int_{-\infty}^{\infty} S(\tau) e^{i2\pi\nu\tau}\, d\tau \\ &= \frac{c}{16\pi}\left\{\left|\tilde{E}(\nu)\right|^2 + \delta(\nu) \int_{-\infty}^{\infty} \left|\vec{E}(\nu')\right|^2\, d\nu'\right\}, \end{aligned} \tag{3.5}$$

where we have used the fact that $\tilde{E}(-\nu) = \tilde{E}^*(\nu)$. The last term describes the signal at zero frequency, $\nu = 0$.

In practice, we use discrete sampling to obtain an interferogram with discrete points, $S(n\,\delta\tau)$, instead of the continuous, infinite interferogram $S(\tau)$, with n being integers extending from $-N/2$ to $N/2-1$ or $\tau = n\,\delta\tau$ from $-T/2$ to $T/2-\delta\tau$, where $T = N\,\delta\tau$. The

spectral density is then given by the estimate:

$$\tilde{S}(\nu) \approx \sum_{n=-N/2}^{N/2-1} S(n\,\delta\tau) e^{i2\pi\nu\, n\,\delta\tau} \delta\tau. \tag{3.6}$$

For discussion of the accuracy of this approximation, we convert the above series back into a Fourier integral

$$\sum_{n=-N/2}^{N/2-1} S(n\,\delta\tau) e^{i2\pi\nu\, n\,\delta\tau} \delta\tau \;=\; \int_{-\infty}^{\infty} \Sigma(\tau, \delta\tau, T) e^{i2\pi\nu\tau}\, d\tau \tag{3.7}$$

by defining

$$\Sigma(\tau, \delta\tau, T) \equiv \text{Ш}\left(\frac{\tau}{\delta\tau}\right) \cdot \Pi\left(\frac{\tau}{T}\right) \cdot S(\tau), \tag{3.8}$$

where

$$\text{Ш}(x) \equiv \sum_{n=-\infty}^{\infty} \delta(x-n) \tag{3.9}$$

accounts for the discreteness of the interferogram and

$$\Pi(x) \equiv \begin{cases} 1 & : \quad -\frac{1}{2} < x < \frac{1}{2} \\ 0 & : \quad \text{otherwise} \end{cases} \tag{3.10}$$

accounts for the finite range of the interferogram. To determine the effect of discrete sampling over a finite range of path differences, it is useful to recall an important property of Fourier transforms, namely,

$$\hat{\mathcal{F}}[f(t) \cdot g(t)] = \hat{\mathcal{F}}[f(t)] * \hat{\mathcal{F}}[g(t)], \tag{3.11}$$

where $\hat{\mathcal{F}}$ indicates a Fourier transform of the function enclosed in brackets, and $*$ indicates a convolution

$$\tilde{f}(\nu) * \tilde{g}(\nu) = \int_{-\infty}^{\infty} \tilde{f}(x) \cdot \tilde{g}(\nu - x)\, dx. \tag{3.12}$$

The Fourier transform of $\Sigma(\tau, \delta\tau, T)$ with respect to τ is then

$$\tilde{\Sigma}(\nu, \delta\tau, T) = \hat{\mathcal{F}}\left[\text{Ш}\left(\frac{\tau}{\delta\tau}\right)\right] * \left[\hat{\mathcal{F}}\left[\Pi\left(\frac{\tau}{T}\right)\right] * \hat{\mathcal{F}}\left[S(\tau)\right]\right]. \tag{3.13}$$

By making use of the rescaling property of the Fourier transform

$$\hat{\mathcal{F}}[f(\tau/T)] = T\ \tilde{f}(\nu\ T), \tag{3.14}$$

we can rewrite the Fourier transform of the interferogram as

$$\tilde{\Sigma}(\nu, \delta\tau, T) = T\ \delta\tau\ \tilde{\text{III}}(\nu\ \delta\tau) * \left[\tilde{\Pi}(\nu\ T) * \tilde{S}(\nu)\right]. \tag{3.15}$$

The Fourier transformed quantities that constitute $\tilde{\Sigma}$ are easily calculated (See Figure 3.1):

$$\tilde{\text{III}}(\nu) = \text{III}(\nu) \tag{3.16}$$

and

$$\tilde{\Pi}(\nu) = \text{sinc}(\nu). \tag{3.17}$$

These finally yield

$$\tilde{\Sigma}(\nu, \delta\tau, T) = T\ \delta\tau\ \text{III}(\nu\ \delta\tau) * \left[\text{sinc}(\nu\ T) * \tilde{S}(\nu)\right]. \tag{3.18}$$

As seen from Eqs. (3.6) and (3.7),

$$\tilde{\Sigma}(\nu, \delta\tau, T) \approx \tilde{S}(\nu). \tag{3.19}$$

Equation (3.18) describes how good the approximation is. From the convolution in the square brackets of Eq. (3.18), we see that the limited range of path differences from $-T/2$ to $+T/2$ limits the resolution of $\tilde{S}(\nu)$ to $\sim 1/T$, the full spectral width at half maximum of the sinc(νT) function (To be precise, the full width at half maximum of sinc(νT) is 1.2/T). The effect of discrete sampling appears in the convolution of the spectrum in square brackets with the function $\tilde{\text{III}}(\nu\ \delta\tau)$, which is a an infinite sum of delta functions with period $1/\delta\tau$. (This is the same as band structures in crystal lattices, where the inverse of the real-space distance between unit cells yields the size of the unit cell in k-space, and vice versa). If the true spectrum contains frequency components ν outside the fundamental range from $-1/2\delta\tau$ to $1/2\delta\tau$, they will be aliased to frequencies $\nu = m/\delta\tau$ inside this frequency range, where m is an integer. Thus, if the spectrum to be probed covers the range $(0, \nu_2)$ (We have $\tilde{S}(\nu) = \tilde{S}(-\nu)$), there is an upper limit of $\delta\tau = 1/2\nu_2$ on the step size of an interferogram that does not alias the spectral range under investigation to lower frequencies. The preceding discussion is illustrated graphically in Figure 3.1, which shows the case of a pair of Lorentzian lines with frequencies of 0.30 and 0.40 and choosing $\delta\tau = 1$, i.e., normal sampling.

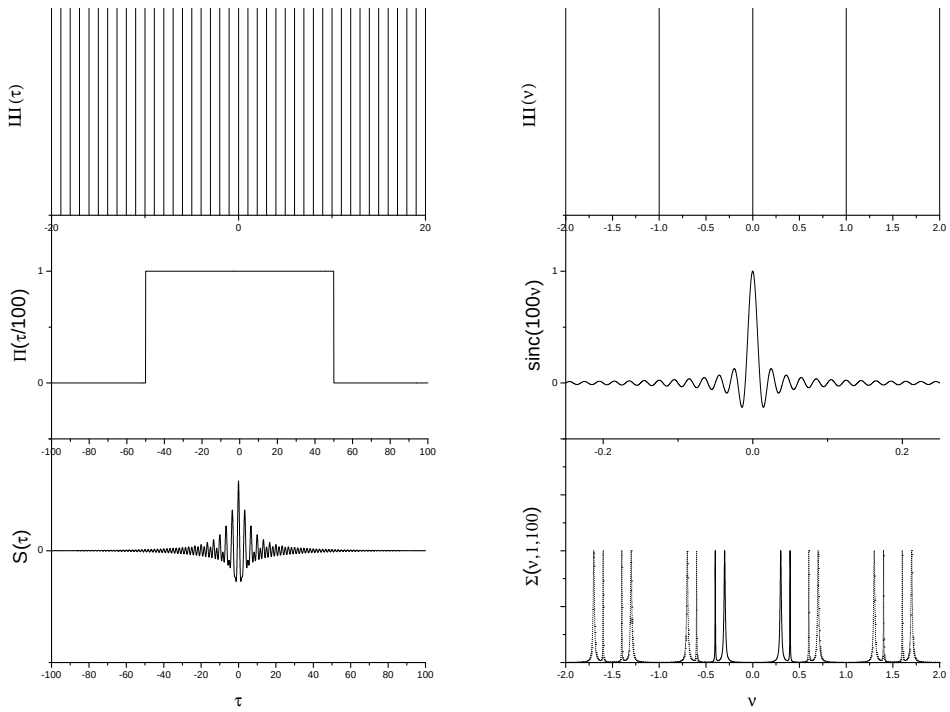

Figure 3.1: The figures on the left show the three functions whose product yield the finite, discrete interferogram of Equation (3.8), with the bottom left figure being the infinite, continuous interferogram resulting from a pair of Lorentzian spectral lines. The figures on the right show the Fourier transforms of the corresponding time-domain functions on the left. In the bottom right figure, the solid curve is the Fourier transform of the infinite interferogram, and both the solid and dotted curves describe the Fourier transform of the finite, discrete interferogram, the latter also showing the periodic aliasing of the spectrum into all periodic spectral ranges $(-0.5+n, +0.5+n)$, where n is an integer. In the figures, the unit of time is set by $\delta\tau = 1$ and the unit of frequency by $1/\delta\tau$. The plots of $\text{Ш}(\tau)$ and $\text{Ш}(\nu)$ should be extended to negative and positive infinity along the abscissa.

If a spectrum is known to be restricted to a range (ν_1, ν_2), one can exploit such aliasing. Instead of regular sampling to obtain an interferogram, one can undersample (i.e., collect an interferogram with step size larger than $1/2\nu_2$) by taking a step size as large as $n/2\nu_2$, where n is the largest integer less than or equal to $\nu_2/(\nu_2 - \nu_1)$. The frequency period (the period of repetition of the spectrum in the frequency domain) is now $2\nu_2/n \approx 2(\nu_2 - \nu_1)$. The spectrum in the frequency range $\left(\frac{n-1}{n}\nu_2, \nu_2\right)$ is then aliased into the fundamental range $\left(0, \frac{1}{n}\nu_2\right)$. Were one to instead undersample by using a step size twice as large as that shown in Figure 3.1, the fundamental frequency range would be reduced to the range -0.25 to 0.25 and the spectral features in the range $(0.25, 0.50)$ ((-0.50,-0.25)) would appear in the

range $(-0.25, 0.00)$ ((0.00,0.25)) through aliasing. Specifically, the features at frequencies of 0.30 and 0.40 would give rise respectively to features at frequencies -0.20 and -0.10 or, equivalently, at frequencies 0.20 and 0.10.

One of the advantages of Fourier-transform spectroscopy, particularly in the form of FTIR, compared to spectroscopy using a monochromator and single-channel detection is the multiplex advantage (also known as the Fellgett advantage) [155, 156]. Since one collects signal in the form of an interferogram from the whole spectrum throughout the entire measurement time and only decodes the interferogram afterward (as opposed to the case of a monochromator with single-channel detection, which only detects a narrow portion of the signal spectrum at any given time and rejects the rest) one expects to obtain a much better signal-to-noise ratio for a given amount of data collection time. To obtain a spectrum over a bandwidth $(\nu_2 - \nu_1)$ with resolution $\delta\nu$, in a time T, it will take $N = (\nu_2 - \nu_1)/\delta\nu$ steps with a time T/N at each step in the monochromator case. Since the multiplex FT approach involves measurement of each $\delta\nu$ interval a factor of N times longer than the sequential monochromator case, the signal-to-noise ratio is expected to be $\sqrt{N}$ times better for the former if the noise is due to sources other than the signal (e.g., background blackbody radiation). For large N, this advantage can be significant.

A second important advantage of Fourier-transform spectroscopy is the Jacquinot, or throughput, advantage [157, 158]. Generally, an interferometer will have a much greater energy gathering efficiency than will a conventional spectrometer. This, of course, yields a further increase in the signal-to-noise ratio.

However, these advantages of FT spectroscopy become less appreciable in dealing with nonlinear optical spectroscopy using ultrashort laser pulses with bandwidth exceeding the width of spectral features of interest. First, the throughput advantage is often lost in the case of coherent laser spectroscopy where the signal output is a collimated beam. Second, the multiplex advantage is diminished because there is only a limited bandwidth to multiplex. For example, consider a 100 fs pulse with a corresponding bandwidth of 150 cm^{-1} FWHM used to obtain a spectrum. If we are interested in a spectral resolution of $5\,\mathrm{cm}^{-1}$, there are only 30 steps or channels to multiplex, resulting in an improvement in signal-to-noise

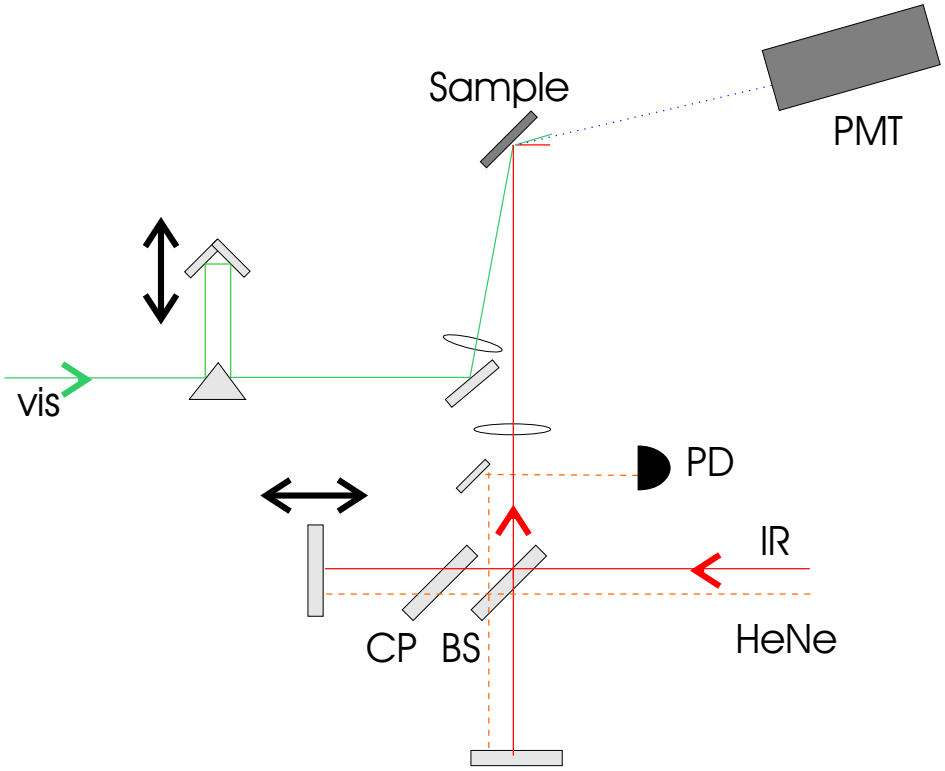

Figure 3.2: Experimental setup for performing FT-SFG measurements. BS=beam splitter, CP=compensation plate, PD=photodiode, and PMT=photomultiplier.

ratio of about a factor of 5 for the FT case. More importantly, as we shall see later, the multiplex advantage of FT spectroscopy is lost in comparison with multichannel detection using a spectrometer.

3.2 FT-SFG: Introduction

The basic concept of FT-SFG as applied to a vibrationally resonant but electronically non-resonant system is illustrated in Figure 3.2, which also illustrates the setup used in our experimental realization of the technique. As in FTIR, the IR field is passed through an interferometer. The IR field performs the same role as in FTIR; its passage through the interferometer and subsequent irradiation of the sample result in a path-length-dependent interference in the material polarization. A compensation plate in one arm of the interferometer ensures that dispersion across the IR bandwidth is the same through both arms of

the interferometer and, hence, that the point of zero delay is the same for all frequencies. The visible beam is directly incident on the sample and couples with the the IR material polarization to produce a sum-frequency signal. As a second-order process, sum-frequency generation is surface-specific if the bulk medium has inversion symmetry. Thus, one way to look at SFG spectroscopy is by noting that the visible pulse, in converting the IR polarization to the visible, essentially serves as a detector for the surface IR polarization, while the PMT that actually detects the sum-frequency photons merely serves as an amplifier. In the implementation of FT spectroscopy, the slow IR detectors used in FTIR detect the IR radiation emitted during the entire lifetime of the coherent material excitations, but in FT-SFG, the visible pulse can be short compared to the dephasing time of the IR material excitation, in which case the visible delay must be scanned to capture the entire decay of the coherent IR response of the system.

3.3 FT-SFG: Mathematical Treatment

The mathematical treatment of FT-SFG follows that of FTIR except that we need to include the additional interaction, or upconversion, step due to the interaction between the medium with the visible field. We assume here the use of a visible pulse described by $E_v(t_v, \tau_v)$, where τ_v is the time delay of the pulse relative to the later one of the two interfering IR pulses reaching the sample. As for equation (3.3), the SF output from the sample is given by

$$S_{SF}(\tau, \tau_v) = \frac{c}{8\pi} \int_{-\infty}^{\infty} |E_{SF}(t, \tau, \tau_v)|^2 \, dt, \tag{3.20}$$

with τ being the time delay between the two IR pulses. In terms of the nonlinear polarization $P_{SF}^{(2)}$ induced in the medium, we can write

$$S_{SF}(\tau, \tau_v) \propto \int_{-\infty}^{\infty} \left| P_{SF}^{(2)}(t, \tau, \tau_v) \right|^2 \, dt, \tag{3.21}$$

where

$$P_{SF}^{(2)}(t, \tau, \tau_v) = \int_{-\infty}^{\infty} dt_v \int_{-\infty}^{\infty} dt_{IR} \, R^{(2)}(t - t_v, t - t_{IR}) E_v(t_v, \tau_v) E_{IR}(t_{IR}, \tau), \tag{3.22}$$

with $E_{IR}(t_{IR},\tau)$ as in equation (3.2). $R^{(2)}(t-t_v,t-t_{IR})$ is the second-order response function of the medium . Note that we are treating $R^{(2)}$ and E as scalar quantities, rather than as a tensor and vector, respectively; this can always be accounted for at the end. Assuming an instantaneous (delta function) response of the medium to the visible field (The visible and SF frequencies are both assumed to be far from any resonances of the material response), the polarization becomes

$$P^{(2)}_{SF}(t,\tau,\tau_v) = E_v(t,\tau_v)\int_{-\infty}^{\infty} dt_{IR}\, R^{(2)}(0,t-t_{IR})E_{IR}(t_{IR},\tau). \tag{3.23}$$

This can be rewritten as

$$P^{(2)}_{SF}(t,\tau,\tau_v) \propto E_v(t,\tau_v)\int_{-\infty}^{\infty} d\nu_{IR}\,\chi^{(2)}(\nu_{IR})\tilde{E}_{IR}(\nu_{IR},\tau)e^{-i2\pi\nu_{IR}t}, \tag{3.24}$$

with

$$\tilde{E}_{IR}(\nu_{IR},\tau) = \tilde{E}_{IR}(\nu)\left(1+e^{-i2\pi\nu_{IR}\tau}\right), \tag{3.25}$$

where $\tilde{E}_{IR}(\nu)$ is the Fourier transform of $E_{IR}(t)$ from the fixed arm of the interferometer and $\chi^{(2)}$ is the SF nonlinear susceptibility. Inserting Eq. (3.24) in Eq. (3.21) yields

$$S_{SF}(\tau,\tau_v) \propto \int_{-\infty}^{\infty} dt\,|E_v(t,\tau_v)|^2\left|\int_{-\infty}^{\infty} d\nu_{IR}\,\chi^{(2)}(\nu_{IR})\tilde{E}_{IR}(\nu_{IR},\tau)e^{-i2\pi\nu_{IR}t}\right|^2. \tag{3.26}$$

In comparison with Eq. (3.3), this equation illustrates how the visible pulse acts as a gate for detecting the material response. If one were to use a cw visible pulse, then one would have, as in Eq. (3.4),

$$S_{SF}(\tau) \propto \int_{-\infty}^{\infty} d\nu_{IR}\left|\chi^{(2)}(\nu_{IR})\tilde{E}_{IR}(\nu_{IR},\tau)\right|^2\left[1+\cos(2\pi\nu_{IR}\tau)\right], \tag{3.27}$$

Fourier transformation of which would yield, as in Eq. (3.5),

$$S_{SF}(\nu) \propto \left|\chi^{(2)}(\nu)\tilde{E}_{IR}(\nu)\right|^2 + \delta(\nu)\int_{-\infty}^{\infty} d\nu'\left|\chi^{(2)}(\nu')\tilde{E}_{IR}(\nu')\right|^2. \tag{3.28}$$

The first term on the right of Eq. (3.28) gives the IR spectrum of $\left|\chi^{(2)}(\nu)\right|^2$ upon normalization by the input IR spectral intensity.

From Eq. (3.26), it follows that a short visible pulse may distort the spectrum. To see this more clearly, we rewrite Eq. (3.26) as

$$S_{SF}(\tau,\tau_v) \propto \int_{-\infty}^{\infty} d\nu_{IR} \int_{-\infty}^{\infty} d\nu'_{IR}\, \chi^{(2)}(\nu_{IR})\tilde{E}_{IR}(\nu_{IR})\chi^{(2)*}(\nu'_{IR})\tilde{E}^*_{IR}(\nu'_{IR}) \tag{3.29}$$
$$\times(1+e^{-i2\pi\nu_{IR}\tau})(1+e^{i2\pi\nu'_{IR}\tau}) \int_{-\infty}^{\infty} dt\,|E_v(t,\tau_v)|^2\, e^{-i2\pi(\nu_{IR}-\nu'_{IR})t}.$$

Fourier transformation of the τ-dependent term in the above equation yields the spectrum

$$\tilde{S}_{SF}(\nu) \propto 2\chi^{(2)}(\nu)\tilde{E}_{IR}(\nu) \int_{-\infty}^{\infty} d\nu_{IR}\chi^{(2)*}(\nu_{IR})\tilde{E}^*_{IR}(\nu_{IR})\tilde{F}(\nu-\nu_{IR}) \tag{3.30}$$
$$+\tilde{F}(\nu) \int_{-\infty}^{\infty} d\nu_{IR}\,\chi^{(2)}(\nu_{IR})\tilde{E}_{IR}(\nu_{IR})\chi^{(2)}(\nu-\nu_{IR})\tilde{E}_{IR}(\nu-\nu_{IR})$$
$$+\delta(\nu) \int_{-\infty}^{\infty} d\nu_{IR} \int_{-\infty}^{\infty} d\nu'_{IR}\chi^{(2)}(\nu_{IR})\tilde{E}_{IR}(\nu_{IR})\chi^{(2)*}(\nu'_{IR})\tilde{E}^*_{IR}(\nu'_{IR})\tilde{F}(\nu_{IR}-\nu'_{IR}),$$

where

$$\tilde{F}(\nu) = \sum_{\tau_v} \int_{-\infty}^{\infty} dt\,|E_v(t,\tau_v)|^2\, e^{-i2\pi\nu t} = \int_{-\infty}^{\infty} d\nu'\tilde{E}_v(\nu')\tilde{E}^*_v(\nu'+\nu)e^{-i2\pi\nu\tau_v}. \tag{3.31}$$

In a more compact form in terms of convolutions of Fourier transforms, Eq. (3.30) becomes

$$\tilde{S}_{SF}(\nu) \propto 2\chi^{(2)}(\nu)\tilde{E}_{IR}(\nu)\cdot\left\{\left[\chi^{(2)*}(\nu)\tilde{E}^*_{IR}(\nu)\right]*\tilde{F}(\nu)\right\} \tag{3.32}$$
$$+\tilde{F}(\nu)\cdot\left\{\left[\chi^{(2)}(\nu)\tilde{E}_{IR}(\nu)\right]*\left[\chi^{(2)}(\nu)\tilde{E}_{IR}(\nu)\right]\right\}$$
$$+\delta(\nu)\int_{-\infty}^{\infty} d\nu_{IR}\chi^{(2)}(\nu_{IR})\tilde{E}_{IR}(\nu_{IR})\cdot\left\{\left[\chi^{(2)}(\nu_{IR})\tilde{E}_{IR}(\nu_{IR})\right]*\tilde{F}(\nu_{IR})\right\}.$$

As $\tilde{F}(\nu)$ only has frequency components around $\nu = 0$ with a bandwidth approximately equal to the inverse of the visible pulsewidth, the second term in Eq. (3.32) only contributes to spectral features near $\nu = 0$. This term plays the same role as the delta-function term in Eq. (3.28) for the case of a cw visible beam. When the spectrum of $\tilde{F}(\nu)$ does not overlap with the IR spectrum of interest, this term can be neglected. The first term in Eq. (3.32) then dominates, and only if $\tilde{F}(\nu) = \delta(\nu)$ do we recover the exact spectrum $\left|\chi^{(2)}(\nu)\tilde{E}_{IR}(\nu)\right|^2$.

We now consider two types of visible pulses used for up-conversion, one being a series of equally spaced short pulses and the other a single square pulse. In the case of a series of

short visible pulses spaced by $\delta\tau_v$ covering a total range of visible time delay from 0 to T_v, we can write

$$F(t) \propto I(t) * \left[\Pi\left(\frac{t}{T_v}\right) \cdot \text{Ш}\left(\frac{t}{\delta\tau_v}\right)\right], \tag{3.33}$$

where $I(t) = |E_v(t, \tau_v = 0)|^2$ and $\Pi(t)$ and $\text{Ш}(t)$ are as defined in Eqs. (3.9) and (3.10). We then have

$$\tilde{F}(\nu) \propto \tilde{I}(\nu) \cdot \left[\text{sinc}(2\nu T_v) * \tilde{\text{Ш}}(\nu\,\delta\tau_v)\right]. \tag{3.34}$$

The term in square brackets indicates that, to minimize the effects of aliasing, we should choose a spacing $\delta\tau_v$ such that $\tilde{I}\left(\frac{1}{\delta\tau_v}\right) \ll \tilde{I}(0)$ or, equivalently, $\frac{1}{\delta\tau_v} \gg \Delta_{HWHM}$, where Δ_{HWHM} is the half-width at half maximum of $\tilde{I}(\nu)$. There is then little spectral content of $\tilde{I}(\nu)$ outside the frequency period $1/\delta\tau_v$. The sinc function limits $\tilde{F}(\nu)$ to roughly a bandwidth of $\frac{1.2}{2T_v}$, and as seen in the first term of Eq. (3.32), the overall effect of $\tilde{F}(\nu)$ is in smearing of the quantity $\left[\chi^{(2)*}(\nu)\tilde{E}^*_{IR}(\nu)\right]$. The final resolution of the spectrum obtained by Fourier transforming the interferogram should be better than $\frac{1.2}{2T_v}$ though, as the convolution with $\tilde{F}(\nu)$ is only on $\left[\chi^{(2)*}(\nu)\tilde{E}^*_{IR}(\nu)\right]$, not on $\left|\chi^{(2)}(\nu)\tilde{E}_{IR}(\nu)\right|^2$.

The case of a single square pulse covering the range $[0, T_v]$ is more straightforward. In this case, $\tilde{F}(\nu) = \text{sinc}(2\nu T_v)$, and its convolution with $\left[\chi^{(2)*}(\nu)\tilde{E}^*_{IR}(\nu)\right]$ degrades the resolution of $\left[\chi^{(2)*}(\nu)\tilde{E}^*_{IR}(\nu)\right]$ to $\sim \frac{1.2}{2T_v}$.

3.4 Experimental Demonstration

For an experimental demonstration of FT-SFG, we used this technique to measure the surface vibrational spectrum of a self-assembled monolayer of *n*-octadecyltrichlorosilane $[CH_3(CH_2)_{17}SiCl_3$ (OTS)] on fused silica [159]. For a surface with $C_{\infty v}$ symmetry, the nonvanishing elements of the second-order susceptibility are $\chi^{(2)}_{zzz}$, $\chi^{(2)}_{xxz} = \chi^{(2)}_{yyz}$, and $\chi^{(2)}_{xzx} = \chi^{(2)}_{zxx} = \chi^{(2)}_{yzy} = \chi^{(2)}_{zyy}$ (From left to right, the indices refer respectively to the indicated projections of the sum-frequency, visible, and IR fields). In the last set of equalities, we have assumed that the dispersion between the visible and sum frequencies, both being non-resonant, is negligible so that their corresponding subindices in $\boldsymbol{\chi}^{(2)}$ can be interchanged.

The basic experimental arrangement is shown in Figure 3.2. We first describe the ex-

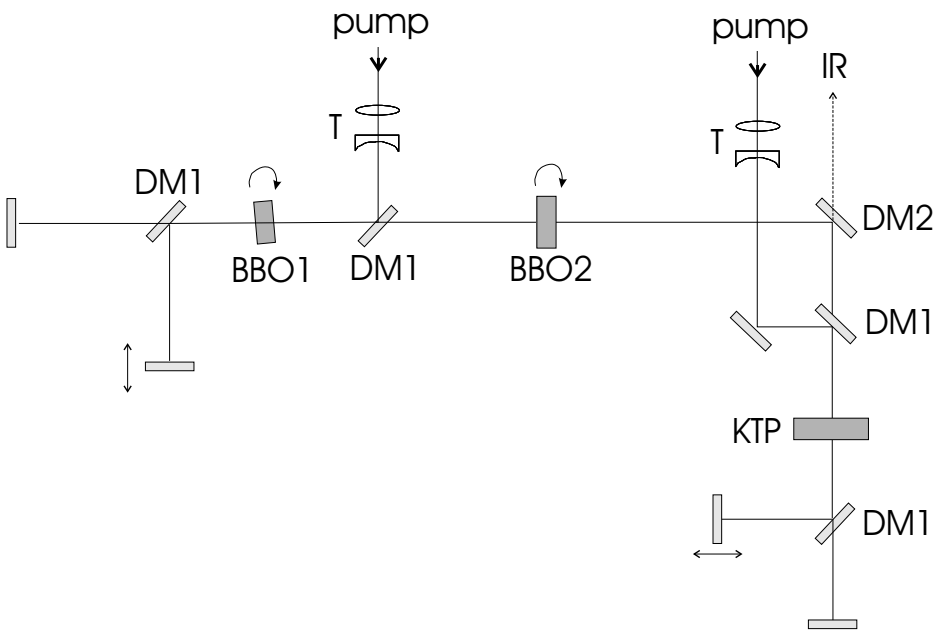

Figure 3.3: OPA used for generating high-energy pulses at around 3 μm in FT-SFG experiments using femtosecond pulses of 800 nm radiation. DM1=dichroic mirror to reflect 800 nm and transmit signal and idler. DM2=dichroic mirror to reflect signal and transmit idler.

perimental arrangement that used 100 fs pulses of 800 nm radiation as our visible beam. To probe CH stretch modes of OTS, IR pulses of $\sim$3 μm radiation were generated by a β-$BaBO_3$-$KTiPO_4$ optical parametric generator/amplifier (Figure 3.3) pumped by the femtosecond Ti:sapphire pulsed laser described in Chapter 1. The first (left) BBO crystal serves as an OPG/OPA. The idler from the first BBO crystal is doubled in the second OPA crystal to provide a seed at the idler frequency for the KTP stage. The final idler pulses were tunable from 2.7 to 3.6 μm and had a spectral width of about 180 cm^{-1} FWHM, a pulse temporal width of 200 fs, and an energy of 20-35 μJ/pulse. The IR beam was sent through a Michelson interferometer and then incident upon the sample at 45° to the surface normal of the sample. 120 μJ of 800 nm radiation was sent through a variable delay line and incident upon the sample at 58°. The two beams spatially overlapped on the sample, with beam spot diameters of approximately 400 and 800 μm, respectively. The SF output in reflection from the sample was passed through spatial and interference filters and detected

by photon counting with a photomultiplier tube. Changes in path length difference between the two arms of the IR interferometer were determined by measuring the interference fringes resulting from the 632.8 nm beam of a He-Ne laser sent through the interferometer parallel to the IR path.

Our later experiments using a stretched visible pulse differed only in a few details. The 100 fs pulses of 800 nm radiation from the Ti:sapphire amplifier that were not used to pump the OPA were sent through a pair of parallel gratings with a groove spacing of 0.9 μm and a separation of about 15 mm perpendicular to the grating faces. At an incident angle of about 81° to the grating face normal, the stretched pulses had intensity profiles of $\sim$ 4.3 ps FWHM. Since the pulses were lengthened merely by chirping, not by spectral narrowing, the energy throughput was limited only by the efficiency of the gratings. The IR pulses for the experiments performed with stretched visible pulses were generated with the KTP-based version of the OPA described in Chapter 1 (These experiments were performed after the experiments with compressed visible pulses at a time when we had already settled on the OPA design of Chapter 1). The angles of the input beams were reversed relative to the case in the experiment with the 100 fs visible pulses, i.e., the IR and 800 nm beams were incident respectively at 58° and 45° and focused to spots of diameter about 100 μm (perpendicular to the direction of propagation of each beam).

The interferometer was a relatively crude, homemade instrument driven only by a delay stage controlled by an optical encoder (Oriel Instruments Model 18236). Most notably, it lacked a continuous feedback system independent of the data acquisition system, and the optically encoded delay stage could not make steps of a magnitude of an optical wavelength without significant error. To address this deficiency, the interferometer was moved in steps that were small compared to the He-Ne fringe spacing (A step size of 100 nm was chosen). In this way we avoided accidentally skipping a HeNe fringe and thereby losing accurate information on the interferometer optical path length difference if the steps were too large. At each interferometer delay at which we measured the He-Ne fringe intensity we also measured the SF signal. After collection of the SF interferogram a new, composite interferogram was created by assigning each point in the measured SF interferogram to the

point corresponding to the nearest peak or trough in the He-Ne interferogram and then obtaining an average SFG signal for that point. When femtosecond visible pulses were used to up-convert and generate the SF interferogram, one such composite interferogram was obtained for each visible pulse delay, and the interferograms from different visible pulse delays were then summed to form the complete interferogram used for Fourier transformation. When stretched picosecond visible pulses were used, the observed SF interferogram could be directly used for Fourier transformation. (We note that for fast Fourier transformation, the data was further padded by adding equal numbers of points on each end of the interferogram with signal strengths equal to the average of the last ten interferogram points at the respective end to bring the total number of points to the 2^n points needed in the fast FT algorithm. This does not alter the resolution, nor should it otherwise affect any spectral features at non-zero frequencies, since a constant contribution to the interferogram only yields a zero-frequency term in the Fourier transform.) In addition to requiring small steps, there are a few other practical drawbacks of our interferometer. Most notably, we did not have the means of establishing the true zero delay with the accuracy needed to perform a single-sided interferometric scan (a scan from $\tau = 0$ to $\tau = T/2$ rather than from $\tau = -T/2$ to $\tau = T/2$), which resulted in a doubling of the needed data acquisition time. Of less fundamental importance was the fact that the very fine steps increased the data acquisition time because of the larger number of analog-to-digital conversions required. The interferogram was grossly oversampled in this case, but as will be seen later, oversampling does not alter the signal-to-noise ratio as long as the data acquisition time and hence the total amount of signal obtained in an interferogram are the same. FT-SFG can readily be implemented with a commercial step-scan FTIR interferometer to circumvent these problems.

To confirm the accuracy of the FT-SFG technique, we compare the spectra obtained by this technique to spectra obtained by sequential sum-frequency spectroscopy with a picosecond laser system. The picosecond laser and OPA system has been described by X. Wei [160]. The narrowband picosecond OPA produces an IR output with a linewidth of $\sim$6 cm^{-1}. The input angles of the narrowband picosecond IR and visible beams were respectively 58° and 45° (i.e., the same as for our stretched-visible FT-SFG measurements

but opposite to the angles for our femtosecond-visible FT-SFG measurements).

To roughly match our FT-SFG resolution to that of the narrowband picosecond OPA, we chose to scan our interferometer over a range of path length differences from -0.75 mm to $+0.75$ mm to yield a corresponding instrument function (the function $\tilde{\Pi}(\nu)$ above) with a full-width at half maximum of $\sim \frac{1}{L} = \frac{1}{0.15\,\mathrm{cm}} = 6.7\,\mathrm{cm}^{-1}$ (To be more precise, for no apodization, the instrument function actually has a FWHM of $\frac{1.2}{L} = \frac{1.2}{0.15\,\mathrm{cm}} = 8.0\,\mathrm{cm}^{-1}$, corresponding to the FWHM of the function $\mathrm{sinc}(\nu L)$). For the visible pulse, rather than using a single stretched visible pulse, we used a sequence of pulses split off from the regenerative amplifier output with different delay times relative to the later of the two IR pulses from the interferometer. Intuitively, our approach to the choice of visible delays was based on the notion that, at each IR path difference, it should be sufficient to capture a good picture of most of the decay of the surface vibrations. This means that we must scan the visible delay both over a sufficiently large range to cover most of the range over which the coherent surface polarization decays and that we must step the visible delay in small enough steps to capture any beating present between different frequencies in the bandwidth of the IR excitation. In practice, we determined the range and size of visible steps by first looking at the SFG free induction decay (FID) from IR excitation of the monolayer to measure the time scale on which the vibrations decohered and the time scale on which any beating between vibrational modes took place. (Note that the beating is a manifestation of the differences in frequencies between discrete spectral features and their decay rates are related to the linewidths of those features, but the homodyne-detected SFG-FID does not reveal the absolute frequencies of the resonant modes.) This approach is justified below in terms of our earlier mathematical analysis of FT-SFG. The SFG FID for ssp and ppp polarizations (As above, from left to right, the indices refer to the SF, visible, and IR polarizations) are shown in Figure 3.4. Based on these FID data, which show quantum beats with half-periods of about 250 fs and almost complete decoherence within 1 ps, and the SFG cross-correlation between visible and IR from an Ag surface (i.e., a material giving an instantaneous response) of about 310 fs FWHM (See Figure 3.4), we chose a series of visible delays of $\tau_v = 0$, 250, 500, 750, and 1000 fs (0, 75, 150, 225, and 300 μm). Assuming the 100 fs FWHM visible

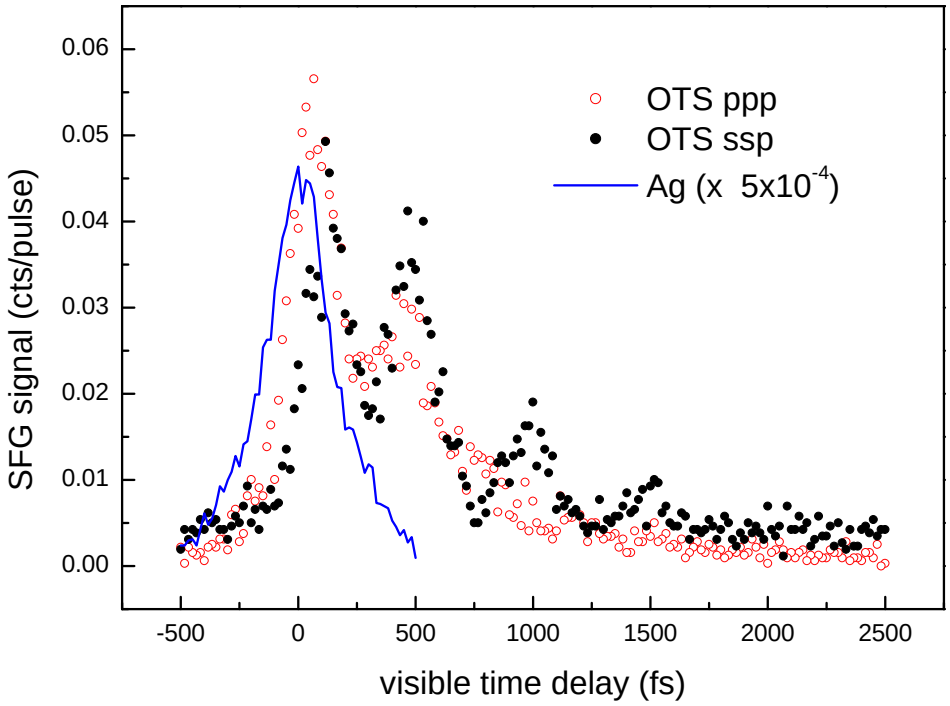

Figure 3.4: SFG measurement of vibrational free-induction decay of OTS on fused silica and SFG cross-correlation measurement from an Ag surface.

pulses to be sech pulses (i.e., pulses with intensity profile $I_v(t) \propto \mathrm{sech}^2(1.763\,t/\tau_{FWHM})$), the bandwidth as given by the FWHM of the spectral density is then about $105\,\mathrm{cm}^{-1}$ (For a Gaussian profile ($I_v(t) \propto e^{-2(1.177\,t/\tau_{FWHM})^2}$) the spectral density would have a FWHM of $150\,\mathrm{cm}^{-1}$). The bracketed portion of the function $\tilde{F}(\nu)$ in Eq. (3.34) then consists of a series of sinc functions of FWHM $\frac{1.2}{2\cdot 0.03\,\mathrm{cm}} = 20\,\mathrm{cm}^{-1}$ (Recall, though, that the effective resolution of the spectrum is finer than this) separated by intervals of $\frac{1}{0.0075\,\mathrm{cm}} = 133\,\mathrm{cm}^{-1}$. The spacing between sinc functions does not quite fulfill the requirement after Eq. (3.34) that one should have $\frac{1}{\delta T_v} \gg \Delta_{HWHM}$, as we have $\frac{1}{\delta T_v} \sim 3\Delta_{HWHM}$. In principle, the spacing between visible pulses should have been somewhat less to eliminate any aliasing from within the bandwidth of the IR, as happens in the curly brackets of Eq. (3.32) due to the extra sinc functions arising from Eq. (3.34). However, as will be seen below, the spectra that we measured contained spectral features only within a roughly $100\,\mathrm{cm}^{-1}$ portion within the bandwidth of the IR, so the aliasing that could occur between features separated by $133\,\mathrm{cm}^{-1}$ did not cause any distortions of our spectra.

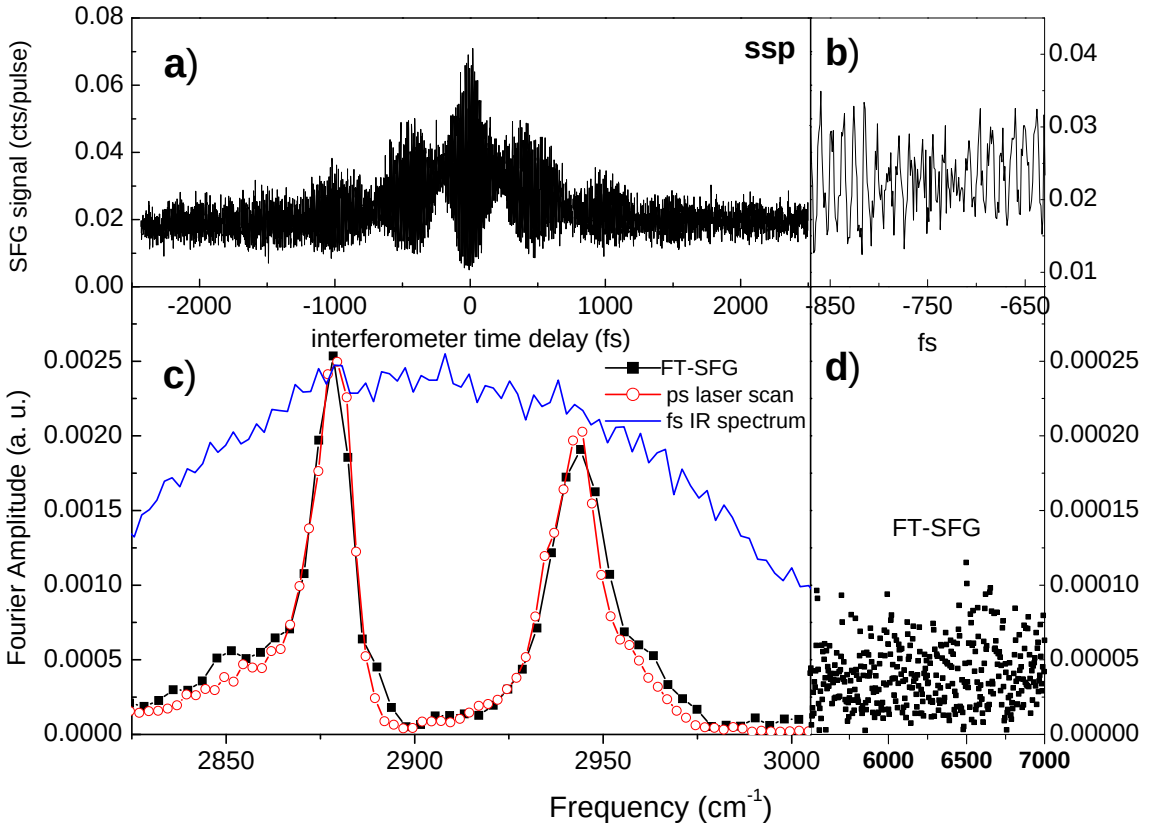

Figure 3.5: (a) Interferogram from OTS on fused silica for SF, visible, and IR polarizations s, s, and p, respectively and (c) spectrum generated by Fourier transformation of the interferogram in (a). Figure (b) shows the interferogram over a short portion of the scan to clearly illustrate the oscillations of the interferogram. Figure (c) also shows the input IR spectrum obtained by detecting the IR through a monochromator. Figure (d) shows the spectrum at frequencies far from the vibrational resonance, which illustrates the noise level of the experiment.

The FT-SFG interferograms and the spectra of the square of the effective susceptibility ($\left|\chi^{(2)}\right|^2$) obtained by Fourier transformation of the interferograms obtained for ssp and ppp polarizations are shown in Figures 3.5 and 3.6, respectively. Figures 3.5a and 3.6a show the SFG interferograms of an OTS monolayer adsorbed on fused silica measured with an IR pulse centered at 2900 cm^{-1} with a FWHM of $\sim$ 170 cm^{-1}. Fourier transformation of the interferogram yields the SFG vibrational spectrum of the OTS monolayer (solid squares) presented in Figures 3.5c and 3.6c. For comparison, we also display the SFG spectrum of the same OTS sample obtained by the traditional sequential scheme with narrowband picosecond input pulses (open circles).

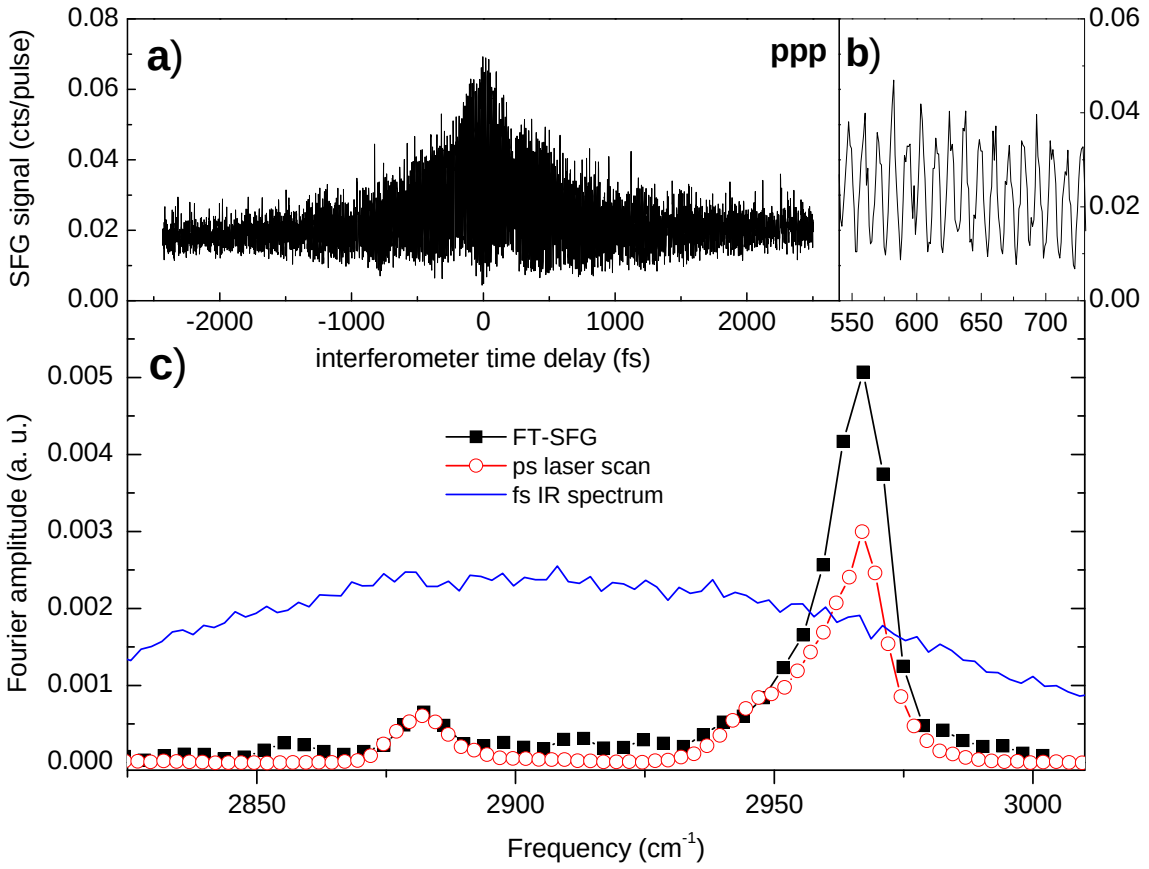

Figure 3.6: (a) ppp SFG interferogram from OTS on fused silica and (c) spectrum generated by Fourier transformation of the interferogram in (a). Figure (b) shows the interferogram over a limited range. Figure (c) also shows the input IR spectrum measured with a monochromator.

The spectra in Figures 3.5c and 3.6c are obtained directly from the data divided by the SFG signal from quartz at the same frequency in the picosecond case and divided by the IR intensity measured directly with a pyrometer (Scientech P09) and a monochromator at the corresponding frequency in the case of FT-SFG. The strong peaks at 2879 and 2944 cm^{-1} in the ssp spectra are due respectively to the CH_3 symmetric stretch and Fermi resonance [161]. The ppp spectrum displays a small peak from the CH_3 symmetric stretch and a large peak at 2967 cm^{-1} due to the antisymmetric CH_3 stretch [161]. Our measured resonant frequencies differ slightly from an earlier assignment [161], but we believe ours are more accurate, since Fourier-transform spectroscopies generally provide absolute frequency calibration. The picosecond spectra shown in Figures 3.5c and 3.6c are shifted 3 cm^{-1} to

lower frequencies to match the frequencies from Fourier transformation. (The reliability of our frequency assignment is demonstrated by the results of a measurement of Fourier-transform coherent anti-Stokes Raman scattering in acetone, in which the IR- and Raman-active mode reported at 2925 cm^{-1} [162] was measured on our instrument to be centered at 2923.4 cm^{-1}, corresponding to a difference well below the 8 cm^{-1} resolution of the interferometric measurement.) The feature at 2850 cm^{-1} in the ssp FT-SFG spectrum may be due to the CH_2 asymmetric stretch [38], but this must be regarded as a questionable assignment given the signal-to-noise ratio.

The agreement between the FT-SFG and narrowband picosecond spectra is excellent in the case of the ssp spectra. This confirms that FT-SFG yields reliable spectra, even when implemented with a sparse, finite set of visible pulse delays. The discrepancies observed in the ppp spectra can be attributed to the differences in beam angles between the picosecond and FT-SFG measurements. In the case of ssp measurements, there is only a single independent non-zero element ($\chi^{(2)}_{xxz}$) that contributes to the signal, so differences in beam angles only affect the magnitude of the signal but not the relative magnitudes of the different spectral components contributing to the signal. In contrast, all three independent matrix elements contribute to the signal in the ppp configuration. In this case, differences in the input angles affect not only the absolute magnitude of the signal but also the relative magnitudes of the different spectral components, since different spectral components will arise from different normal modes that may have different symmetries or orientations.

Although the spectra obtained by the FT-SFG approach display good accuracy and resolution, the FT-SFG spectra took a very long time to acquire. Each interferogram shown in Figures 3.5 and 3.6 required 15,000 seconds of data collection at the laser repetition rate of 1 kHz (We collected 200 shots of data at each combination of visible and IR path delay). If one can accurately and reproducibly start an interferogram at the zero path-delay-difference position, then one can take a single-sided interferogram and reduce the data collection time to 7,500 seconds (For demonstration of the technique with our crude interferometer, we had to use double-sided interferograms to minimize any distortions due to zero-path-delay errors). This is to be compared to the one order of magnitude less time required to obtain

the equivalent spectra with the ps laser system (Each spectrum obtained with the ps system required about 1,200 seconds of data collection time at the ps laser repetition rate of 20 Hz). Although a comparison between such different laser systems may seem misleading, as will be seen later, the data collection time needed for FT-SFG can compare even less favorably to that commonly required in multichannel spectroscopy using a CCD array to detect the SFG from a 100 fs IR pulse and a spectrally narrowed pulse of 800 nm radiation from an equivalent kHz Ti:sapphire laser system. The long time required to obtain the FT-SFG spectra arise from two factors. First, the 800 nm beam could not be focused very tightly on the sample without generating a white-light continuum that overwhelmed the SFG signal. Secondly, there are inherent signal-to-noise issues that can require longer acquisition times than multichannel approaches with equal signal levels. Before analyzing the signal-to-noise issues in detail, we will discuss experiments implementing FT-SFG with a stretched pulse of 800 nm radiation.

Using a long visible pulse to upconvert the IR polarization at the sample surface is attractive for two reasons. Firstly, because surface vibrational polarizations can easily radiate coherently for times T_2' of the order of 1 ps (See Figure 3.4), a picosecond pulse with the same peak intensity as a 100 fs pulse will yield a SFG signal about $\frac{T_2'}{2 \cdot 100\,\mathrm{fs}}$ times the SFG signal obtained with the 100 fs pulse. [‡] On the fused silica substrates, we found that continuum generation occurred at about the same peak intensity for picosecond visible pulses as for 100 fs visible pulses, so the $\sim$ 1 ps dephasing time of the OTS resonances probed should give rise to $\sim$ 5 times as much SFG signal with picosecond visible pulses of the same peak intensity as the 100 fs visible pulses. Secondly, the use of picosecond visible pulses decreases the complexity of the experiment and the data acquisition time since it is unnecessary to use multiple visible pulse delays.

[‡]Assume a homogeneously broadened resonance described by a Lorentzian line characterized by a homogeneous dephasing time T_2. Excitation by a pulse of IR radiation much shorter than T_2 creates a polarization $P_{IR}(t) \propto \sin\theta_{IR}\ e^{-t/T_2}$, where $\theta_{IR} = \frac{\mu_{10}}{\hbar}\int \mathcal{E}_{IR}(t)dt$ is the Bloch vector tipping angle [18]. The SFG signal is given by the interaction between this polarization and the visible field: $S_{SF} \propto \int_{-\infty}^{\infty} dt\ |P_{IR}(t)E_v(t)|^2$. If we assume for convenience a square pulse of visible radiation from $t = 0$ to $t = \tau_v$, we find $S_{SF} = A\left(1 - e^{-2\tau_v/T_2}\right)$, where A is a just a constant of proportionality. In the alternate limits $\tau_v \ll T_2$ and $\tau_v \gg T_2$, we find that S_{SF} is approximately $2\,A\,\tau_v/T_2$ and A, respectively.

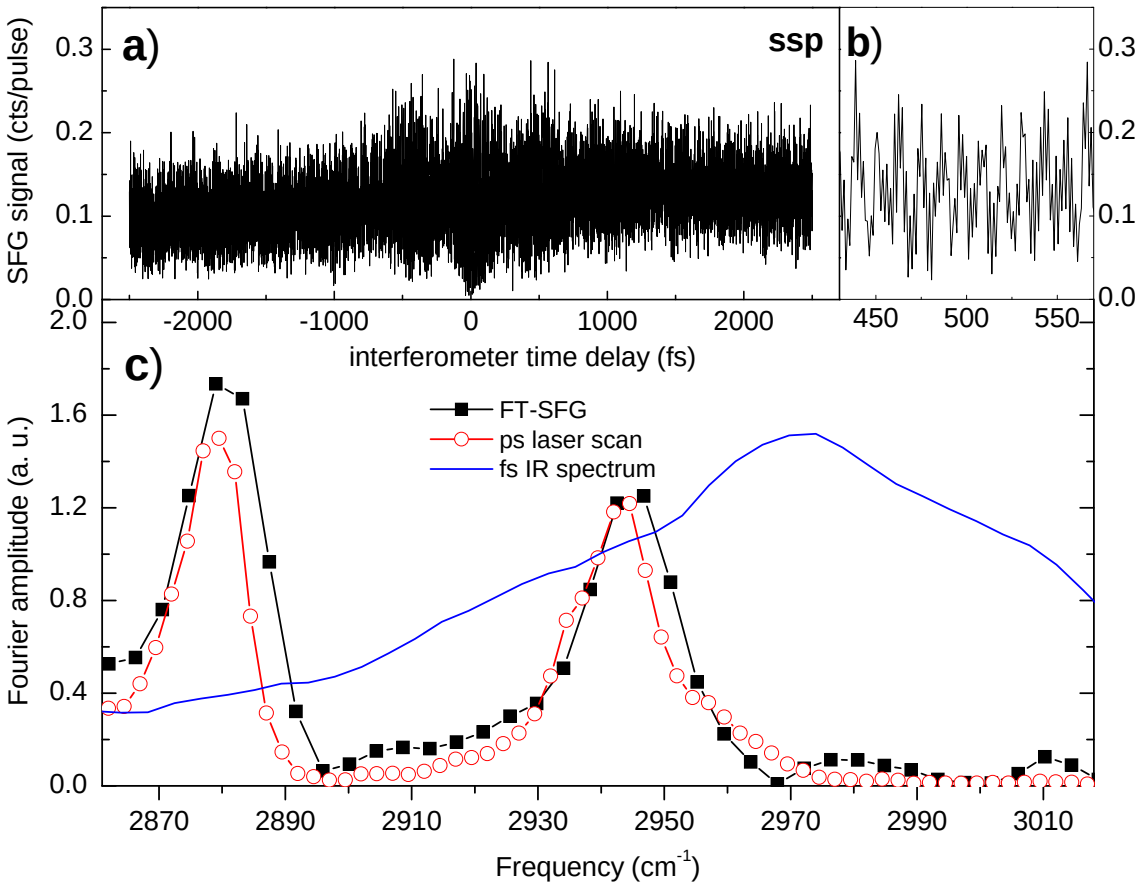

Figure 3.7: (a) ssp SFG interferogram from OTS on fused silica and (c) spectrum generated by Fourier transformation of the interferogram in (a). Figure (b) is a short range from Figure (a). Figure (c) also shows the IR spectrum obtained by Fourier transformation of an FT-SFG interferogram obtained from a bulk crystalline quartz sample in reflection.

Figures 3.7 and 3.8 show the interferograms and spectra obtained from OTS on fused silica by FT-SFG with a stretched visible pulse. The spectra of the infrared input were obtained directly from FT-SFG scans on a crystalline quartz sample, for which there is only a nonresonant response at the frequencies used in this experiment. Collecting 200 shots of data at each IR path delay resulted in collection of approximately the same total number of photons as in the FT-SFG implementation using 100 fs visible pulses described above. The use of ~ 4.3 ps visible pulses results in a FWHM of about 9.3 cm^{-1} for the term $\tilde{F}(\nu)$ of Eq. (3.34).

Figures 3.7 and 3.8 show FT-SFG spectra very similar to those obtained with narrow-

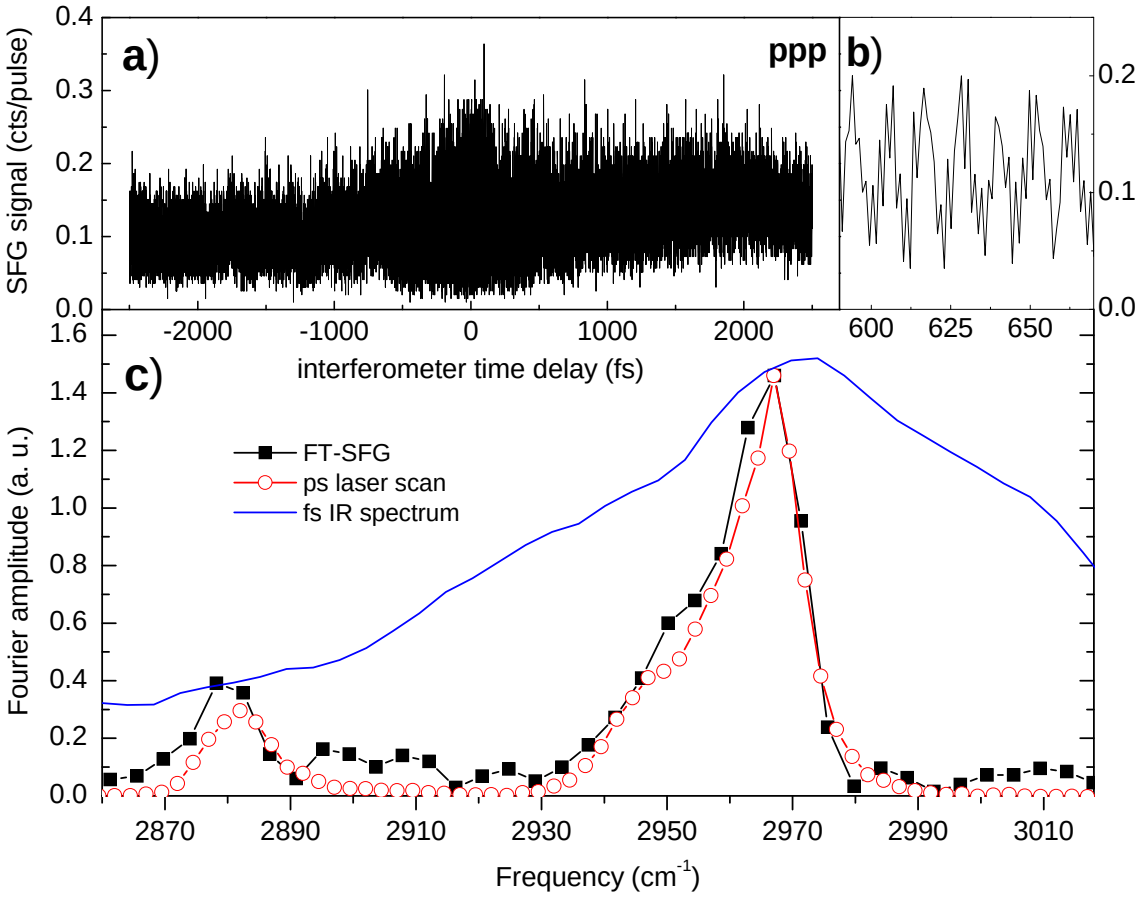

Figure 3.8: (a) ppp interferogram from OTS on fused silica and (c) spectrum generated by Fourier transformation of the interferogram in (a). Figure (b) is a short range from Figure (a). Figure (c) also shows the IR spectrum obtained by Fourier transformation of an FT-SFG interferogram obtained from a bulk crystalline quartz sample in reflection.

band picosecond SFG. As in the implementation of FT-SFG with femtosecond pulses, the main peaks in the ssp spectrum show the same relative peak heights and shapes as in the narrowband picosecond spectrum. Moreover, since the input angles are now the same for the FT-SFG and picosecond spectra, the main peaks in the ppp FT-SFG spectrum also match those of the picosecond spectrum. Compared to the picosecond spectra, there are some discrepancies in the heights of the lower frequency peaks for the FT-SFG spectra of Figures 3.7 and 3.8. These are attributable to two factors that diminish the signal-to-noise ratio at the lower frequencies. Firstly, the IR spectrum was centered at about 2975 cm^{-1}, so that the IR spectral intensity at $\sim$ 2880 cm^{-1} was only about 25% of the peak spectral

intensity. The signal-to-noise ratio of the IR spectrum was about 20:1 at the peak of the spectral intensity, which results in a SNR of about 5:1 at 2880 cm^{-1}. Secondly, the increased signal evident in the interferograms using stretched visible pulses compared to those using 100 fs visible pulses does not result in as much of an improvement in SNR as one would naively expect. In the case of 100 fs visible pulses, when the IR pulses do not overlap the SFG signal is due to up-conversion of the polarization induced by the later of the two IR pulses and that portion of the polarization induced by the earlier IR pulse that has not decayed away. In contrast, in the case of the stretched visible pulse, even when the two IR beams are separated enough that there is essentially no interference between the polarizations induced by each IR pulse, the visible pulse upconverts the separate polarizations induced by each IR pulse. These differences account for the fact that the interferograms obtained with stretched visible pulses show oscillations about an approximately constant value, whereas the interferograms obtained with 100 fs visible pulses show an increase in the average value of the oscillations in a region about the zero delay point corresponding roughly to a FWHM of the IR-visible cross-correlation. The extra contribution to the SFG signal is a non-oscillatory contribution and so contributes to the noise without contributing to the signal at the vibrational resonances. In our case, this effect will decrease the SNR by a factor of approximately $\sqrt{2}$.

3.5 Signal-to-Noise Ratios in FT-SFG and Multichannel Measurements

The time required to obtain the spectra shown in Section 3.4 greatly exceeded the time (of order 10^2 s) with which spectra of other surface systems have been obtained using multichannel detection of SFG produced from broadband IR and narrowband visible pulses [37, 163] generated by kHz Ti:sapphire amplifier systems similar to ours. Therefore, a detailed comparison of the signal-to-noise ratios of spectra obtained by FT-SFG and multichannel detection is in order. This is not a new problem, as signal-intensity-dependent noise sources are known to degrade the signal-to-noise ratio in FTIR compared to multichannel and even

sequential single-channel spectroscopies [164, 165, 166]. We begin with a more physically intuitive but qualitative description.

Consider an interferogram of N steps that converts by Fourier transformation into a spectrum with N channels of which only $M(< N)$ channels contain nonzero signal that is taken to be of more or less equal magnitude in those M channels. The measured interferogram can be regarded as a sum of an ideal, noise-free interferogram and a noise interferogram. If the total number of signal photons in the interferogram is $\mathcal{N}$, then the average signal per step of the interferogram is $\langle f_n \rangle = \mathcal{N}/N$. An important point to recall is that a Fourier transform is essentially just a sum of elements (points in an interferogram), each of which is multiplied by a complex factor of unit magnitude. In the case of the ideal interferogram, we expect that, to within some constant factor, the Fourier transformation of the ideal interferogram will yield a spectrum with Fourier amplitudes in the M nonzero-signal channels equal to a sum of all the photons in the interferogram divided by the number (M) of the channels with nonzero signal:

$$\langle F_m \rangle \sim A\frac{\mathcal{N}}{M} = A\frac{N}{M}\langle f_n \rangle , \tag{3.35}$$

where A is a constant. Let the noise in each step of the noise interferogram be represented by a random quantity δ_f with a mean square of $\sigma_f^2 = \left\langle \delta_f^2 \right\rangle$. To understand the transformation of the noise in the interferogram into the transformed spectrum, we note that, statistically, a random function about zero multiplied by a periodic function of unit magnitude remains a random function of the same magnitude as the original random function. In general, a sum of N values of a random function about zero of mean square value σ^2 yields a quantity of magnitude $\sqrt{N}\,\sigma$. Therefore, Fourier transformation should convert the noise interferogram to a noise per frequency channel of $\sigma_F \sim A\sqrt{N}\sigma_f$. Fourier transformation of the experimentally measured interferogram is expected to yield a signal-to-noise ratio of

$$SNR_F \sim \frac{\mathcal{N}}{M\sqrt{N}\sigma_f} = \frac{\sqrt{N}}{M}\frac{\langle f_n \rangle}{\sigma_f}. \tag{3.36}$$

The preceding result for the signal-to-noise ratio of a Fourier-transformed interferogram also follows from a more thorough mathematical analysis. Consider a set of discrete signals f_n obtained from the N (assumed even) interferometer steps n, where $n = -N/2, -N/2 +$

$1, -N/2+2, ..., N/2-1$. We can define a Fourier series

$$F_m = F_{m+Ns} = \frac{1}{\sqrt{N}} \sum_{n=-N/2}^{N/2-1} f_n e^{i2\pi mn/N}, \tag{3.37}$$

with m and s being integers varying from $-N/2$ to $N/2-1$ and from $-\infty$ to $+\infty$ respectively. Comparison with Eq. (3.7) yields

$$F_m = \frac{1}{\sqrt{N}} \tilde{\Sigma}(m\,\delta\nu, \delta\tau, T), \tag{3.38}$$

with $f_n = S(n\,\delta\tau)\delta\tau$, $T/N = \delta\tau$, $\delta\nu = 1/T$ and $m\,\delta\nu = \nu$. The discrete inverse Fourier transform of F_m gives

$$f_n = \frac{1}{\sqrt{N}} \sum_{m=-N/2}^{N/2-1} F_m e^{-i2\pi mn/N}, \tag{3.39}$$

which can be derived from Eq. (3.37) using the equality

$$\sum_{m=-N/2}^{N/2-1} e^{i2\pi m(n-n')/N} = N\,\delta_{n,n'}, \tag{3.40}$$

where $\delta_{n,n'} = 1$ if $n = n'$ and is zero otherwise. From Eqs. (3.37) and (3.39), we obtain the Parseval-Rayleigh relation

$$\sum_{m=-N/2}^{N/2-1} |F_m|^2 = \sum_{n=-N/2}^{N/2-1} |f_n|^2. \tag{3.41}$$

We separate the signal from the noise by writing

$$f_n = f_n^0 + \delta_n \tag{3.42}$$

and

$$F_m = F_m^0 + \Delta_m, \tag{3.43}$$

where δ_n and Δ_m are random noise and are related by the discrete Fourier transform

$$\Delta_m = \frac{1}{\sqrt{N}} \sum_m \delta_n e^{i2\pi\, m\, n/N}. \tag{3.44}$$

We define the average noise in the interferogram (σ_f) and spectrum (σ_F) by

$$\sigma_f^2 = \langle \delta_n \delta_n^* \rangle \tag{3.45}$$

and

$$\sigma_F^2 = \langle \Delta_m \Delta_m^* \rangle\,, \tag{3.46}$$

where the angled brackets indicate averages over the N values of n or m. We then have

$$\begin{aligned}\sigma_F^2 &= \langle \Delta_m \Delta_m^* \rangle \\ &= \frac{1}{N^2} \sum_{m,n,n'} \delta_n \delta_{n'}^* e^{-i2\pi \frac{m}{N}(n-n')} \\ &= \frac{1}{N^2} \sum_{n,n'} \delta_n \delta_{n'}^* N \delta_{n,n'} \\ &= \sigma_f^2. \end{aligned} \tag{3.47}$$

This result also follows from the Parseval-Rayleigh relationship of Eq. (3.41) by replacing f_n by δ_n and F_m by Δ_m.

Except in the case of a very narrowband spectrum (i.e., a spectrum corresponding to an interferogram that oscillates over its entire extent between some peak value and a minimum value much smaller than the peak value) with fluctuations determined by the signal intensity (e.g., fluctuations due to photon counting), the amplitude of the fluctuations in the interferogram should have very little periodicity. It is then to be expected that the amplitude of the fluctuations in the Fourier transform of the interferogram will be evenly distributed throughout the spectrum.

For estimation of signal-to-noise ratios, we assume a spectrum such that among the N frequency channels, only M of them have significant amounts of signal. From Eq. (3.41), we find

$$|F_{m=0}|^2 + M\langle |F_{m\neq 0}|^2 \rangle = N\langle |f_n|^2 \rangle, \tag{3.48}$$

where $\langle |F_{m\neq 0}|^2 \rangle$ is the average of $|F_{m\neq 0}|^2$ over the M channels of significant signal. We use the crude approximation that $\langle |F_{m\neq 0}|^2 \rangle \approx |\langle F_{m\neq 0} \rangle|^2$ and also $\langle |f_n|^2 \rangle \approx |\langle f_n \rangle|^2$ (An interferogram often exhibits only weak variations of signal about the mean signal level). By Eqs. (3.5) and (3.38), we also expect to have $F_{m=0} \sim M\langle F_{m\neq 0} \rangle$. Therefore, we obtain

$$|\langle F_{m\neq 0} \rangle|^2 \sim \frac{N}{M(M+1)} |\langle f_n \rangle|^2. \tag{3.49}$$

The signal-to-noise ratio of the significantly occupied channels in the FT spectrum is now given by

$$\mathrm{SNR_{FT}} = \frac{\langle F_m \rangle}{\sigma_F} \approx \sqrt{\frac{N}{M(M+1)}} \frac{\langle f_n \rangle}{\sigma_f}. \tag{3.50}$$

Note that $\langle f_n \rangle / \sigma_f$ is the average SNR of a single step in the interferogram.

One might expect intuitively that as the noise in the interferogram appears to be more or less evenly distributed in the frequency channels of the FT spectrum, the signal in the interferogram would also be evenly redistributed in the FT spectrum, i.e., $N\langle f_n \rangle \simeq F_{m=0} + M\langle F_{m\neq 0} \rangle \sim 2M\langle F_m \rangle$. One would then have $\langle F_m \rangle \sim (N/2M)\,\langle f_n \rangle$. This is, however, not true because the Fourier transform is not performed on the field but on the intensity, and the Parseval theorem here applies to intensities rather than electric fields. Consequently, $\langle F_m \rangle \sim \sqrt{N/M(M+1)}\langle f_n \rangle$. This difference tends to make the SNR of FT spectroscopy inferior to that of multichannel spectroscopy, although both utilize the idea of multiplexing (The demultiplexing is performed by FFT in FT-SFG and by a grating in multichannel detection).

Consider obtaining a multichannel spectrum over the same measurement time as for obtaining an interferogram with N steps and a spectrum occupying roughly $M\,(< N)$ frequency channels. Assuming the same total number of photons is acquired in the two measurements, the total signal in both schemes is $N\langle f_n \rangle$. Therefore, in the case of multi-channel detection, the signal in each frequency channel is $N\langle f_n \rangle / M$. Let the noise in each channel be σ_M. The corresponding SNR for multi-channel detection is

$$\mathrm{SNR_{MC}} = \frac{N\langle f_n \rangle}{M\sigma_M}. \tag{3.51}$$

We can now compare the SNR's of the two approaches. First, assuming that the detector noise dominates, we have $\sigma^2_{M,MC} = N\sigma^2_{f,FT}$ because the detector in the multi-channel case is open N times as long as at each point in the interferogram. We then find from Eqs. (3.50) and (3.51)

$$\frac{\mathrm{SNR_{MC}}}{\mathrm{SNR_{FT}}} \simeq \sqrt{\frac{M(M+1)}{M^2}} \sim 1. \tag{3.52}$$

Next, assuming signal intensity fluctuations due to the Poisson statistics of photon counting are the dominant source of noise, we have $\sigma_f = \sqrt{\langle f_n \rangle}$ and $\sigma_M = \sqrt{N\langle f_n \rangle / M}$ and, therefore,

$$\mathrm{SNR_{FT}} \sim \sqrt{\frac{N}{M(M+1)}\langle f_n \rangle} \sim \frac{\sqrt{N\langle f_n \rangle}}{M}, \tag{3.53}$$

$$\mathrm{SNR_{MC}} = \sqrt{\frac{N\langle f_n \rangle}{M}}, \tag{3.54}$$

and

$$\frac{\mathrm{SNR_{MC}}}{\mathrm{SNR_{FT}}} \sim \sqrt{M}. \tag{3.55}$$

In this case, the multi-channel detection scheme is clearly more advantageous. For surface-specific SFG with pulsed lasers, the noise experienced is usually dominated by signal fluctuations due to photon counting. Note that both $\mathrm{SNR_{MC}}$ and $\mathrm{SNR_{FT}}$ are proportional to the square root of the total signal $N\langle f_n \rangle$ and hence, the square root of the signal collection time. In FT spectroscopy, therefore, $\mathrm{SNR_{FT}}$ is independent of the number of steps N taken as long as the data collection time remains unchanged.

We have found rough agreement between theory and experiment on the SNR in our FT-SFG measurements. In the experiments, the step size of our interferograms ($\sim \lambda_{IR}/10$) yields a spectral range in the Fourier transforms that is much larger than the bandwidth of the IR beam from the OPA. The spectral density in the FT spectrum outside the bandwidth of the IR input should be zero, but noise in the interferogram is redistributed in the FT spectrum more or less evenly throughout the spectral range. A portion of this spectral range in which only noise contributes to the spectral intensity is shown in Figure 3.5d. We can estimate our SNR by the ratio of the spectral peak intensity to the average noise in the frequency channels outside the signal bandwidth. For the largest peaks in the ssp and ppp spectra of Figures 3.5 and 3.6, the resulting signal-to-noise ratios are 66 and 94, respectively. To estimate the theoretically expected SNR, we note that each of the two interferograms is made up of a total of about 3.3×10^5 signal photon counts and that the full-width at half maxima of the two peaks in the ssp spectrum occupy a total of about 7 units of spectral resolution, i.e., $M \simeq 7$, whereas the single large peak in the ppp spectrum has $M \simeq 3.5$. Assuming that signal fluctuations due to the Poissonian nature of photon counting dominate, we expect signal-to-noise ratios of about $\frac{\sqrt{3.3\times10^5}}{7} = 82$ and $\frac{\sqrt{3.3\times10^5}}{3.5} = 164$ for the largest peaks in the ssp and ppp spectra, respectively. These numbers are within a factor of 2 of the experimental values.

As seen in Eq. (3.55), for equal total numbers of collected photons and noise dominated by photon counting statistics, obtaining equal SNRs requires M times as much time in a FT-SFG scheme as in a multichannel scheme. The question is then whether the signal

level per shot in multichannel SFG is equal to that in FT-SFG despite the loss of energy in forming the narrowband visible pulse for multichannel SFG. We assume that the irradiating spot on the sample surface is determined by the (smaller) IR focal spot and the visible pulse is stretched to the same picosecond pulse width in the FT case as the narrowband visible in the multi-channel case. In both cases, the detected signal per laser shot is related to the input IR energy per pulse, U_{IR}, and input visible pulse intensity, I_{vis}, by $S_{SF} \propto I_{vis}U_{IR}$. If I_{vis} and U_{IR} are the same for both cases, the signal S_{SF} should also be the same.

In real experiments with femtosecond laser systems, U_{IR} is often limited to a few tens of μJ, and I_{vis} is limited by continuum generation or damage in the medium. For typical liquids or solids, I_{vis} is limited to around $10^1 - 10^2$ GW/cm^2. To achieve a peak intensity of $I_{vis} \sim 50$ GW/cm^2 by overlapping IR and visible inputs in a 60 μm spot requires a visible pulse energy of about 3 μJ for a 5 ps pulse, which is readily available from a kilohertz amplifier system. Usually there is much more visible pulse energy available for up-conversion in the FT-SFG case than in the multi-channel case, but unfortunately it does not help $\mathrm{SNR_{FT}}$ because of limitations on I_{vis}. For equal data collection times, multichannel SFG with a 1 kHz, millijoule-per-pulse laser system will typically provide a better SNR than FT-SFG.

Despite the SNR problem noted above, there are situations in which FT-SFG may be preferable to multichannel SFG. In the case of amplifiers operating at hundreds of kilohertz, the energy per pulse from the amplifier is about two orders of magnitude smaller than from a 1 kHz amplifier. In such cases, the visible beam used in SFG can be focused tightly without significant danger of continuum generation or sample damage. The total number of signal photons per pulse obtained by FT-SFG will then be a factor of approximately $U_{\mathrm{FT}}/U_{\mathrm{MC}}$ times the number of signal photons per pulse obtained by multi-channel detection, where U_{FT} and U_{MC} are the energies of the visible pulses used in FT-SFG and multi-channel SFG, respectively. Typically, there is of order 10^1 times as much energy available for upconversion in the FT-SFG approach as in the multi-channel approach, which should make the FT approach comparable to the multi-channel approach with regard to the time required to obtain spectra of equal SNR. In addition, FT-SFG spectroscopy with unchirped

femtosecond visible pulses allows for the elimination of non-resonant background from a spectrum. By choosing visible delays such that the visible pulse does not overlap either IR pulse (thereby eliminating any instantaneous nonlinear response) but still overlaps most of the free-induction decay after the second IR pulse, almost all of the detected signal should come from the resonant response. This can be useful for studying systems in which a strong non-resonant response obscures the resonant response.

3.6 Conclusion

In summary, by use of a very simple interferometer and broadband IR and visible pulses, we were able to demonstrate surface FT-SFG spectroscopy that has subbandwidth resolution and yields spectra identical to those obtainable by traditional approaches with tunable picosecond pulses. When fluctuations in the signal source (e.g., photon counting statistics) dominate, Fourier transformation degrades the signal-to-noise ratio of the spectroscopy in comparison with multichannel SFG spectroscopy performed with a broadband IR pulse and a narrowband visible pulse. This diminishes its appeal for widespread use with kilohertz laser amplifier systems. However, FT-SFG may be attractive in applications in which the available energy from the laser is insufficient to produce continuum generation or sample damage and when working with systems displaying a strong nonresonant response that obscures resonant features of interest.

Bibliography

[1] A.P. Alivisatos. Perspectives on the physical chemistry of semiconductor nanocrystals. *J. Phys. Chem.*, 100:13226, 1996.

[2] J.Z. Zhang. Ultrafast studies of electron dynamics in semiconductor and metal colloidal nanoparticles: Effects of size and surface. *Acc. Chem. Res.*, 30:423, 1997.

[3] C.R. Henry. Surface studies of supported model catalysts. *Surf. Sci. Rep.*, 31:235, 1998.

[4] Y.R. Shen. *The Principles of Nonlinear Optics*. John Wiley & Sons, Inc., New York, 1984.

[5] S. Mukamel. *Principles of Nonlinear Optical Spectroscopy*. Oxford University Press, Inc., New York, 1995.

[6] Y.R. Shen. Surface spectroscopy by nonlinear optics. In T.W. Hänsch and M. Inguscio, editors, *Frontiers in Laser Spectroscopy*, Proceedings of the International School of Physics "Enrico Fermi" Course CXX. North Holland, Amsterdam, 1994.

[7] T.F. Heinz. Second-order nonlinear optical effects at surfaces and interfaces. In H.-E. Ponath and G.I. Stegeman, editors, *Nonlinear Surface Electromagnetic Phenomena*. Elsevier Science Publishers B.V., Amsterdam, 1991.

[8] C.K. Chen, T.F. Heinz, D. Ricard, and Y.R. Shen. Detection of molecular monolayers by optical second-harmonic generation. *Phys. Rev. Lett.*, 46:1010, 1981.

[9] P.B. Miranda and Y.R. Shen. Liquid interfaces: A study by sum-frequency vibrational spectroscopy. *J. Phys. Chem. B*, 103:3292.

[10] X. Wei, P.B. Miranda, and Y.R. Shen. Surface vibrational spectroscopic study of surface melting of ice. *Phys. Rev. Lett.*, 86:1554, 2001.

[11] P.S. Cremer, X.C. Su, Y.R. Shen, and G.A. Somorjai. Ethylene hydrogenation on Pt(111) monitored in situ at high pressures using sum frequency generation. *J. Am. Chem. Soc.*, 118:2942, 1996.

[12] X.D. Zhu, Th. Rasing, and Y.R. Shen. Surface diffusion of CO on Ni(111) studied by diffraction of optical second-harmonic generation off a monolayer grating. *Phys. Rev. Lett.*, 61:2883, 1988.

[13] P. Guyot-Sionnest. Coherent processes at surfaces: Free-induction decay and photon echo of the Si-H stretching vibration for H/Si(111). *Phys. Rev. Lett.*, 66:1489, 1991.

[14] Y.-S. Lee and M.C. Downer. Reflected fourth-harmonic radiation from a centrosymmetric crystal. *Opt. Lett.*, 23:918, 1998.

[15] C. Voelkmann, M. Mauerer, W. Berthold, and U. Höfer. Second-harmonic diffraction from a transient population grating of silicon dangling bonds. *Phys. Stat. Sol. a*, 175(1):169, 1999.

[16] T. Kikteva, D. Star, A.M.D. Lee, G.W. Leach, and J.M. Papanikolas. Five wave mixing: Surface-specific transient grating spectroscopy as a probe of low frequency intermolecular adsorbate motion. *Phys. Rev. Lett.*, 85:1906, 2000.

[17] S. Fujiyoshi, T. Ishibashi, and H. Onishi. Interface-specific vibrational spectroscopy of molecules with visible lights. *J. Phys. Chem. B*, 108:10636, 2004.

[18] L. Allen and J.H. Eberly. *Optical Resonance and Two-Level Atoms.* Dover Publications, Inc., New York, 1987.

[19] W.H. Knox, D.S. Chemla, G. Livescu, J.E. Cunningham, and J.E. Henry. Femtosecond carrier thermalization in dense Fermi seas. *Phys. Rev. Lett.*, 61:1290, 1988.

[20] J.-Y. Bigot, M.T. Portella, R.W. Schoenlein, J.E. Cunningham, and C.V. Shank. Two-dimensional carrier-carrier screening in a quantum well. *Phys. Rev. Lett.*, 67:636, 1991.

[21] M.T. Portella, J.-Y. Bigot, R.W. Schoenlein, J.E. Cunningham, and C.V. Shank. k-space carrier dynamics in GaAs. *Appl. Phys. Lett.*, 60:2123, 1992.

[22] A. Cavalleri, C. Toth, C.W. Siders, J.A. Squier, F. Ráksi, P. Forget, and J.C. Kieffer. Femtosecond structural dynamics in VO_2 during an ultrafast solid-solid phase transition. *Phys. Rev. Lett.*, 87:237401, 2001.

[23] R. Haight. Electron dynamics at surfaces. *Surf. Sci. Rep.*, 21:275, 1995.

[24] R.R. Cavanagh, D.S. King, J.C. Stephenson, and T.F. Heinz. Dynamics of nonthermal reactions: Femtosecond surface chemistry. *J. Phys. Chem.*, 97:786, 1993.

[25] W. Ho. Reactions at metal surfaces induced by femtosecond lasers, tunneling electrons, and heating. *J. Phys. Chem.*, 100:13050, 1996.

[26] M. Bonn, S. Funk, Ch. Hess, D.N. Denzler, C. Stampfl, M. Scheffler, M. Wolf, and G. Ertl. Phonon- versus electron-mediated desorption and oxidation of CO on Ru(0001). *Science*, 285:1042, 1999.

[27] D.N. Denzler, C. Frischkorn, C. Hess, M. Wolf, and G. Ertl. Electronic excitation and dynamic promotion of a surface reaction. *Phys. Rev. Lett.*, 91:226102, 2003.

[28] H. Petek and S. Ogawa. Surface femtochemistry: Observation and quantum control of frustrated desorption of alkali atoms from noble metals. *Annu. Rev. Phys. Chem.*, 53:507, 2002.

[29] Ch. Reuß, I.L. Shumay, U. Thomann, M. Kutschera, M. Weinelt, Th. Fauster, and U. Höfer. Control of the dephasing of image-potential states by CO adsorption on Cu(100). *Phys. Rev. Lett.*, 82:153, 1999.

[30] M. Weinelt, Ch. Reuß, M. Kutschera, U. Thomann, I.L. Shumay, Th. Fauster, U. Höfer, F. Theilmann, and A. Goldmann. Decay and dephasing of image-potential states due to surface defects and disorder. *Appl. Phys. B*, 68:377, 1999.

[31] Th. Fauster. Watching the life of electrons at surfaces with two-photon photoemission. *Surf. Sci.*, 507:256, 2002.

[32] H. Petek and S. Ogawa. Femtosecond time-resolved two-photon photoemission studies of electron dynamics in metals. *Prog. Surf. Sci.*, 56:239, 1997.

[33] A. Baltuška, Z. Wei, M.S. Pshenichnikov, D.A. Wiersma, and R. Szipőcs. All-solid-state cavity-dumped sub-5-fs laser. *Appl. Phys. B*, 65:175, 1997.

[34] A. Baltuška, Z.Y. Wei, M.S. Pshenichnikov, and D.A. Wiersma. Optical pulse compression to 5 fs at a 1-MHz repetition rate. *Opt. Lett.*, 22:102, 1997.

[35] M. Nisoli, S. De Silvestri, O. Svelto, R. Szipöcs, K. Ferencz, Ch. Spielmann, S. Sartania, and F. Krausz. Compression of high-energy laser pulses below 5 fs. *Opt. Lett.*, 22:522, 1997.

[36] B. Schenkel, J. Biegert, U. Keller, C. Vozzi, M. Nisoli, G. Sansone, S. Stagira, S. De Silvestri, and O. Svelto. Generation of 3.8-fs pulses from adaptive compression of a cascaded hollow fiber supercontinuum. *Opt. Lett.*, 28:1987, 2003.

[37] L.J. Richter, T.P. Petralli-Mallow, and J.C. Stephenson. Vibrationally resolved sum-frequency generation with broad-bandwidth infrared pulses. *Opt. Lett.*, 23:1594, 1998.

[38] J.A. McGuire, W. Beck, X. Wei, and Y.R. Shen. Fourier-transform sum-frequency surface vibrational spectroscopy with femtosecond pulses. *Opt. Lett.*, 24:1877, 1999.

[39] C.-P. Huang, M.T. Asaki, S. Backus, M.M. Murnane, H.C. Kapteyn, and H. Nathel. 17-fs pulses from a self-mode-locked Ti:sapphire laser. *Opt. Lett.*, 17:1289, 1992.

[40] M.T. Asaki, C.-P. Huang, D. Garvey, J. Zhou, H.C. Kapteyn, and M.M. Muranane. Generation of 11-fs pulses from a self-mode-locked Ti:sapphire laser. *Opt. Lett.*, 18:977, 1993.

[41] J. Herrmann. Theory of Kerr-lens mode locking: role of self-focusing and radially varying gain. *J. Opt. Soc. Am. B*, 11:498, 1994.

[42] R.A. Kaindl, M. Wurm, K. Reimann, P. Hamm, A.M. Weiner, and M. Woerner. Generation, shaping, and characterization of intense femtosecond pulses tunable from 3 to 20 μm. *J. Opt. Soc. Am. B*, 17:2086, 2000.

[43] P. Hamm, R.A. Kaindl, and J. Stenger. Noise suppression in femtosecond mid-infrared light sources. *Opt. Lett.*, 25:1798, 2000.

[44] E. Yablonovitch, D.L. Allara, C.C. Chang, T. Gmitter, and T.B. Bright. Unusually low surface-recombination velocity on silicon and germanium surfaces. *Phys. Rev. Lett.*, 57:249, 1986.

[45] G.S. Higashi, Y.J. Chabal, G.W. Trucks, and Krishnan Raghavachari. Ideal hydrogen termination of the Si(111) surface. *Appl. Phys. Lett.*, 56:656, 1990.

[46] J. J. Boland. The importance of structure and bonding in semiconductor surface-chemistry - hydrogen on the Si(111)-7×7 surface. *Surf. Sci.*, 244(1-2):1, 1991.

[47] T. Engel. The interaction of molecular and atomic oxygen with Si(100) and Si(111). *Surf. Sci. Rep.*, 18:91, 1993.

[48] Ph. Avouris. Atom-resolved surface chemistry: The early steps of Si(111)-7×7 oxidation. *J. Vac. Sci. Tech. B*, 9:424, 1990.

[49] K.-Y. Kim, T.-H. Shin, S.-J. Han, and H. Kang. Identification of the precursor state in the initial stages of Si(111)-(7×7) oxidation. *Phys. Rev. Lett.*, 82:1329, 1999.

[50] M. Carbone, M.N. Piancastelli, M.P. Casaletto, R. Zanoni, G. Comtet, G. Dujardin, and L. Hellner. Low-temperature adsorption states of benzene on Si(111)7×7 studied by synchrotron-radiation photoemission. *Phys. Rev. B*, 61:8531, 2000.

[51] M. Scarselli, P. Castrucci, P.D. Szkutnik, A. Sgarlata, and M. De Crescenzi. STM study of Si(111)7×7 reconstructed surface carbonization induced by acetylene. *Surf. Sci.*, 559:223, 2004.

[52] R. E. Schlier and H. E. Farnsworth. Structure and adsorption characteristics of clean surfaces of germanium and silicon. *J. Chem. Phys.*, 30(4):917, 1959.

[53] E. G. McRae. Surface stacking-sequence and (7×7) reconstruction at Si(111) surfaces. *Phys. Rev. B*, 28(4):2305, 1983.

[54] T. Yamaguchi. Si(111) 7×7 reconstruction - strain in the adatom model. *Phys. Rev. B*, 30(4):1992, 1984.

[55] F. J. Himpsel and I. P. Batra. Structural models for Si(111)-(7×7). *J. of Vac. Sci. Tech. A*, 2(2):952, 1984.

[56] K. Takayanagi, Y. Tanishiro, M. Takahashi, and S. Takahashi. Structural analysis of Si(111)-7×7 by UHV-transmission electron diffraction and microscopy. *J. Vac. Sci. Tech. A*, 3:1502, 1985.

[57] R. J. Culbertson, L. C. Feldman, and P. J. Silverman. Atomic displacements in the Si(111)-(7×7) surface. *Phys. Rev. Lett.*, 45(25):2043, 1980.

[58] G. Binnig, H. Rohrer, C. Gerber, and E. Weibel. 7×7 reconstruction on Si(111) resolved in real space. *Phys. Rev. Lett.*, 50(2):120, 1983.

[59] P. Avouris. Atom-resolved surface-chemistry using the scanning tunneling microscope. *J. Phys. Chem.*, 94(6):2246–2256, 1990.

[60] I. K. Robinson, W. K. Waskiewicz, P. H. Fuoss, J. B. Stark, and P. A. Bennett. X-ray-diffraction evidence of adatoms in the Si(111)7×7 reconstructed surface. *Phys. Rev. B*, 33(10):7013, 1986.

[61] S. Y. Tong, H. Huang, C. M. Wei, W. E. Packard, F. K. Men, G. Glander, and M. B. Webb. Low-energy electron-diffraction analysis of the Si(111)7×7 structure. *J. Vac. Sci. Tech. A*, 6(3):615, 1988.

[62] R. J. Hamers, R. M. Tromp, and J. E. Demuth. Surface electronic-structure of Si(111)-(7×7) resolved in real space. *Phys. Rev. Lett.*, 56(18):1972, 1986.

[63] R. Losio, K. N. Altmann, and F. J. Himpsel. Fermi surface of Si(111)7×7. *Phys. Rev. B*, 61(16):10845, 2000.

[64] J. E. Demuth, B. N. J. Persson, and A. J. Schell-Sorokin. Temperature-dependent surface-states and transitions of Si(111)-7×7. *Phys. Rev. Lett.*, 51(24):2214, 1983.

[65] B. N. J. Persson and J. E. Demuth. Inelastic-scattering of slow-electrons from Si(111) surfaces. *Phys. Rev. B*, 30(10):5968, 1984.

[66] P. Mårtensson, W.-X. Ni, G. V. Hansson, J. M. Nicholls, and B. Reihl. Surface electronic-structure of Si(111)7×7-Ge and Si(111)5×5-Ge studied with photoemission and inverse photoemission. *Phys. Rev. B*, 36(11):5974, 1987.

[67] R. I. G. Uhrberg, T. Kaurila, and Y. C. Chao. Low-temperature photoemission study of the surface electronic structure of Si(111)7×7. *Phys. Rev. B*, 58(4):R1730, 1998.

[68] F. J. Himpsel. Inverse photoemission from semiconductors. *Surf. Sci. Rep.*, 12(1):1, 1990.

[69] F.J. Himpsel. Inverse photoemission at semiconductor surfaces. In M. Balkanski, editor, *Handbook on Semiconductors (Completely Revised Edition)*, volume 2. Elsevier Science B.V., Amsterdam, 1994.

[70] F.J. Himpsel and Th. Fauster. Probing valence states with photoemission and inverse photoemission. *J. Vac. Sci. Tech. A*, 2:815, 1984.

[71] R.I.G. Uhrberg, G.V. Hansson, U.O. Karlsson, J.M. Nicholls, P.E.S. Persson, S.A. Flodström, R. Engelhardt, and E.-E. Koch. Photoemission study of the surface and bulk electronic structures of Si(111)7×7 and Si(111)$\sqrt{3}\times\sqrt{3}$:Al. *Phys. Rev. B*, 31:3805, 1985.

[72] J.M. Nicholls and B. Reihl. Adatom electronic structure of the Si(111)7×7 surface. *Phys. Rev. B*, 36:8071, 1987.

[73] J. M. Layet, J. Y. Hoarau, H. Luth, and J. Derrien. Dispersion of the dangling-bond surface-states of Si(111)-(7×7). *Phys. Rev. B*, 30(12):7355, 1984.

[74] R. Wolkow and P. Avouris. Atom-resolved surface-chemistry using scanning tunneling microscopy. *Phys. Rev. Lett.*, 60(11):1049, 1988.

[75] P. Avouris and R. Wolkow. Atom-resolved surface-chemistry studied by scanning tunneling microscopy and spectroscopy. *Phys. Rev. B*, 39(8):5091–5100, 1989.

[76] J.E. Northrup. Origin of surface states on Si(111)(7×7). *Phys. Rev. Lett.*, 57:154, 1986.

[77] J. Ortega, F. Flores, and A. L. Yeyati. Electron correlation effects in the Si(111)-7×7 surface. *Phys. Rev. B*, 58(8):4584, 1998.

[78] F.J. Himpsel, G. Hollinger, and R.A. Pollak. Determination of the Fermi-level pinning position at Si(111) surfaces. *Phys. Rev. B*, 28:7014, 1983.

[79] U. Backes and H. Ibach. Evidence for a 2D-metallic state of the clean 7×7 Si(111) surface. *Solid State Comm.*, 40:575, 1981.

[80] F.G. Allen and G.W. Gobeli. Work function, photoelectric threshold, and surface states of atomically clean silicon. *Phys. Rev.*, 127:150, 1962.

[81] S. Heike, S. Watanabe, Y. Wada, and T. Hashizume. Electron conduction through surface states of the Si(111)-(7×7) surface. *Phys. Rev. Lett.*, 81:890, 1998.

[82] K. Yoo and H.H. Weitering. Electrical conductance of reconstructed silicon surfaces. *Phys. Rev. B*, 65:115424, 2002.

[83] T. Tanikawa, K. You, I. Matsuda, S. Hasegawa, and Y. Hasegawa. Nonmetallic transport property of the Si(111)7×7 surface. *Phys. Rev. B*, 68:113303, 2003.

[84] D. Fick, R. Veith, H.D. Ebinger, H.J. Jänsch, C. Weindel, H. Winnefeld, and J.J. Paggel. Electron correlations in the clean and hydrogen-covered Si(111)-(7×7) surface at extremely low Li coverages. *Phys. Rev. B*, 60:8783, 1999.

[85] J.E. Rowe and H. Ibach. Surface-state transitions of silicon in electron energy-loss spectra. *Phys. Rev. Lett.*, 31:102, 1973.

[86] H. Kobayashi, K. Edamoto, M. Onehi, and M. Nishijima. Comparison of the Si(111)(7×7) and (1×1) surfaces. *Solid State Comm.*, 44:1449, 1982.

[87] C. Noguez, C. Beitia, W. Preyss, A. I. Shkrebtii, M. Roy, Y. Borensztein, and R. Del-Sole. Theoretical and experimental optical spectroscopy study of hydrogen adsorption at Si(111)-(7×7). *Phys. Rev. Lett.*, 76(26):4923, 1996.

[88] R. Alameh and Y. Borensztein. Optical response of Si(111)-7×7. *Surf. Science*, 251/252:396, 1991.

[89] P.E. Wierenga, A. Van Silfhout, and M.J. Sparnaay. Reflectometric study of dangling-bond surface states and oxygen adsorption on the clean Si(111)7×7 surface. *Surf. Sci.*, 87:43, 1979.

[90] C. Noguez, A.I. Shkrebtii, and R. Del Sole. Microscopic theory of electron transitions at Si(111)-7×7 optical properties and energy-loss spectra. *Surf. Sci.*, 331:1349, 1995.

[91] U. Höfer. Nonlinear optical investigations of the dynamics of hydrogen interaction with silicon surfaces. *Appl. Phys. A*, 63(6):533, 1996.

[92] T. Suzuki, D. E. Milovzorov, S. Kogo, M. Tsukakoshi, and M. Aono. Surface second-harmonic generation spectra of Si(111)-7×7 in the 1.0-1.7-eV fundamental photon energy. *Appl. Phys. B*, 68(3):623, 1999.

[93] T. Suzuki. Surface-state transitions of Si(111)-7×7 probed using nonlinear optical spectroscopy. *Phys. Rev. B*, 61(8):R5117, 2000.

[94] K. Pedersen and P. Morgen. Dispersion of optical second-harmonic generation from Si(111)7×7. *Phys. Rev. B*, 52(4):R2277, 1995.

[95] W. Daum, H. J. Krause, U. Reichel, and H. Ibach. Nonlinear-optical spectroscopy at silicon interfaces. *Physica Scripta*, T49B:513, 1993.

[96] J.E. Mejía, B.S. Mendoza, M. Palummo, G. Onida, R. Del Sole, S. Bergfeld, and W. Daum. Surface second-harmonic generation from Si(111)(1×1)H: Theory versus experiment. *Phys. Rev. B*, 66:195329, 2002.

[97] G. Erley and W. Daum. Silicon interband transitions observed at Si(100)-SiO_2 interfaces. *Phys. Rev. B*, 58(4):R1734, 1998.

[98] O. Madelung, (Ed.). *Semiconductors: Group IV Elements and III-V Compounds*. Data in Science and Technology. Springer-Verlag, Berlin, 1991.

[99] T. Sjodin, H. Petek, and H.-L. Dai. Ultrafast carrier dynamics in silicon: A two-color transient reflection grating study on a (111) surface. *Phys. Rev. Lett.*, 81:5664, 1998.

[100] J. Bokor, R. Storz, R.R. Freeman, and P.H. Bucksbaum. Picosecond surface electron dynamics on photoexcited Si(111)(2×1) surfaces. *Phys. Rev. Lett.*, 57:881, 1986.

[101] N.J. Halas and J. Bokor. Surface recombination on the Si(111)2×1 surface. *Phys. Rev. Lett.*, 62:1679, 1989.

[102] S. Tanaka and K. Tanimura. Time-resolved two-photon photoelectron spectroscopy of the Si(001)-(2×1) surface. *Surf. Sci.*, 529:L251, 2003.

[103] M. Weinelt, M. Kutschera, Th. Fauster, and M. Rohlfing. Dynamics of exciton formation at the Si(100)c(4×2) surface. *Phys. Rev. Lett.*, 92:126801, 2004.

[104] U. Höfer. Time-resolved coherent spectroscopy of surface states. *Appl. Phys. B*, 68:383, 1999.

[105] C. Voelkmann. *Five-wave Mixing Investigations of Electron Dynamics at Silicon Surfaces*. PhD thesis, Physik-Department der Technishen Universität München and Fachbereich Physik der Philipps-Universität Marbug, 2001.

[106] S. Mukamel and R. Loring. Nonlinear response function for time-domain and frequency-domain four-wave mixing. *J. Opt. Soc. Am. B*, 3:595, 1986.

[107] M. Berg, C.A. Walsh, L.R. Narasimhan, K.A. Littau, and M.D. Fayer. Dynamics in low temperature glasses: Theory and experiments on optical dephasing, spectral diffusion, and hydrogen tunneling. *J. Chem. Phys.*, 88:1564, 1988.

[108] D.S. Chemla. Lecture notes for physics 208A: Introduction to quantum electronics and nonlinear optics, 1996.

[109] P. Meystre and M. Sargent III. *Elements of Quantum Optics*. Springer-Verlag, Berlin, 1990.

[110] D.Th. Leeson, O. Berg, and D.A. Wiersma. Low-temperature protein dynamics studied by the long-lived stimulated photon echo. *J. Phys. Chem.*, 98:3913, 1994.

[111] P. Hamm, M. Lim, and R.M. Hochstrasser. Non-Markovian dynamics of the vibrations of ions in water from femtosecond infrared three-pulse photon echoes. *Phys. Rev. Lett.*, 81:5326, 1998.

[112] P. Hamm, M. Lim, and R.M. Hochstrasser. Structure of the amide I band of peptides measured by femtosecond nonlinear-infrared spectroscopy. *J. Phys. Chem. B*, 102:6123, 1998.

[113] H.-K. Nienhuys, S. Woutersen, R.A. van Santen, and H.J. Bakker. Mechanism for vibrational relaxation in water investigated by femtosecond infrared spectroscopy. *J. Chem. Phys.*, 111:1494, 1999.

[114] P. Bratu. *Optische Frequenzverdopplung an Si(111)7×7: Adsorption Dissoziation und Desorption von Sauerstoff*. PhD thesis, Ludwig-Maximilians-Universität München, 1993.

[115] K. Shudo, S. Takeda, and T. Munakata. Resonant surface-state transitions of Si(111)-7×7 measured with two-photon photoemission spectroscopy. *Phys. Rev. B*, 65:075302, 2002.

[116] D. E. Aspnes and A. A. Studna. Dielectric functions and optical parameters of Si, Ge, GaP, GaAs, GaSb, InP, InAs, and InSb from 1.5 to 6.0 eV. *Phys. Rev. B*, 27(2):985–1009, 1983.

[117] M.A.J. Mauerer. *Frequenzverdopplung ultrakurzer Laserimpulse an hochangeregten Siliziumoberflächen und physisorbierten Edelgasschichten*. PhD thesis, Technische Universität München, 1996.

[118] J.P. Long, H.R. Sadeghi, J.C. Rife, and M.N. Kabler. Surface space-charge dynamics and surface recombination on silicon (111) surfaces measured with combined laser and synchrotron radiation. *Phys. Rev. Lett.*, 64:1158, 1990.

[119] W. Daum, H. Ibach, and J.E. Müller. Adatom vibrations on Si(111) reconstructed surfaces. *Phys. Rev. Lett.*, 59:1593, 1987.

[120] J. Kim, M.L. Yeh, F.S. Khan, and J.W. Wilkins. Surface phonons of the Si(111)-7×7 reconstructed surface. *Phys. Rev. B*, 52:14709, 1995.

[121] M. Weinelt. Decay and dephasing of image-potential states studied by time-resolved two-photon photoemission. *Surf. Sci.*, 482:519, 2001.

[122] E. Knoesel, A. Hotzel, and M. Wolf. Temperature dependence of surface state lifetimes, dephasing rates and binding energies on Cu(111) studied with time-resolved photoemission. *J. Electron Spec. Relat. Phenom.*, 88:577, 1998.

[123] J.-Y. Bigot, M.T. Portella, R.W. Schoenlein, J.E. Cunningham, and C.V. Shank. Two-dimensional carrier-carrier screening in a quantum well. *Phys. Rev. Lett.*, 67:636, 1991.

[124] M.T. Portella, J.-Y. Bigot, R.W. Schoenlein, J.E. Cunningham, and C.V. Shank. k-space carrier dynamics in GaAs. *Appl. Phys. Lett.*, 60:2123, 1992.

[125] D.-S. Kim, J. Shah, J.E. Cunningham, T.C. Damen, S. Schmitt-Rink, and W. Schäfer. Carrier-carrier scattering in a degenerate electron system: Strong inhibition of scattering near the Fermi edge. *Phys. Rev. Lett.*, 68:2838, 1992.

[126] S.R. Bolton, S. Bar-Ad, G. Sucha, D.S. Chemla, D.L. Sivco, and A.Y. Cho. Effect of confinement on energy-dependent dephasing in heterostructures. *Phys. Rev. B*, 55:15768, 1997.

[127] T. Sjodin, C.-M. Li, H. Petek, and H.-L. Dai. Ultrafast transient grating scattering studies of carrier dynamics at a silicon surface. *Chem. Phys.*, 251:205, 2000.

[128] P.Y. Yu and M. Cardona. *Fundamentals of Semiconductors: Physics and Materials Properties*. Springer-Verlag, Berlin, first edition, 1996.

[129] D.Y. Oberli, D.R. Wake, M.V. Klein, J. Klem, T. Henderson, and H. Morkoç. Time-resolved Raman scattering in GaAs quantum wells. *Phys. Rev. Lett.*, 59:696, 1987.

[130] J.F. Ryan and M.C. Tatham. Time-resolved Raman measurements of electron-phonon interactions in quantum wells and superlattices. In J. Shah, editor, *Hot Carriers in Semiconductor Nanostructures: Physics and Applications*. Academic Press, Inc., San Diego, 1992.

[131] J. Shah. *Ultrafast Spectroscopy of Semiconductors and Semiconductor Nanostructures*. Springer-Verlag, Berlin, 1999.

[132] Y. Enta, S. Suzuki, and S. Kono. Angle-resolved-photoemission study of the electronic structure of the Si(001)$c(4\times2)$ surface. *Phys. Rev. Lett.*, 65:2704, 1990.

[133] L.S.O. Johansson and B. Reihl. Unoccupied surface-state bands on the single-domain Si(100)2×1 surface. *Surf. Sci.*, 269/270:810, 1992.

[134] J.E. Northrup. Electronic structure of Si(100)$c(4\times2)$ calculated within the GW approximation. *Phys. Rev. B*, 47:10032, 1993.

[135] M. Rohlfing, P. Krüger, and J. Pollmann. Efficient scheme for GW quasiparticle band-structure calculations with applications to bulk Si and to the Si(001)-(2×1) surface. *Phys. Rev. B*, 52:1905, 1995.

[136] H. Petek, H. Nagano, and S. Ogawa. Hole decoherence of d bands in copper. *Phys. Rev. Lett.*, 83:832, 1999.

[137] M. Roth, M. Pickel, J.-X. Wang, M. Weinelt, and Th. Fauster. Electron scattering at steps: Image-potential states on Cu(119). *Phys. Rev. Lett.*, 88:096802, 2002.

[138] M. Zavelani-Rossi, D. Polli, G. Cerullo, S. De Silvestri, L. Gallmann, G. Steinmeyer, and U. Keller. Few-optical-cycle laser pulses by OPA: broadband chirped mirror compression and SPIDER characterization. *Appl. Phys. B*, 74:S245, 2002.

[139] Q. Du, E. Freysz, and Y.R. Shen. Surface vibrational spectroscopic studies of hydrogen bonding and hydrophobicity. *Science*, 264:826, 1994.

[140] X. Wei, P.B. Miranda, and Y.R. Shen. Surface vibrational spectroscopic study of surface melting of ice. *Phys. Rev. Lett.*, 86:1554, 2001.

[141] J. Stenger, D. Madsen, P. Hamm, E.T.J. Nibbering, and T. Elsaesser. Ultrafast vibrational dephasing of liquid water. *Phys. Rev. Lett.*, 87:027401, 2001.

[142] S. Woutersen and P. Hamm. Nonlinear two-dimensional vibrational spectroscopy. *J. Phys.: Cond. Matt.*, 14:R1035, 2002.

[143] M. Khalil, N. Demirdöven, and A. Tokmakoff. Obtaining absorptive line shapes in two-dimensional infrared vibrational correlation spectra. *Phys. Rev. Lett.*, 90:047401, 2003.

[144] O. Golonzka, M. Khalil, N. Demirdöven, and A. Tokmakoff. Coupling and orientation between anharmonic vibrations characterized with two-dimensional infrared vibrational echo spectroscopy. *J. Chem. Phys.*, 115:10814, 2001.

[145] S.M. Gallagher Faeder and D.M. Jonas. Phase-resolved time-domain nonlinear optical signals. *Phys. Rev. A*, 62:033820, 2000.

[146] J.D. Hybl, A. Albrecht Ferro, and D.M. Jonas. Two-dimensional Fourier transform electronic spectroscopy. *J. Chem. Phys.*, 115:6606, 2001.

[147] G.V. Hartland, B.F. Henson, and P.M. Felker. The dependence of Fourier transform nonlinear Raman spectroscopies on the temporal characteristics of the excitation fields. *J. Chem. Phys.*, 91:1478, 1989.

[148] G.V. Hartland, P.W. Joireman, L.L. Connell, and P.M. Felker. High resolution Fourier transform stimulated emission and molecular beam hole-burning spectroscopy with picosecond excitation sources: Theoretical and experimental results. *J. Chem. Phys.*, 96:179, 1992.

[149] P.M. Felker. Fourier-transform nonlinear spectroscopies. In A.B. Myers and T.R. Rizzo, editors, *Laser Techniques in Chemistry*. John Wiley & Sons, Inc., 1995.

[150] J. Kauppinen and J. Partanen. *Fourier Transforms in Spectroscopy*. Wiley-VCH, Berlin, 2001.

[151] S.F. Johnston. *Fourier Transform Infrared: A Constantly Evolving Technology*. Ellis Horwood Ltd., New York, 1991.

[152] L. Mertz. *Transformations in Optics*. John Wiley & Sons, Inc., New York, 1965.

[153] H. Sakai. High resolving power Fourier spectroscopy. In G.A. Vanasse, editor, *Spectrometric Techniques*. Academic Press, New York, 1977.

[154] G.A. Vanasse, A.T. Stair, Jr., , and D.J. Baker, editors. *Aspen International Conference on Fourier Spectroscopy, 1970*, number 114 in AFCRL-71-0019 Special Reports. Air Force Cambridge Research Laboratories, 1971.

[155] G.A. Vanasse and H. Sakai. Fourier spectroscopy. In E. Wolf, editor, *Progress in Optics*, volume VI. North-Holland Publishing Co., Amsterdam, 1967.

[156] T. Hirschfeld. Quantitative FT-IR: A detailed look at the problems involved. In J.R. Ferraro and L.J. Basile, editors, *Fourier Transform Infrared Spectroscopy*, volume 2. Academic Press, New York, 1979.

[157] E.V. Loewenstein. Fourier spectroscopy: An introduction. In G.A. Vanasse, A.T. Stair, Jr., and D.J. Baker, editors, *Aspen International Conference on Fourier Spectroscopy, 1970*, number 114 in AFCRL-71-0019 Special Reports. 1971.

[158] J.H. Moore, C.C. Davis, and M.A. Coplan. *Building Scientific Apparatus: A Practical Guide to Design and Construction*. Perseus Books Publishing, L.L.C., Cambridge, Massachusetts, 2 edition, 1991.

[159] J. Sagiv. Organized monolayers by adsorption. 1. formation and structure of oleophobic mixed monolayers on solid surfaces. *J. Amer. Chem. Soc.*, 102:92, 1980.

[160] Xing Wei. *Sum-Frequency Spectroscopic Studies I. Surface Melting of Ice II. Surface Alignment of Polymers*. PhD thesis, University of California, Berkeley, 2000.

[161] R. Superfine, P. Guyot-Sionnest, J.H. Hunt, C.T. Kao, and Y.R. Shen. Surface vibrational spectroscopy of molecular adsorbates on metals and semiconductors by infrared-visible sum-frequency generation. *Surf. Sci.*, 200:L445, 1988.

[162] B. Schrader. *Raman/Infrared Atlas of Organic Compounds*. VCH, New York, second edition, 1989.

[163] S. Roke, J. Schins, M. Müller, and M. Bonn. Vibrational spectroscopic investigation of the phase diagram of a biomimetic lipid monolayer. *Phys. Rev. Lett.*, 90:128101, 2003.

[164] T. Hirschfeld. The implications of fluctuation noise in multiplex spectroscopy. *Appl. Spec.*, 30:234, 1976.

[165] T. Hirschfeld. Ideal FT-IR spectrometers and the efficiency of real instruments. *Appl. Spec.*, 40:1239, 1986.

[166] E. Voigtman and J.D. Winefordner. The multiplex disadvantage and excess low-frequency noise. *Appl. Spec.*, 41:1182, 1987.